

**TWO DIMENSIONAL MATERIAL BASED FIELD
EFFECT TRANSISTOR FOR BIOSENSING
APPLICATIONS**

**A Thesis Submitted to
the Graduate School of Engineering and Sciences of
İzmir Institute of Technology
in Partial Fulfillment of the Requirements for the Degree of**

DOCTOR OF PHILOSOPHY

in Photonics Science and Engineering

**by
Dilce İNANÇ**

**July 2023
İZMİR**

We approve the thesis of **Dilce İNANÇ**

Examining committee members:

Assoc. Prof. Dr. Ümit Hakan YILDIZ
Department of Chemistry, İzmir Institute of Technology

Prof. Dr. Sinan BALCI
Department of Photonics, İzmir Institute of Technology

Assist. Prof. Dr. Onur BÜYÜKÇAKIR
Department of Chemistry, İzmir Institute of Technology

Assist. Prof. Dr. Osman AKIN
Department of Mechatronics, İzmir Katip Çelebi University

Assist. Prof. Dr. Ümit TAYFUN
Department of Basic Sciences, Bartın University

18 July 2023

Assoc. Prof. Dr. Ümit Hakan YILDIZ
Supervisor, Department of Chemistry,
İzmir Institute of Technology

Prof. Dr. Cem ÇELEBİ
Co-Supervisor, Department of
Physics,
İzmir Institute of Technology

Prof. Dr. Canan VARLIKLI
Head of the Department of Photonics
Science and Engineering

Prof. Dr. Mehtap EANES
Dean of the Graduate School of
Engineering and Sciences

ACKNOWLEDGMENTS

First of all, I would like to thank my advisor, Assoc. Prof. Dr. Ümit Hakan YILDIZ. His encouragement and support made this thesis possible. I am very grateful for his invaluable help, guidance and his endless patience as well as his understanding provided during this thesis. I would like to thank my committee members of my thesis Prof. Dr. Sinan BALCI, Assist. Prof. Onur BÜYÜKÇAKIR, Assist. Prof. Osman AKIN and Assist. Prof. Ümit TAYFUN for their participations.

First I would like to express my heart-felt gratitude to my husband Eray Mustafa İNANÇ who is always believing in me and unwaveringly supporting me in my life and my little son Çınar İNANÇ. I would like thank you my mother Dilek KOÇKAR, to my father Cengiz ÖZKENDİR and especially my sister Özgü ÖZKENDİR. I am also thankful to Alper YANILMAZ for their friendship and endless support. Additionally, I am very thankful to S. Batuhan KALKAN, Mehmet FİDAN, Tuğçe KÜÇÜKTARTAR Öykü YILDIRIMKARAMAN and Mustafa Umut MUTLU for their caring and valuable advice. Besides, I would like to thank Soner KARABACAK, Ahmet ÖNDER and the members of BioSens&BioApps research group with all the alumni. Also, I would like to acknowledge my institution, İzmir Institute of Technology, for providing me research facilities during my PhD study. This study is supported by the The Scientific and Technological Research Council of Turkey, TÜBİTAK Project: 117F243

ABSTRACT

TWO DIMENSIONAL MATERIAL BASED FIELD EFFECT TRANSISTOR FOR BIOSENSING APPLICATIONS

This thesis presents research on the use of two-dimensional material graphene as an area-effective transistor and its application in biological fields. The formation of wrinkled and flat structures on the surface of a single-layer graphene area-effective transistor, epitaxially grown for determining the bio-membrane dynamics of graphene, was examined using two different methods of deposition (thermal evaporation and pulsed electron accumulation) of a silicon dioxide (SiO_2) layer. The investigation aimed to evaluate the pH and lipid bilayer formation performance of both wrinkled and flat GFETs. Increased sensitivity was determined through electrical measurements, as the oxide layer becomes thinner due to the existence of wrinkles, thus providing electrostatic coating on graphene. A sensor platform of chemiresistor type was developed for the differential determination of volatile organic compounds (VOCs) by synthesizing single-layer, bilayer, and multilayer graphene, enabling the analysis of ethanol (EtOH) and methanol (MeOH). Sensors produced using three different graphene morphologies demonstrated differential MeOH-EtOH responses attributed to the differential intercalation phenomenon in multilayer graphene morphologies when compared to ethanol. For the detection of VOCs such as acetone, ethanol, and hexane in human breath, a polymer nanofiber/multi-walled carbon nanotube or poly(3,4-ethylenedioxythiophene)/gold (Au) and iron oxide (Fe) hybrid bioelectronic interface was developed. Sensitivity studies were conducted by applying pure VOCs at different concentrations to the sensor platforms, and the behavior of the sensor platforms against interfering elements was evaluated by recharacterizing them under CO_2 and humidity conditions. Considering the responses of MWCNT-PLLCL-Fe-based sensors to acetone, ethanol, and hexane, the tendency of water molecules to adhere to the Fe surface was shown to decrease water condensation on the conductive layer compared to other sensor configurations, indicating that the humidity effect was minimized in MWCNT-PLLCL-Fe-based sensors.

ÖZET

BİYOALGILAMA UYGULAMALARI İÇİN İKİ BOYUTLU MALZEME TABANLI ALAN ETKİLİ TRANSİSTÖR

Bu tez, 2 boyutlu malzeme grafenin alan etkili transistör olarak kullanımı ve biyolojik alanlarda kullanımı üzerine bir araştırma sunar. Grafenin biyo-membran dinamiği tayininde epitaksiyel olarak büyütülen tek katman grafen alan etkili transistör üzerine iki farklı yöntemle (termal buharlaştırma ve darbeli electron biriktirme) deposit edilen silikon dioksit (SiO_2) katmanının yüzeyinde buruşuk ve düz oluşumu incelendi. Buruşuk ve düz sonuçları GFET'lerin pH değerlendirmesi ve lipid çift tabakası oluşturma performansı araştırıldı. Artan hassasiyet, oksit tabakasının kırışıklıkların oluşumuyla incelmeye ve böylece grafen üzerinde elektrostatik kaplamayı kolaylaştırdığı yapılan elektriksel ölçümler sonucunda belirlendi. Grafenin uçucu organik bileşiklerin (UOB) ayrımsal tayini için tek katman, iki katman ve çok katman grafen sentezlenerek etanol (EtOH) ve metanol (MetOH) tayini yapılabilen kemiresistör tipi sensör platformu geliştirildi. Üç grafen morfolojisi kullanılarak imal edilen sensörler, etanol ile karşılaştırıldığında çok katmanlı grafen morfolojileri içinde metanolün diferansiyel interkalasyonu fenomenine atfedilen ayırıcı MeOH-EtOH tepkilerini göstermiştir. İnsan nefesindeki aseton, etanol ve hekzan gibi UOB'in tespiti için polimer nanofiber / çok duvarlı karbon nanotüp (ÇDKNT) veya poli (3,4-etilendioksitiyofen) / altın (Au) ve demir oksit (Fe) metal parçacığı hibrit biyoelektronik arayüz geliştirildi. Sensör platformlarına farklı konsantrasyonlarda saf UOB'ler uygulanarak duyarlılık çalışmaları yapıldı ve UOB'ler ile CO_2 , nem ve N_2 katkılı koşullar yeniden karakterize edilerek sensör platformlarının girişim yapan elementlere karşı davranışı değerlendirildi. ÇDNT-PLLCL- Fe yapıları sensörlerin aseton, etanol ve hekzana karşı verdikleri tepkiler göz önüne alındığında, su moleküllerinin Fe yüzeye tutunma eğilimi, iletken katman üzerinde su yoğunlaşmasını diğer konfigürasyondaki sensörlere göre azaldığı ve bu nedenle ÇDKNT-PLLCL- Fe yapıları sensörlerde nem etkisi minimize olduğu gösterildi.

To my Family

TABLE OF CONTENTS

LIST OF FIGURES	viii
LIST OF TABLES.....	xiv
LIST OF SYMBOLS	xv
LIST OF ABBREVIATIONS.....	xvii
CHAPTER 1. INTRODUCTION.....	1
CHAPTER 2. MOTIVATION	7
2.1. Graphene	
2.1.1. Structure of Graphene.....	8
2.1.2. Electrical Properties of Graphene	9
2.2. Production Methods of Graphene	11
2.2.1. Mechanical Exfoliation.....	11
2.2.2. Epitaxial Growth on SiC Substrate.....	12
2.2.3. Chemical Vapor Deposition.....	13
2.3. Graphene Foam	14
2.3.1. Structure of Graphene Foam.....	14
2.3.2. Synthesis of Graphene Foam	16
2.4. Graphene Field Effect Transistors	18
2.4.1. Characteristics of GFETs.....	19
2.4.2. GFET Working Mechanism.....	21
2.4.3. GFET Medical Diagnostic	23
2.4.4. Point of Care for GFET	25
CHAPTER 3. EXPERIMENTAL METHODS.....	26
3.1. Device Fabrication	26

3.1.1. Graphene Foam Synthesis with Chemical Vapor Deposition (CVD) Method	26
3.1.2. Epitaxial Growth of Graphene	27
3.1.3. Chemical Vapor Deposition (CVD) Growth of Graphene	30
3.1.4. Gas Sensor Platform Fabrication	31
3.2. Characterization Techniques	37
3.2.1 Scanning Electron Microscopy	37
3.2.2. Atomic Force Microscopy	38
3.2.3. Raman Spectroscopy.....	39
3.2.4. Electrical Characterizations	41
 CHAPTER 4. RESULTS AND DISCUSSION	 43
4.1. Lipid Bilayer on Wrinkled-interfaced Graphene Field Effect Transistor	43
4.2. Multi-layered Graphene Based Gas Sensor Platform for Volatile Organic Compounds Discrimination via Differential Intercalation.....	53
4.3. Cost-Effective Portable Breath Analyzer for Determination of Volatile Organic Compounds	68
 CHAPTER 5. CONCLUSION	 89
 REFERENCES	 93

LIST OF FIGURES

<u>Figure</u>	<u>Page</u>
Figure 2.1. (a) Schematic representation of van de Waals bonds and covalent bonds between carbon atoms between multilayer graphene sheets, respectively ³⁸ . (b) Graphical representation of the sp^2 and p_z orbitals in graphene (c) Schematic of σ and π bonds in graphene. ³⁹	8
Figure 2.2. Electronic dispersion and Dirac points of single layer graphene ⁴⁷	10
Figure 2.3. (a) Steps of synthesizing single-layer graphene by mechanical decomposition method using HOPG. Optical microscope image of mechanically exfoliated graphene transferred on SiO_2/Si substrate under (b) white and (c) green light illumination.....	12
Figure 2.4. SEM images of epitaxial graphene grown on SiC (0001) surface (a) fractures and (b) wrinkles ⁵⁴	13
Figure 2.5. Schematic representation of CVD growth mechanism of graphene ⁵⁵	14
Figure 2.6. (a) Low and (b) high resolution SEM image and the porous graphene foam after removal of the Cu/Ni template (c) Schematic representation of 3D GF	16
Figure 2.7. Schematic representation of (a) CVD (b) growth parameters and (c) transfer process	17
Figure 2.8. Schematic illustration of GFET structure.....	18
Figure 2.9. Schematic representation of (a) typical FET (b) n-channel FET and (c) p-channel FET structures	19
Figure 2.10. Schematic representations of (a) top-gated (b) back-gated and (c) liquid-gated GFET device structures	20
Figure 3.1. CVD growth system for graphene foam.....	27
Figure 3.2. a) Ultra-high vacuum epitaxial graphene growth set up b) control panel and c) graphene growth at 1350 °C	28
Figure 3.3. Thermal evaporation system for SiO_2 deposition.....	29
Figure 3.4. Pulsed Electron Deposition (PED) system for SiO_2 deposition.....	30
Figure 3.5. a) The CVD growth set-up and b) furnace for BLG growth	31
Figure 3.6. Image of Laser Cutter b) digital image of designed PMMA sensor substrate after cut via Laser Cutter	32

<u>Figure</u>	<u>Page</u>
Figure 3.7. (a) Schematic representation of the electrospinning device (b) The electrospinning device we used in the studies	34
Figure 3.8. (a) Digital image of synthesized Fe and Au nanoparticles (b) DLS spectra showing the diameters of the synthesized Au and Fe nanoparticles.....	36
Figure 3.9. a) Schematic representation of sensor platform formation b) Digital image of polymer nanofiber formation on PMMA substrate c) Functionalized sensor platform with MWCNT or PEDOT:PSS	37
Figure 3.10. Scanning Electron Microscopy	38
Figure 3.11. Digital image of atomic force microscopy in our laboratory	39
Figure 3.12. Raman spectroscopy measurement system	40
Figure 3.13. Raman spectroscopy measurements of single layer, bilayer and few layer graphene ¹⁰²	41
Figure 3.14. (a) HP4145B parameter analyzer that we use in electrical measurements (b) Two probe sample holder station	41
Figure 3.15. VOC detection system in our laboratory	42
Figure 4.1. Designed device fabrication step by step.	44
Figure 4.2. Schematic representation of wrinkled and flat surface structure after 15 nm and 100 nm thick SiO ₂ deposition via TE and PED, respectively.....	45
Figure 4.3. Schematic figure of lipid bilayer formation on wrinkled a) and flat b) SiO ₂ surface	46
Figure 4.4. High magnification scanning electron microscopy images of (a) wrinkled and (b) flat oxide surfaces.....	47
Figure 4.5. (a) AFM topography image of TE deposited SiO ₂ wrinkle network on epitaxial graphene (50 x 50 μm ² area) (b) Zoomed in AFM topography image of localized height protrusions (10 x 10 μm ² area) (c) The cross-sectional line profiles of primary and secondary wrinkles were examined, with the primary wrinkles denoted as 1 and the secondary wrinkles as 2)..	48
Figure 4.6. I-V characteristics depicting the pH dependence are presented for both (a) flat interfaced-GFET and (b) wrinkle interfaced-GFET. Insets in the figure illustrate the linear fitting of current versus pH values for the flat interfaced-GFET and the wrinkle interfaced-GFET, respectively.....	50

<u>Figure</u>	<u>Page</u>
Figure 4.7. The time-dependent current measurements of lipid vesicle adsorption characteristics are illustrated for (a) wrinkle interfaced-GFET surface and (b) flat interfaced-GFET surface.....	52
Figure 4.8. A histogram showing the repeatability of absorbing and dissipating lipid vesicles from SiO ₂ surface. Black columns show the current change of lipid vesicles adsorbing on the SiO ₂ surface. Gray columns depict the current change of lipid vesicle dissipating via SDS solution from SiO ₂ surface	53
Figure 4.9. a) SLG b) BLG and c) MLG devices	54
Figure 4.10. Raman spectra of SLG (black), BLG (red) and MLG (blue)	55
Figure 4.11. SEM images of SLG grown on SiC substrate with (a) 10.000 x (b) 50.000 x (c) 100.000 x and (d) 200.000 x magnifications	56
Figure 4.12. SEM images of BLG grown on SiC substrate with (a) 2.500 x (b) 50.000 x (c) 100.000 x and (d) 200.000 x magnifications	57
Figure 4.13. (a) SEM images of MLG (b) TEM image of MLG framework and inset related SAED pattern (c) d-spacing between graphene layers is assessed using the MLG XRD spectrum. (inset).....	58
Figure 4.14. (a) AFM topography image measuring 50 x 50 μm and its corresponding cross-sectional profile (b) Conductive AFM current mapping performed on SLG, and the resulting current distribution histogram.....	59
Figure 4.15. (a) AFM topography image measuring 50 x 50 μm and its corresponding cross-sectional profile (b) Conductive AFM current mapping performed on BLG, and the resulting current distribution histogram	60
Figure 4.16. Concentration dependent chemiresistor responses of SLG upon exposure to (I) 0.2 ppm (II) 0.5 ppm, (III) 2.5 ppm (IV) 5 ppm (V) 25 ppm and (VI) 50 ppm of MeOH (red) and EtOH (black), measured at room temperature (22 °C). (The gray traces in the graph illustrate the baseline and response stability SLG).....	61

<u>Figure</u>	<u>Page</u>
Figure 4.17. Concentration dependent chemiresistor responses of BLG upon exposure to (I) 0.2 ppm (II) 0.5 ppm, (III) 2.5 ppm (IV) 5 ppm (V) 25 ppm and (VI) 50 ppm of MeOH (red) and EtOH (black), measured at room temperature (22 °C). (The gray traces in the graph illustrate the baseline and response stability BLG))	62
Figure 4.18. Concentration dependent chemiresistor responses of MLG upon exposure to (I) 0.2 ppm (II) 0.5 ppm, (III) 2.5 ppm (IV) 5 ppm (V) 25 ppm and (VI) 50 ppm of MeOH (red) and EtOH (black), measured at room temperature (22 °C). (The gray traces in the graph illustrate the baseline and response stability M LG))	63
Figure 4.19. Theoretical results indicating the modulations in charge density distributions of graphene (green) and MeOH/EtOH (cyan) molecules upon their adsorption on graphene surface, (a) individual molecule and (b) to (e) two to five molecules, respectively.	65
Figure 4.20. Bar graph of RH on chemiresistor responses at 25 ppm of EtOH and MeOH	66
Figure 4.21. Normalized chemiresistor responses of (a) SLG and (b) BLG and (b) MLG upon exposure to varying concentrations of MeOH (red) and EtOH (black).	67
Figure 4.22. (a) The effect of temperature on chemiresistor responses at 25 ppm of EtOH and MeOH measured at room temperature 20 °C and 30 °C	68
Figure 4.23. a) Concentration dependent response of MLG device in the existence of a) water/EtOH and b) water/MeOH.....	68
Figure 4.24. Scanning electron microscope images of PVDF nanofibers obtained by electrospinning at a distance of (a) 45 mm, (b) 145 mm and (c) 170 mm... ..	71
Figure 4.25. Scanning electron microscopy images of (a-c) CNT coated and (d-f) PEDOT: PSS coated PVDF structures at different magnifications coated on PMMA surface by electrospinning method	71
Figure 4.26. Scanning electron microscopy images of (a-c) PVDF-CNT-Au NP and (d-f) PVDF-CNT-Fe NP coated structures at different magnifications coated on PMMA surface by electrospinning method.....	72

<u>Figure</u>	<u>Page</u>
Figure 4.27. Scanning electron microscopy images of (a-c) PVDF-PEDOT: PSS-Au NP and (d-f) PVDF- PEDOT: PSS -Fe NP coated structures at different magnifications coated on PMMA surface by electrospinning method.....	73
Figure 4.28. Scanning electron microscopy images of (a-c) PU, (d-f) CNT coated and (g-i) PEDOT: PSS coated PU structures at different magnifications coated on PMMA surface by electrospinning method.....	74
Figure 4.29. Scanning electron microscopy images of (a-c) PCL, (d-f) CNT coated and (g-i) PEDOT: PSS coated PCL structures at different magnifications coated on PMMA surface by electrospinning method.....	75
Figure 4.30. Scanning electron microscopy images of (a-c) PLLCL, (d-f) CNT coated and (g-i) PEDOT: PSS coated PLLCL structures at different magnifications coated on PMMA surface by electrospinning method.....	76
Figure 4.31. 2D topographical image of PVDF-PEDOT: PSS and PVDF-CNT conductive nets with the range of μm scale (scale bars are 10 μm and 2 μm , respectively) (a-b) their height profiles (c-d) and e) F-d analysis of PVDF-PEDOT: PSS and MWCNT network.....	78
Figure 4.32. Conductive AFM topography imaged and I-V characteristics of (a) PEDOT: PSS and (b) MWCNT nets which were measured from three different locations (below).....	79
Figure 4.33. (a) PVDF-MWCNT, PU-MWCNT, PCL-MWCNT and PLLCL-MWCNT structured sensor platforms reproducibility results of their responses to ethanol and acetone gases (b) Time dependent current change measurements given to ethanol and acetone between 0.5-100 ppm gas concentrations (average and standard deviation of five different sensors from each platform were taken into account).	81
Figure 4.34. (a) PLLCL- PEDOT: PSS structured sensor platforms reproducibility results of their responses to ethanol and acetone gases (b) Time dependent current change measurements given to ethanol and acetone between 0.5-100 ppm gas concentrations (average and standard deviation of five different sensors from each platform were taken into account).	82

<u>Figure</u>	<u>Page</u>
Figure 4.35. Time dependent current change graph of PLLCL, PLLCL-MWCNT-Au and PLLCL-MWCNT-Fe nanoparticle decorated sensor platform measurements to 0.5-100 ppm range of acetone with 30%, 50% and 70% humidity environment.....	84
Figure 4.36. Time dependent current change graph of PLLCL, PLLCL-MWCNT-Au and PLLCL-MWCNT-Fe nanoparticle decorated sensor platform measurements to 0.5-100 ppm range of ethanol with 30%, 50% and 70% humidity environment.....	85
Figure 4.37. Time dependent current change graph of PLLCL, PLLCL-MWCNT-Au and PLLCL-MWCNT-Fe nanoparticle decorated sensor platform measurements to 0.5-100 ppm range of hexane with 30%, 50% and 70% humidity environment.....	86
Figure 4.38. Principal component analysis result of an average of thirty determinations of (10 ppm) Ethanol, Formaldehyde, Toluene, and Acetone from the integrated instrument	87
Figure 4.39. Principal component analysis result of an average of thirty determinations of Ethanol, Formaldehyde, Toluene and Acetone obtained from the integrated instrument at 0.5 ppm.....	88

LIST OF TABLES

<u>Table</u>	<u>Page</u>
Table 4.1. The polymers used in the study and their chemical structures	33

LIST OF SYMBOLS

DNA	deoxyribonucleic acid
Cu	copper
Ar	argon
CH ₄	methane
FeCl ₃	ferric chloride
MoS ₂	molybdenum disulfide
Si	silicon
SiO ₂	silicon dioxide
SiC	silicon carbide
MWCNT	multi-walled carbon nanotube
Fe	iron
Au	gold
GaAs	gallium arsenide
GaN	gallium nitride
PDMS	dimethylpolysiloxane
PMMA	Poly(methyl 2-methylpropenoate)
PEDOT: PSS	poly (3,4-ethylenedioxythiophene)
PU	polyurethane
PVDF	Polyvinylidene fluoride
PCL	polycaprolactone
PLLCL	Poly (L-lactide-co-caprolactone)
NADH	nicotineamid adenin dinucleotide
I_d	drain current
μ	carrier mobility
V_d	drain current
C_{ox}	capacitance of oxide layer
V_G	gate voltage
V_{th}	threshold voltage
I_{on}/I_{off}	on/off current ratio
R_c	contact resistance

λ_D	Debye length
ε_r	dielectric constant of electrolyte
ε_0	dielectric constant of vacuum
k_B	Boltzmann constant
T	temperature
N_A	Avogadro constant
e	unity of charge
I	electrolyte's total ion strength

LIST OF ABBREVIATIONS

AFM	Atomic force microscopy
BLG	Bilayer graphene
BSA	Bovine serum albumin
CVD	Chemical vapor deposition
c-AFM	Conductive AFM
CPs	Conductive polymers
DFT	Density functional theory
DLS	Dynamic light scattering
EtOH	Ethanol
GGA	Generalized gradient approximation
GFET	Graphene field effect transistors
GF	Graphene foam
HOPG	Highly oriented pyrolytic graphite
POCT	point-of-care testing
L	Length
MeOH	Methanol
MLG	Multi-layer graphene
MWCNT	Multiwall carbon nanotube
NPs	Nanoparticles
PCA	Principal component analysis
PED	Pulsed Electron Deposition
QHE	Quantum Hall effect
rGO	Reduced graphene oxide
SEM	Scanning electron microscope
SAED	Selected Area Electron Diffraction
SLG	Single layer graphene
TE	Thermal evaporation
3D	Three-dimensional
TEM	Transmission electron microscopy
2D	Two-dimensional

UHV	Ultra-high vacuum
VASP	Vienna ab-initio Simulation Package
VOCs	Volatile organic compounds
W	Width
0D	Zero-dimensional

CHAPTER 1

INTRODUCTION

In recent times, there has been a significant emphasis on enhancing the capabilities of chemiresistor type graphene field effect sensor devices based on exploring its potential for biological applications, recognition of volatile organic compounds in human breath and their selectivity is crucial. This thesis ensures a comprehensive review of the distinguishing features of methanol (MeOH) and ethanol (EtOH) discrimination properties in single-layer, bi-layer, and multi-layer graphene morphologies, polymer nanofiber / carbon nanotube or poly (3,4-ethylenedioxythiophene) / gold and iron oxide metal particle hybrid bioelectronic interface and lipid bilayer-based sensor interface on SiO₂ encapsulated graphene field effect transistors (GFET) various aspects from synthesis to applications.

By using graphene-based sensor platforms to detect glucose¹, hemoglobin (Hb)², nicotinamide adenine dinucleotide (NADH)³, cholesterol⁴, urea⁵, harmful gases^{6,7}, and DNA^{8,9} as examples, the biosensing capability of graphene occupies an important part in literature. According to Perumal et al.¹⁰ graphene-based sensor platforms possess analytical capabilities that extend beyond clinical applications to encompass food sciences. As a result of their enhanced sensing performance, ranging from small molecules to large particles, graphene and other two-dimensional (2D) materials have become essential elements in biosensor technology. Graphene field effect transistors (GFETs), in which a graphene sheet is attached to source and drain electrodes and the current flowing through the graphene sheet between the two electrodes is controlled by a gate electrode, are among the most extensively investigated graphene devices. Because the sensing mechanism of GFET sensors depends on the adsorption of chemical or biological species onto the graphene surface, which either acts as electron donors or acceptors. GFETs provide an acceptable fundamental stage for a wide range of sensors such as pH sensor¹¹, antigen sensor¹², and wearable biosensors for detecting glucose in human blood¹³. However, given graphene's 2D nature, the electronic band structure is greatly influenced by external perturbations. For instance, doping graphene, encapsulating graphene surface with higher dielectric constant material or band gap modulation are just a few of the predicted methods to change the conductivity of

graphene. Lee et.al¹³ explains with details of various strategies for engineering the Fermi level in graphene, including heteroatom substitution, molecular adsorption, introducing functional molecules for enhancing the conductivity of graphene. They clearly show that studies into graphene doping modulation have attracted a lot of interest, and that these studies can be expanded to include hybrids of carbon-based materials as well as extremely high-performance electrical devices, highly sensitive detecting systems, and a variety of other potential uses. On the other hand, encapsulation of graphene is another technique for decreasing charge instability between graphene and analytes. Alexander-Webbel and their colleagues¹⁴ state that depositing an oxide layer onto graphene offers effective protection against environmental factors such as air, humidity, and other disturbances. Therefore, the oxide layer provides complete suppression of conductivity instability in graphene, preventing instability and hysteresis in its responses. Kalkan et al.¹⁵ show that the adsorption and desorption of atmospheric adsorbates have significant effects on the conductivity of epitaxial graphene (n-type) and chemical vapor deposition graphene (p-type) layers on semi-insulating silicon carbide. These processes result in a remarkable increase of over 100% in conductivity when adsorbates are present, while desorption causes a decrease of approximately 45% in conductivity. Hence, the findings indicate that the encapsulation of graphene with SiO₂ grown by the plasma-enhanced deposition (PED) technique effectively prevents the adsorption and desorption of atmospheric adsorbates. Consequently, this encapsulation strategy ensures the electrical stability of graphene remains unaffected by the type of charge carrier, whether it is n-type or p-type.

Recently, the determination of volatile organic compounds (VOCs) with 2D material-based field-effect transistors has become a particularly interesting subject in recent years. In the air quality management¹⁶, pharmaceutical¹⁷, and healthcare industries¹⁸, VOC analysis¹⁹⁻²¹ is crucial. The creating of VOC for alcohols, such as methanol, ethanol, butane, toluene, formaldehyde and more has attracted study attention since, at high exposure levels, they can cause fatal comas that impact the gastrointestinal and central neurological systems²². On a global scale, there have been reported cases of accidental or intentional contamination of beverages and hand sanitizers with primary alcohols, particularly methanol²³. Such contamination has been associated with a rise in the occurrence of intoxications, ultimately leading to an increased number of casualties resulting from methanol poisoning. Although chromatographic techniques remain the established gold standard for detecting primary alcohols, the focus on advancing on-site rapid detection methods is increasing steadily. Recent research has focused on developing

efficient methods for applications such as assessing methanol levels in beverages, consumer products, and even exhaled breath. The aim is to provide quicker and more accessible detection techniques in these specific contexts. The importance of determining volatile organic compounds in human existence has resulted in a noteworthy rise in the quantity of studies done in recent years. Surface modification or functionalization plays a vital role in enhancing the selectivity towards a specific target analyte in a traditional VOC assay utilizing graphene. For example, reduced graphene oxide (rGO) and tin oxide (SnO_2) are employed to selectively detect ethanol in both humid and dry environments by Reddy et.al.²⁴. They showed that the GO include SnO_2 NTs demonstrated a good response (85.3) to 100 ppm ethanol with an optimal operating temperature of 300 C in the dry atmosphere, and they also shown a better ethanol response (51.75) in the wet atmosphere when compared to pristine SnO_2 NTs. By utilizing composite materials of porous reduced graphene oxide (rGO) and tin dioxide (SnO_2), the detection of ethanol (EtOH) can be accomplished with high sensitivity and selectivity. This is facilitated by the synergistic effect of the large surface area of rGO and the specific affinity between EtOH and SnO_2 . This is made possible through the utilization of rGO- SnO_2 composites. Selectivity and repeatability is another important factor for VOC detect gas sensors. Field effect transistors (FETs) based on graphene have been suggested as a method of selectively detecting methanol and ethanol in a study by Liu²⁵ et al. The charge transfer phenomena that results from the adsorption of volatile organic compounds (VOCs) onto the surface of graphene serves as the detecting mechanism. This charge transfer then alters the graphene's charge carrier density, producing different reactions that reveal the presence of MeOH or EtOH. Paul et al. introduced a chemiresistor platform based on three-dimensional (3D) structured graphene nanomesh. This platform demonstrated selectivity in detecting nitrogen dioxide (NO_2) and ammonia (NH_3) gases.²⁶ The sensing potential of 3D graphene morphologies in gas sensing applications is highlighted by this ground-breaking platform. The innovative design of the graphene nanomesh demonstrates the promising potential of 3D graphene structures in sensing technologies by enabling improved surface interactions and selective detection of NH_3 and NO_2 . They showed that the constructed GNM transistor was found to have a high drive current and an $I_{\text{ON}}/I_{\text{OFF}}$ ratio as 6. Additionally, the limits of detection for the ethanol-based graphene nanomesh sensors were 15 and 160 ppb, with sensitivities of around 4.32%/ppm in NO_2 and 0.71%/ppm in NH_3 , respectively.

Specifically, our focus lies on graphene-based field effect transistors (GFETs) and their relevance in medical point-of-care and diagnostic applications. In this thesis, in addition to the biological-based sensor studies with 2-dimensional material-based field-effect transistors in the literature, we developed a sensor interface that mimics the bilayer lipid structure in the cell membrane using basically graphene and its derivatives. For this, we used two different morphologies of the compatible SiO₂ layer on graphene for lipids to form a bilayer on the surface. We deposited these two different structures on a single layer of graphene by thermal evaporation and pulsed electron deposition method, and as a result, we observed that the SiO₂ layer coated with the thermal evaporation method forms a wrinkle structure on the graphene, while with the pulsed electron deposition method exhibits a flat structure on the graphene. We created a graphene field-effect transistor structure by depositing Au contacts on the graphene samples deposited with SiO₂. The pH and lipid sensing performance of wrinkled and flat graphene field effect transistors were investigated by electrical measurements. As a result of these measurements, it has been recorded as a result of the experiments that the electrical response in the GFET sensor found in the wrinkled structure is 10 times higher than the flat one. The reason for the increase in sensitivity in sensors with a wrinkled surface encapsulated with SiO₂ was defined as electrostatic gating between graphene and SiO₂. The current-voltage behavior of lipid molecules, which form a bilayer on the SiO₂ layer, in both wrinkled and flat surface GFET sensor platforms were investigated. As a result of these measurements, the stage of forming a bilayer structure of lipid molecules in 4 steps was determined by looking at the current changes in the current-voltage measurements. According to these graphs, the sensitivity of detecting lipid molecules of the sensor interface in the wrinkled structure is one order of magnitude higher when compared to flat surfaces. In light of all these results, the indicated wrinkled SiO₂ interfaced-GFET shows potential as a sensing platform that mimics cell membranes for innovative bioelectronics applications.

Additionally, we examined selective and sensitive discrimination of volatile organic compounds using graphene-based sensor interfaces with different number of layers. Due to the similarities in their chemical structure and distinguishing group, selective detection of primary alcohols is incredibly difficult. Therefore, our main aim in this study was to distinguish methanol from ethanol even at low concentrations (0.5 ppm) and to ensure selectivity. For this, we created a single-layer, bilayer and multi-layer graphene-based chemiresistor type sensor interface and observed that these sensors gave

electrical signals distinguishing ethanol and methanol from each other. In the three different graphene morphologies produced, intercalation between the graphene layers of methanol caused to differentiate from ethanol. It has also been supported by theoretical studies that this intercalation is directly proportional to the increase in the number of layers of graphene. In addition, the selectivity of these sensors for ethanol and methanol at a certain concentration (25 ppm) in high (80%) and low (20%) humidity environments was also investigated. As a result of experiments, it has been shown that the produced multilayer graphene sensors respond more selectively to low molecular weight alcohols compared to CO₂ and air. Thus, in this study, it was aimed to develop sensor platforms that selectively and sensitively detect MeOH by using different graphene layer numbers with a chemiresistor sensor type.

Further, we aimed to determine the volatile organic compounds harmful to human health such as acetone, ethanol and hexane in a humid environment with using the polymer nanofiber/multiwall carbon nanotube (MWCNT) or poly (3,4-ethylenedioxythiophene) (PEDOT:PSS) / gold and iron oxide metal particle hybrid bioelectronic interface. For this, polymers (Polyvinylidene fluoride (PVDF), polyurethane (PU), Polycaprolactone (PCL) and poly L-lactide-co- ϵ -caprolactone (PLCCL)) were coated on Poly (methyl methacrylate) (PMMA) substrate prepared with laser cutter by electrospinning method and nanofiber structure was formed. MWCNT and PEDOT: PSS were deposited on the prepared nanofibers. The surface and morphological characters of the created sensor surfaces were examined by atomic force microscopy and scanning electron microscopy. As a result of the electrical measurements, the sensors were exposed to different concentrations (0.5, 5, 20, 100 ppm) of acetone and ethanol gas, and it was shown that the sensor with PLLCL nanofiber structure covered with MWCNT was the most responsive sensor combination to the current change. To increase sensitivity, the MWCNT-coated PLLCL sensor structure was modified with gold (Au) and iron (Fe) nanoparticles and exposed to acetone, ethanol and hexane gas in a humid (30% and 70%) environment. It was observed that the sensitivity of the sensor platforms decorated with Au and Fe nanoparticles increased, the response of the PLLCL-MWCNT-Au sensor to low concentrations of acetone gas in both humidity environments was low, while the response of the sensor platform decorated with Fe to ethanol gas was approximately 2 times higher. In conclusion, PLLCL-MWCNT-Fe NP-structured sensors were chosen as potential candidates for application in portable devices for CO₂ and humidity monitoring.

The experimental findings presented in this thesis are anticipated to provide novel device configurations utilizing graphene and conductive polymers for applications in biosensors, selectivity and repeatability of designed sensor platforms, sensing capabilities of different types of GFETs.

CHAPTER 2

MOTIVATION

2.1. Graphene

Two-dimensional (2D) material known as graphene is composed of carbon atoms that have undergone sp^2 hybridization in a honeycomb lattice structure. Due to its remarkable general properties, such as single-atom-thick two-dimensional conjugated structures²⁷, room-temperature stability²⁸ and ballistic transport²⁹, graphene, one of the most fascinating materials, has sparked scientists' great enthusiasm in its synthesis, modification, and applications in many fields since 2004. In addition, a lot of focus has been placed on carbon atom allotropes in addition to graphene. A cylindrical molecular form of graphene known as carbon nanotubes (CNTs), sometimes known as buckytubes, has many outstanding and distinctive properties. CNTs hold significant potential for diverse applications, including nanoelectronics, materials applications, optics, and other fields^{30,31}. Single-walled nanotubes (SWCNTs) and multi-walled nanotubes (MWCNTs) are the two categories into which they can be divided. Fullerene (C₆₀), a different allotrope of the carbon atom, is a zero-dimensional (0D) material with increased surface properties that is employed in solar cell and biomedical applications³².

Graphene consists of a densely packed honeycomb crystal lattice of sp^2 bonded carbon atoms, forming a planar sheet that is only one atom thick. Due to its unique qualities, such as high current density³³, ballistic transport³⁴, chemical inertness³⁵, high thermal conductivity³⁶, and high surface to volume ratio³⁷, in recent times, graphene has garnered considerable attention as a promising candidate for the next generation of electronic materials. Extensive research is currently underway to comprehensively investigate the structure and properties of graphene. This surge in scientific interest is driven by the potential future applications of graphene in the fields of sensing, prompting the need for a deeper understanding of its characteristics. The scope of this thesis chapter does not allow for a thorough treatment of graphene's properties. Extensive research efforts are dedicated to unraveling the structure and properties of graphene due to its remarkable scientific appeal and promising prospects in the realms of electronics and

sensing. The scope of this thesis chapter allows for a thorough treatment of graphene's properties.

2.1.1. Structure of Graphene

A 2D honeycomb lattice plane made of a densely packed single layer of carbon atoms is known as graphene. Carbon atoms create a benzene ring in single layer graphene via sp^2 hybridization with surrounding carbon atoms. The bond between carbon atoms is 0.142 nm in length (Figure 2.1). Graphene has a very thin thickness of 0.34 nm. The bond between carbon atoms is strong enough to withstand external force from a twisting plane without causing atoms to rearrange themselves. Each lattice contains three strong σ bonds that together create a stable hexagonal lattice. Most of the π bonds in graphene's electronic conductivity are found vertically to the lattice plane. Due to the tightly packed of the carbon atoms and the sp^2 hybridization with the orbitals s , p_x , and p_y that make up the σ bond, graphene is stable. π and π^* bonds are created by the hybridization of the π bonds, and they gives graphene its electrical properties by creating a half-filled band that allows free-moving electrons.

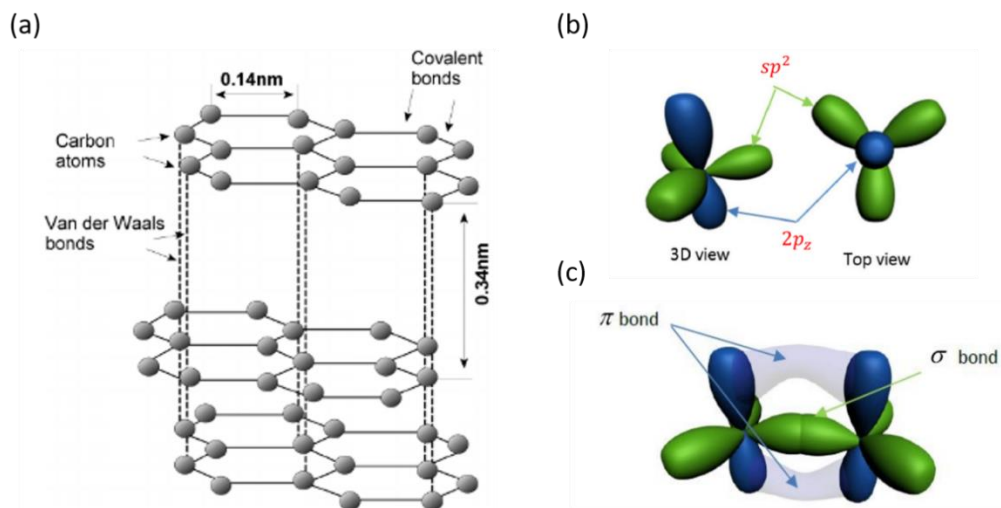


Figure 2.1. (a) Schematic representation of van de Waals bonds and covalent bonds between carbon atoms between multilayer graphene sheets, respectively³⁸. (b) Graphical representation of the sp^2 and p_z orbitals in graphene (c) Schematic of σ and π bonds in graphene.³⁹

Graphene's stability is benefit from one atom thickness, graphene has a very high transparency of 97.79%, it only absorbs 2.3% visible light ⁴⁰. The hexagonal carbon ring that makes up graphene's basic structure has a surface area of 0.052 nm². Since each carbon atom at the vertices is shared by the three unit rings, such a ring only has two carbon atoms. Graphene's advantages of being extremely thin and light are due to a layer that is only one carbon atom thick.

2.1.2. Electrical Properties of Graphene

The conductivity of 10⁶ S/m and a sheet resistance of 31 Ω/sq, graphene is the most conductive substance discovered to date at ambient temperature ⁴¹. Additionally, graphene has a mobility of 2 x 10⁵ cm²/Vs, which is nearly 150 times higher than silicon ⁴². At room temperature, π electrons in graphene are completely free to flow, which results in high conductivity. In addition to these, graphene is a typical semimetal in which slight overlap between the conduction band and valence band. Therefore, lower-energy electrons near the top of the valence band could move into the bottom of the conduction band. Even at absolute zero, a specific concentration of holes is in the valence band and a specific concentration of electrons is already in the conduction band. This behavior results from the Dirac-cone like structure because conduction and valance band intercepts at Dirac point (Figure 2.2). The anomalous quantum hall effect ⁴³ is seen in the electron transport in graphene. These characteristics make graphene even more promising, as it has been utilized to create FETs and other electronic devices. Due to graphene's exceptional electrical properties, devices such a transparent conducting electrodes, sensors, field emitters, ballistic transistors, and integrated circuit components have been developed. Graphene can be used as the channel in a field effect transistor (FET) due to its high electron (or hole) mobility and low Johnson noise⁴⁴, which is the electronic noise arises from the random thermal motion of charge carriers within an electrical conductor in equilibrium. Notably, this noise is present irrespective of the applied voltage. Furthermore, graphene is a candidate for transparent conducting electrodes, which are necessary for applications in touch screens, liquid crystal displays and organic photovoltaic cells and due to its high optical transparency and high conductivity ^{45,46}.

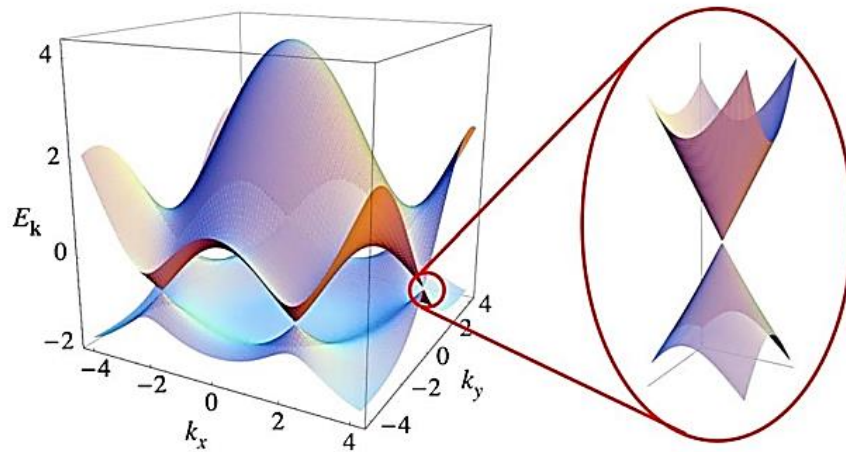


Figure 2.2. Electronic dispersion and Dirac points of single layer graphene⁴⁷

The electrical properties of graphene differ according to the number of layers. The charge carriers in single layer graphene (SLG) can be described as electrons that effectively lose their rest mass and are most accurately represented by the Dirac equations. These charge carriers are referred to as massless Dirac fermions. In comparison to metals and semiconductors, SLG is therefore expected to exhibit several peculiar properties. SLG exhibits ambipolar behavior at room temperature⁴⁸, meaning that the charge carriers can alternate between electrons and holes depending on the type of gate voltage. For this structure, anomalous (half-integer) quantum Hall effect (QHE) has also been seen at low temperatures and at room temperature. SLG is recognized as one of the most robust materials due to its exceptional strength properties. Young's modulus of SLG was calculated as 1.0 TPa⁴⁹. SLG's distinctive features make it a good candidate for use in electronics applications. On the other hand, bi-layer graphene is regarded as a semiconductor with no gap. In contrast to single-layer graphene, bi-layer graphene charge carriers, have finite mass and are referred to as massive Dirac particles. The structure also displays an anomalous QHE that differs from that of SLG. As a result, it maintains a metallic nature in the regions of neutrality⁵⁰. In multi-layer graphene (MLG) there is no gap; the more layers there are, the more metallic the structure gets. MLG exhibits a very high surface area that is approximately identical to single layer of graphene.

2.2. Production Methods of Graphene

In 1975, single-layer graphite synthesis experiments were recorded in the literature with the thermal decomposition of carbon atoms on Pt substrate⁵¹. However, graphene was not a preferred material to study at that time, the inconsistency in properties observed among the layers formed on different crystal planes of Pt hinders the determination of potential applications for the synthesized monolayer graphene. Novoselov et al. in 2004, they won the Nobel Prize for synthesizing single-layer graphene using the mechanical exfoliation method and achieving the simple reproducibility of this method⁵². With the graphene synthesis methods developed in the light of this method, graphene has provided researchers with a wide field of study. This chapter of this thesis covers three important methods used in graphene synthesis.

2.2.1. Mechanical Exfoliation

As mentioned in the previous section, it is the weak van der Waals bonds that hold the graphene layers together. In theory, obtaining single-layer graphene is indeed feasible from multi-layered graphite sheets by breaking these weak bonds. These weak connections are broken and individual graphene sheets are separated through exfoliation and cleavage using mechanical or chemical energy. Novoselov et al.⁵² employed a commercially available highly oriented pyrolytic graphite (HOPG) sheet with a thickness of 1 mm for the exfoliation and created absolutely 3-5 μm deep areas by dry etching in oxygen plasma. The layers of the graphite sheet were then peeled off using a Scotch tape. It was discovered that thin flakes that had been transferred to a Si substrate included single- to few-layer graphene sheets (Figure 2.3 (a)). Later, using other materials such as BN and MoS₂, were produced as two-dimensional atomic crystals using the same approach. Figure 2.3 (b) and (c), respectively, the optical representation of graphene that was mechanically exfoliated and transferred onto a silicon wafer with a SiO₂ thickness of 300 nm. The trace highlights the contrast variations, which correspond to the different layers of graphene. Here, the single-layer graphene is showed by the lightest color on the substrate, while the few or multilayer graphene is indicated by the other flakes with increasing darker.

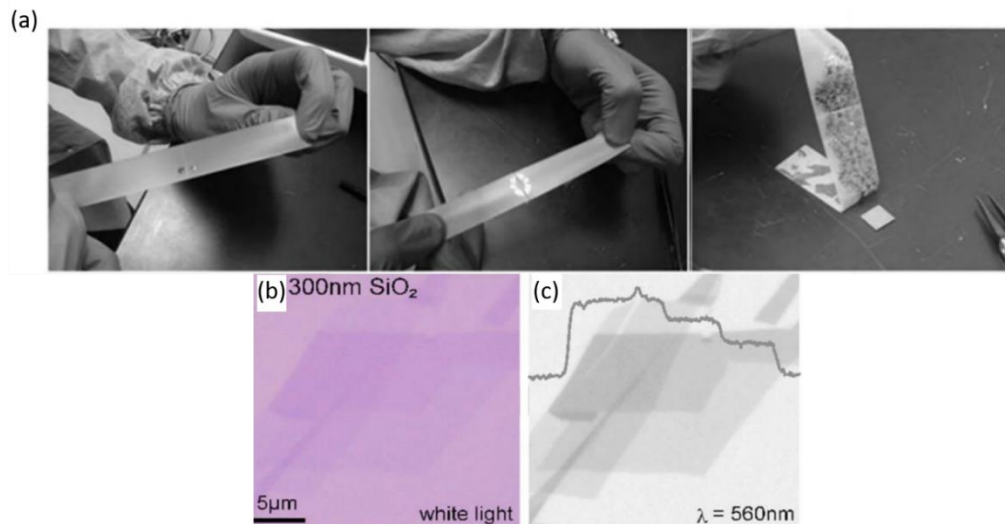


Figure 2.3. (a) Steps of synthesizing single-layer graphene by mechanical decomposition method using HOPG. Optical microscope image of mechanical exfoliated graphene transferred on SiO₂/Si substrate under (b) white and (c) green light illumination

2.2.2. Epitaxial Growth on SiC Substrate

Epitaxial growth method are widely recognized as highly popular technique for the growth of graphene. In Figure 2.4, SEM images of epitaxially growth graphene was shown. In this method relies on the decomposition of silicone on the (0001) surface plane of 6H-SiC which is used for growth material⁵³. At elevated temperatures, approximately 1450°C, silicon atoms undergo evaporation from the SiC surface, leaving behind carbon atoms that arrange themselves into a hexagonal graphene structure. On this surface, epitaxially formed graphene typically had 1 to 3 layers, with layer thickness depending on the decomposition temperature. Particularly for the semiconductor sectors, the approach of producing graphene on SiC appears appealing. It was discovered that the structures of graphene produced on SiC (0001) (Si terminated face) and SiC (000 $\bar{1}$) (C-terminated face)⁵⁴. Multilayer graphene on the SiC (0001) surface was found to exhibit unusual rotating stacking, which may account for their behavior similar to that of isolated graphene sheets. A similar strange behavior was not seen in graphene produced on SiC (0001). Another crucial issue is the structure and electronic characteristics of the interface layer between the substrate and the graphene, as this layer is known to have an impact on the graphene's characteristics. This property is positioned for industrial usage to create wafer scale graphene.

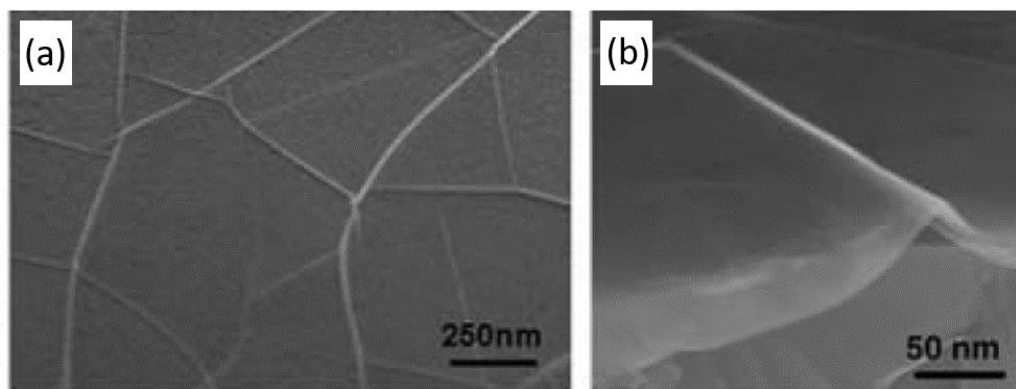


Figure 2.4. SEM images of epitaxial graphene grown on SiC (0001) surface (a) fractures and (b) wrinkles⁵⁴

2.2.3. Chemical Vapor Deposition

Chemical vapor deposition (CVD) has been the generally most used method for synthesizing graphene. In 2006⁵⁴, in literature the first study on planar few layer graphene (PFLG), a CVD-synthesized material, was discovered. In CVD graphene deposition, a quartz furnace tube is used to heat a metal substrate, while hydrogen is pumped through it at low vacuum or ambient pressure. The substrate is annealed at the high temperature, which results in an increase in the size of its grains (generally 3-5 μm) and a decrease in the thickness of the metal oxide film on the substrate surface. Typically, methane (CH_4) and hydrogen (H) are used to introduce carbon during the development stage. By altering the injecting inert diluent gas, it is possible to control the partial pressures of the hydrocarbon and hydrogen. The reaction is completed, the furnace is turned off, and the reactor is allowed to cool until it reaches room temperature. This step is crucial to prevent the deposited carbon from aggregating.

Graphene synthesis steps with CVD method are explained step by step in the Figure 2.5. The process initiates by transporting reactants within the gas flow through convection (1), after which they undergo thermal activation (2). In the subsequent step (3), the reactants move from the main gas stream to the stationary boundary layer via gas diffusion. Following this, the reactants get adsorbed onto the surface of the substrate (4) and proceed to diffuse into the substrate's bulk (5), depending on the solubility of carbon. For substrates with low carbon solubility, graphene growth takes place on the surface, where CH_4 catalytically decomposes and carbon atoms adsorb to form a graphene film. On the other hand, high solubility substrates allow carbon atoms to diffuse into the bulk, and

graphene growth occurs during the cooling step. To prevent the formation of multilayer graphene, it is advisable to cool the system rapidly. In step 6, there is catalytic decomposition of reactive species, along with surface migration towards the attachment sites. Step 7 involves desorption of the product from the substrate, and ultimately, in step 8, the products diffuse through the boundary layer back into the main gas stream (9)⁵⁵.

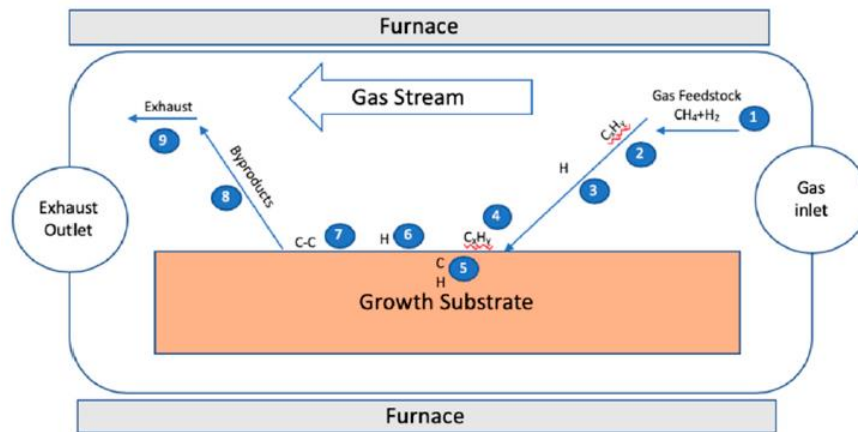


Figure 2.5. Schematic representation of CVD growth mechanism of graphene⁵⁵

2.3. Graphene Foam

The freestanding 3D graphene macroscopic structure known as graphene foam (GF) has captured the interest of many researchers from various domains for both application and basic research. Basically, GF is a 3D macroscopic, defect-free graphene architecture with sub micrometer to several micrometer pore diameters. GF has a porous⁵⁶, large surface area structure⁵⁷ that is mostly created via a technology called chemical vapor deposition. In order to create a material with high conductivity, good strength, and flexibility, standard 2D graphene's cutting-edge mechanical and electrical properties are combined with those of metallic foam^{58,59}.

2.3.1. Structure of Graphene Foam

As mentioned in previous section, the individual graphene sheets have van der Waals interactions across planar 2D structures, which reduces the amount of surface area

that is accessible. GFs, on the other hand, are 3D architectures free of flaws. The number of layers in the graphene film has a significant impact on the specific surface area of 3D GFs⁶⁰.

Moreover, the sub-micrometer to several micrometer range of pore sizes in the GF confers several advantageous properties, including, compressibility, excellent conductivity, and exceptional adsorption characteristics^{61,62}. The presence of a macro porous structure not only hinders the aggregation and restacking of individual graphene flakes during the assembly process but also ensures ample contact area between the electrolyte and electrode, as well as generous adsorption space. In Figure 2.6, the SEM images of 3D porous GF was shown. Pore sizes may differ depending on the 3D GF magnification method. The pores of the GF are substantially smaller than the pores of graphite foams generated by CVD on commercially available nickel foams, which are in the range of 200-500 μm . The pores of the graphene foam vary from a few hundred nanometers to about 60 μm . Additionally, the foam's pores on both its exterior and internal surfaces are connected to one another and extend in all directions, creating a massive 3D structure. This three-dimensional porous framework facilitates the high-rate transportation of electrolyte ions and establishes multidimensional pathways for electron transport^{63,64}. Consequently, these features result in outstanding electrochemical performance. Furthermore, this freestanding GF exhibits distinctive electrochemical, mechanical, oil-absorbing, and biocompatible properties, which render it highly attractive for applications in electronic devices and related fields.

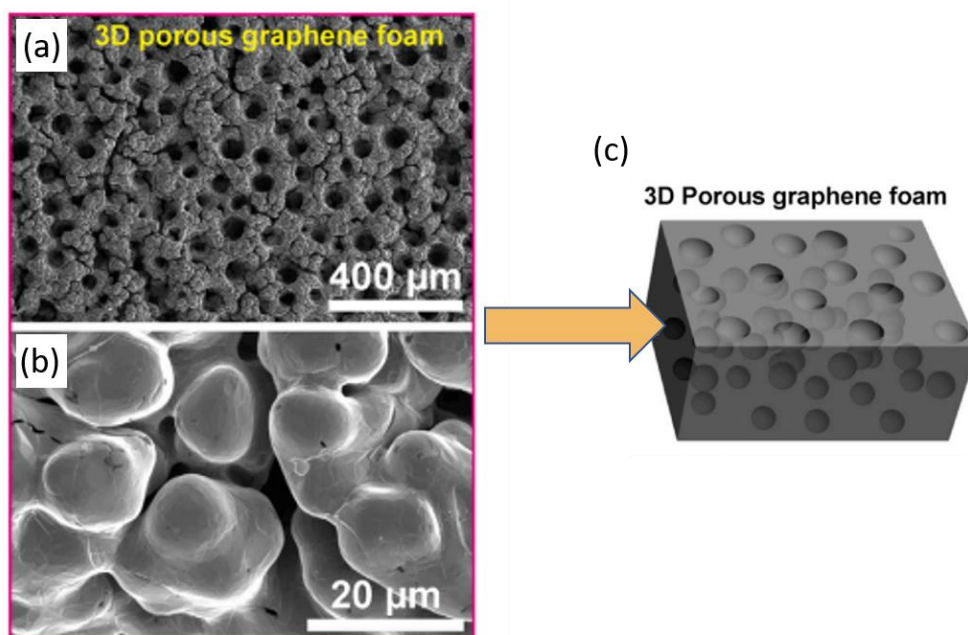


Figure 2.6. (a) Low and (b) high resolution SEM image and the porous graphene foam after removal of the Cu/Ni template (c) Schematic representation of 3D GF

Additionally, the three-dimensional porous framework facilitates the high-rate transportation of electrolyte ions and establishes multidimensional pathways for electron transport. Consequently, these features result in outstanding electrochemical performance. Furthermore, this freestanding GF exhibits distinctive electrochemical, mechanical, oil-absorbing, and biocompatible properties, which render it highly attractive for applications in electronic devices and related fields.

2.3.2. Synthesis of Graphene Foam

Several methods of 3D GF synthesis have been reported. The manufacturing of this intriguing material primarily uses two approaches: template techniques and nontemplate techniques. Two varieties of the template techniques exist: The soft-template, which uses supramolecular agglomerates such as micelles and emulsions as templates, and the hard-template, which uses hard and nanostructured porous metal foams, such as nickel foams, as templates. In this section, the CVD method, which is the most preferred method in GF synthesis, will be explained in detail.

2.3.2.1. Chemical Vapor Deposition Technique

The synthesis and transfer steps of GF by chemical vapor deposition method (CVD) is shown schematically in Figure 2.7 (a). The growth process of the GF involved four steps. Initially, a nickel substrate of appropriate size was positioned at the center of the CVD furnace tube. Subsequently, a vacuum of approximately 101 Torr was created using a rotary pump, and a gas mixture of hydrogen and argon (comprising 75% argon and 25% hydrogen) was introduced throughout the experiment. In the third step, the temperature of the CVD furnace tube was gradually raised from room temperature to 1100°C at a rate of 10°C per minute (Figure 2.7 (b)). Finally, the nickel foam substrate was annealed at 1100°C for 10 minutes, and a third gas, namely ethylene (C_2H_4), was introduced into the gas mixture (argon + hydrogen) as a carbon source. Once the CVD process reached room temperature, the specimens were removed. Notably, the color of the nickel substrate changed from grey to dark grey after the deposition of graphene (as depicted in Figure 2.7 (c)). To separate the graphene film, the prepared sample was immersed in an aqueous solution of iron chloride ($FeCl_3$) for 48 hours. As a result, the graphene film began floating on the surface of the solution after the nickel substrate had been etched away.

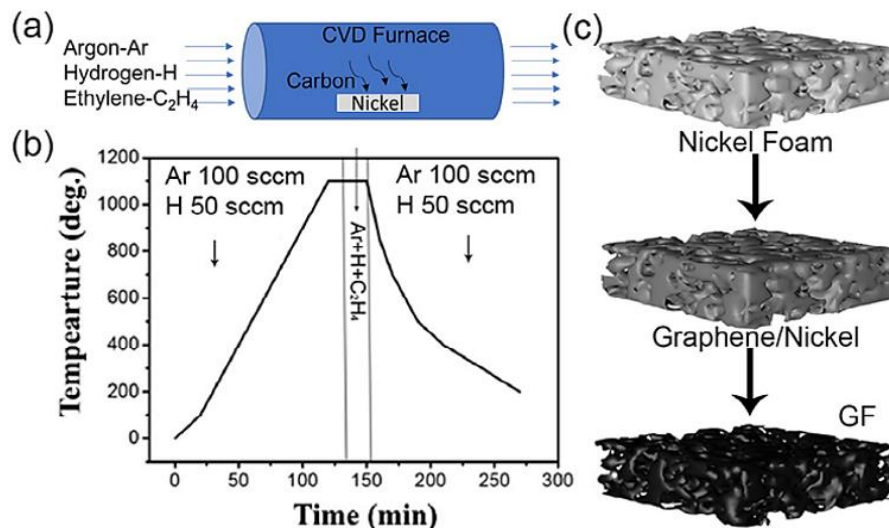


Figure 2.7. Schematic representation of (a) CVD (b) growth parameters and (c) transfer process

2.4. Graphene Field Effect Transistors

Bardeen and Brattain were the first to study FETs in 1948⁶⁵. FETs are currently the most often employed components in common place technical applications. Graphene-based FETs field effect transistors consist of a graphene channel sandwiched between two electrodes, as seen in Figure 2.8. The GFET channel's surface is functionalized with binding receptor molecules for the particular target of interest, opening the door for biological and chemical applications of sensor technologies.

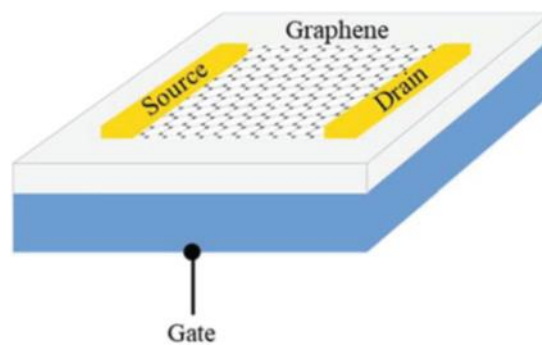


Figure 2.8. Schematic illustration of GFET structure

As shown in Figure 2.9 (a), a conventional GFET is made up of a gate, a channel region linking the source and drain electrodes, and a barrier separating the gate from the channel. To allow its electric charge to tune the channel, a control electrode known as a gate is positioned extremely close to it. The gate of a GFET regulates the flow of carriers (electrons or holes) from the source and drain. The part of the channel known as the source is where carriers enter, and the part known as the drain is where carriers leave. Channel conductivity management is necessary for a conventional GFET to function. Both n-type and p-type semiconductor channels are possible (see Figure 2.9 (b) and (c)). It is an excellent candidate for a variety of transistor applications due to its low noise⁶⁶, low power⁶⁷, enormous dynamic range⁶⁸, and high input impedance at extremely low frequencies⁶⁹.

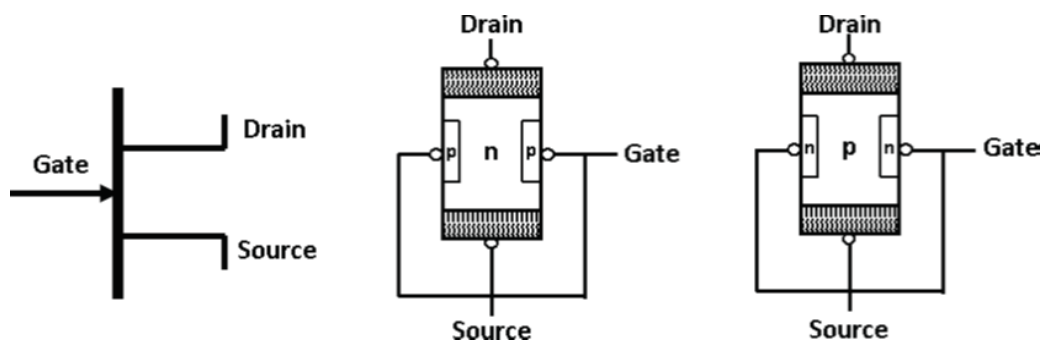


Figure 2.9. Schematic representation of (a) typical FET (b) n-channel FET and (c) p-channel FET structures

GFETs provide a crucial foundation for a diverse range of applications in biochemical sensing, such as electrochemical sensors, pH sensors, ion sensors, and more. One specific area where GFETs have garnered significant attention is in the design of GFET, leveraging the tunable band gap of the two-dimensional graphene structure⁷⁰. This field effect opens up avenues for both experimental and theoretical exploration in utilizing GFETs for high-performance chemical and biological sensors, thereby offering promising prospects in biological and medical applications.

2.4.1. Characteristics of GFETs

Gate geometries of GFETs have undergone enhancements to elevate the performance of the devices. Primarily, there exist three distinct gate configurations in transistor devices, namely top-gated, bottom-gated, and liquid-gated (Figure 2.10). These configurations have been refined to optimize device performance and offer improved functionality.

The top-gated configuration is the most prevalent in GFETs, where the gate is positioned on top of the semiconductor and connected through an insulating layer (Figure 2.10 (a)). In graphene, altering the top gate voltage leads to modifications in the barrier shape and carrier densities. To ensure effective electrostatic control of carrier density, the horizontal overlap between the top gate and the source/drain layers should be greater than the thickness of the top gate insulator. However, excessive overlaps are undesirable due to the resultant increase in gate-to-channel capacitances⁷¹.

The back-gated configuration (Figure 2.10 (b)) is often favored by researchers due to its ease of design implementation. In this configuration, a typical back-gated GFET

involves the growth of a 2D material on a Si wafer that has been oxidized. The channel dimensions are defined, and metal contacts are deposited. The back-gated arrangement, where a graphene flake is placed on a substrate and contacted between the source and drain electrodes, with the substrate serving as the back gate, is the most extensively studied GFET structure. Additionally, an additional insulating layer and a top-gate electrode can be added on top of the device, with both gates regulating the carrier concentration in the channel^{72,73}.

In the liquid-gated configuration as seen in Figure 2.10 (c), the electrochemical potential of the charge carriers can be adjusted by varying the top gate voltage. This configuration resembles the top-gated arrangement, with the distinction that a reference electrode is utilized to apply the gate voltage to the electrolyte. Some research teams have recently explored the utilization of graphene in aqueous electrolytes, demonstrating its potential for various applications in biosensors and bioelectronics⁷⁴. The pioneering work on liquid-gated GFET biosensors using Si devices was investigated by Bergveld⁷⁵. The introduction of this innovative concept has unlocked exciting prospects in the advancement of liquid-gated GFET biosensors, showcasing great potential for various applications in the field.

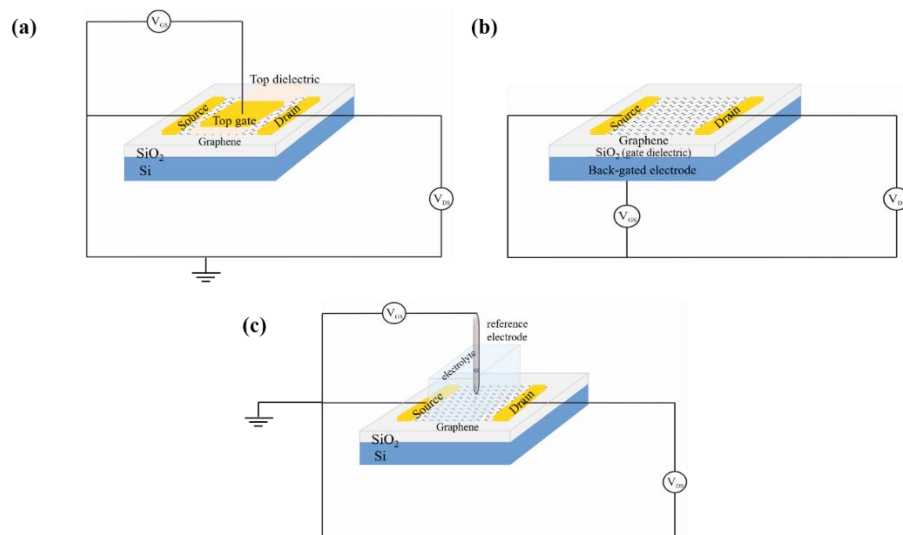


Figure 2.10. Schematic representations of (a) top-gated (b) back-gated and (c) liquid gated GFET device structures

Liquid-gated GFETs are anticipated to exhibit high sensitivities due to several key factors, including the following. Enhanced Carrier Mobility: Graphene possesses significantly higher carrier mobility compared to other semiconductors. In liquid-gated

GFETs, this attribute contributes to higher transconductance, enabling improved sensitivity. Voltage Stability: Liquid-gated GFETs can serve both as sensors and amplifiers, resulting in minimal voltage variation. This stability is advantageous as it enables the device to maintain consistent and accurate measurements. Low Operational Voltage: Liquid-gated GFETs operate at low voltages, making them highly sensitive to even slight potential changes. This characteristic allows for the detection of small variations in the input signal, enhancing the overall sensitivity of the device.

These combined factors contribute to the high sensitivity exhibited by liquid-gated GFETs, making them promising candidates for applications requiring precise and responsive sensing capabilities⁷⁶.

2.4.2. GFET Working Mechanism

Electrical characterization is used to build a device with 2D materials as its first stage. The measurement of I_D - V_G curves is typically used to characterize FETs. Two key states can be defined for these devices: "on" and "off". In a typical FET device, current travels through a semiconducting material channel (drain) from one contact (source) to a second contact. When the semiconductor channel exhibits electrical conductivity, allowing current to flow freely, the FET is considered "on". Conversely, if the semiconductor exhibits high resistance, only a small amount of current flows, and the FET is considered "off". The conductance of the semiconducting channel is controlled by the gate. In the case of GFET structures, the semiconductor channel is made of graphene. While pristine monolayer graphene lacks a band gap, it is possible to induce a band gap through doping and the application of an electric field, thereby exhibiting semiconducting properties. Additionally, the I_D - V_D curve, which represents the relationship between the source-drain voltage (V_D) and the drain current (I_D) for a given bias voltage, plays a crucial role. For semiconductor materials, this relationship includes a saturation region, divided by a cutoff I_D , which occurs as the source-drain voltage increases.

In FET structures, the channel length (L) and width (W) play a vital role in electrical characterizations. The relationship between these parameters is expressed by equation 2.1 where I_D represents the drain current, μ denotes the mobility, C_{ox} represents the capacitance of the oxide layer, V_G signifies the gate voltage, V_{th} represents the threshold voltage, and V_D represents the drain voltage. These parameters collectively

determine the behavior and performance of the FET structure during electrical characterization.

$$I_D = \mu C_{ox}(W/L)(V_G - V_{th})V_D \quad 2.1$$

The performance of GFETs is characterized by three key parameters: the on/off current ratio (I_{on}/I_{off}), contact resistance (R_c), and carrier mobility (μ). The gate voltage is important for controlling the current when the drain-source voltage is held constant. I_{on}/I_{off} represents the ratio of current flowing through the transistor in the "on" state to the current in the "off" state. This ratio is significant in determining the suitability of the device for specific applications. The threshold voltage (V_{th}) of a transistor is the voltage at which it switches from the "off" state to the "on" state. If the applied gate voltage (V_G) is less than V_{th} , the transistor remains in the "off" state.⁷⁷ Additionally, a subthreshold leakage current, known as weak inversion current, is measured. This leakage occurs due to the thermal energy of charge carriers, resulting in the flow of highly energetic electrons through a closed channel. Carrier mobility is another important factor in assessing device performance. It quantifies the ease with which charge carriers move through the transistor, impacting its frequency performance. Enhancing mobility is a critical aspect of improving the performance of the transistor⁷⁸.

In light of electrodynamic behavior, the interface created between liquid and solid surfaces in GFET structures is a very fascinating subject. Debye-Hückel screening approximation⁷⁹ is the key description in creating better bioelectronics for GFET applications. The Debye length (λ_D) serves as a fundamental measure of the overall electrostatic impact exerted by charge carriers in solutions. The ionic solutions filter the analyte charge and result in the formation of an electron double layer on the sensor surface. The buffer concentration at high ratios determines the length of the analyte scan. As a result, only interactions taking place close to the electrode surface can be detected with sufficient sensitivity in the GFET⁸⁰. Due to this characteristic, the sensitivity of analyte detection in GFETs is constrained to interactions taking place in close proximity to the electrode surface. The Debye length (λ_D) for ionic liquids or electrolytes can be determined as in equation 2.2,

$$\lambda_D = \sqrt{\frac{\epsilon_r \epsilon_0 k_B T}{2N_A e^2 I}} \quad 2.2$$

where ϵ_r is the dielectric constant of the electrolyte, ϵ_0 the dielectric constant of vacuum, k_B is Boltzmann's constant, T is the temperature, N_A is Avogadro's constant, e is the unity of charge, and I is the electrolyte's total ion strength⁸¹.

2.4.3. GFET Medical Diagnostic

For the patient to receive the best treatment possible from the medical staff, a proper diagnosis is essential. Additionally, it takes time and may be crucial for the patient's life to evaluate their symptoms during the diagnostic process. Recent research studies have revealed that significant resources and effort have been devoted to expediting the diagnosis procedure while also increasing its accuracy.

The diagnostic process is a difficult, collaborative approach that focuses on the patient and identifies the patient's health issues through an expert evaluation of accumulated symptoms¹⁸. Only an accurate diagnosis made at the appropriate time has the possibility of producing a successful result. In order to define and organize the process, a model that depicts the diagnostic process has been created. Recent research has shown that GFETs can assist in resolving issues that arise during medical diagnosis. Sensing gases or volatile organic molecules, for instance, is essential for regulating chemical reactions, environmental monitoring, and health protection. The detection of toxic gases in human breath or the identification of volatile organic compounds produced by lung cancer⁸² in human breath is crucial for maintaining human health. However, there may be some issues due to the expensiveness and low sensitivity of the instruments employed in these diagnostic techniques. With FETs made of graphene, these diagnostic issues can be resolved. Since Novoselov's group first revealed that graphene-based gas sensors could detect gas molecules adhering to or leaving the graphene surface in 2007⁸³, it has been possible to use GFET to determine harmful volatile compounds in low concentrations in human breath as well as various types of gases. Completely electronic and label-free sensing techniques are another issue with medical diagnosis that can be resolved with GFET. The environment has an impact on a graphene's electrical conductivity, and the surface adsorption of various substances and biomolecules has a significant impact. Thus, extremely encouraging choices for label-free biosensing include graphene-based FETs⁸⁴. In addition, for NH_3 sensing, Gautam and Jayatissa⁸⁵ improved CVD growth in back-gated GFET. Their findings indicated that the device displayed two

distinct adsorption peaks for the target gas at ambient temperature and one adsorption peak at a higher temperature of about 100 °C. Dirac peak's average shifting rate was determined to be 0.49 V/ppm at 100 ° C.

In comparison to other nanostructured materials, graphene's 2D structure gives an outstanding surface area-to-volume ratio⁸⁶ and exhibits no separation between a layer and the bulk material, which is necessary for great sensitivity. This makes it a perfect option for chemical sensing applications. Additionally, graphene's ambipolarity⁸⁷ permits chemical gates to be created by either electron-donating or electron-withdrawing groups. Kim et al.⁸⁸ depicted the effects of temperature and humidity on the sensitivity to NO₂ and NH₃ gas. As a result, an increase in temperature led to an increase in the drain current for NO₂ and an opposite effect for NH₃ gas. According to their results, NH₃ and humidity combine to generate NH₄OH, which acts as a donor on the graphene surface and lowers the drain current. Hwang et al.⁸⁹ investigated the ethanol-selective behavior of a chemoresistor with a tin oxide nanofiber structure that was decorated with silver nanoparticles. Additionally, it was demonstrated that after being decorated with silver nanoparticles, tin oxide nanofibers responded to ethanol up to four times more strongly. However, once the silver nanoparticle ratio beyond a certain threshold, the response decreased once more. In this study, the higher adherence of ethanol to the tin oxide nanofiber partially covered with silver nanoparticles was attempted to explain the synergistic effect in the hybrid chemoresistor. Hybridizing graphene is another option for enhancing sensing capacities²⁶. Loan and his team created graphene/MoS₂ heterostructures for DNA hybridization detection. On top of a monolayer of crystalline CVD MoS₂, graphene was layered. Due to the hybrid film's photoluminescence properties, their technology demonstrated selective detection of DNA hybridization. By inhibiting the reaction between molybdenum disulfide (MoS₂) and the surrounding environment, the graphene layer acts as a protective layer. MoS₂'s photoluminescence intensity rose as target DNA concentration did. DNA recognition was detected at low detection levels of 1 aM with the discrimination of complementary and one-base mismatched target DNA using the combination of two separate semiconductors.

2.4.4. Point of Care for GFET

One of the most important biosensor applications is point-of-care testing (POCT), which offers various benefits. The most well-known benefit is the availability of diagnostic or prognostic tests close to the patient. POCT distinguishes out because it offers quick results and is simple to use without using expensive or complicated instrumentation. With expanding technological possibilities, POC diagnostic tools serve a crucial role in health systems, particularly in the diagnosis and follow-up of disorders. Creating a structure that can test several substances in intricate samples is one of the goals of the POC test, which has many advantages. POC testing, which enables the shift from conventional diagnostic tests to close to the patient in clinical laboratories, aids doctors in making the best decisions regarding diagnosis and treatment and significantly facilitates their work in this area.

Numerous biosensor techniques have been improved as a result. As a result, numerous sensing techniques using GFET-based DNA sensors were created, including electrochemical GFET⁹⁰, liquid-gated GFET⁹¹, and back-gated GFET⁹² DNA-based GFET that follow a recognized DNA detecting process. In biorecognition, brief DNA probes that are crucial to the target DNA are used. The target DNA on the sensor surface is captured and bound using DNA probes. Using a platinum nanoparticle (PtNP), Lei and colleagues⁹³ showed that rGO-FET immunosensor technology is an excellent detector of a protein-specific biomarker of heart failure. This investigation led to the development of a label-free, portable, easily deployable, and highly sensitive protein biosensor for point-of-care early detection, diagnostic, and prognostic evaluation in patients with heart failure. The relationship between brain natriuretic peptide (BNP) and anti-BNP may be discovered at 100 fm in liquid-gated investigations. On the other hand, Cr/Au/Cr contacts and a polydimethylsiloxane (PDMS) microfluidic component, Xu et al. employed CVD graphene switched onto a SiO₂/Si substrate. The 41-mer DNA probe was attached to the graphene surface using the well-known streptavidin-biotin tying method. Injections of streptavidin, biotinylated 41-mer single-stranded probe DNA, and biotinylated bovine serum albumin (BSA) were made in that order. When the eight GFETs were subjected to 100 fM of the target miRNA, a pronounced negative shift was seen because of the influence of electron doping for DNA hybridization on the graphene channel.

CHAPTER 3

EXPERIMENTAL METHODS

3.1. Device Fabrication

3.1.1. Graphene Foam Synthesis with Chemical Vapor Deposition (CVD) Method

Graphene foams are made by growing graphene using a CVD process on a 3D metal foam structure and multilayer graphene (MLG) structure occurs. A typical CVD method for MLG growth is divided into 4 phases as shown Figure 3.1. In the ramp-up phase, after the substrate with catalyst is loaded into the chamber and flushed with inert gas, the temperature of the chamber is gradually raised in Ar and H₂ environment. For MLG synthesis, an approximate 20 °C/min increase in temperature was chosen. Subsequently, in the annealing phase, the substrate is maintained at a fixed temperature of 1000 °C in Ar/H₂ environment to remove native oxide layer on the nickel (Ni) foam substrate. In the growth phase, precursor gases are injected into the chamber to initiate the growth of MLG on the Ni foam. Here, the Ni catalyzes the breakdown of the gaseous carbon precursors and the carbon dissolves into the Ni foam. After a stipulated amount of growth time, in the cooling phase, the chamber is cooled back down to room temperature. The sample is removed from the heated region for quenching to successfully synthesize MLG. The dissolved carbon will precipitate on the surface of the Ni foam during the cooling process. The Ni foam herein therefore has an additional function of providing a template for the MLG to precipitate.



Figure 3.1. CVD growth system for graphene foam

3.1.2. Epitaxial Growth of Graphene

The epitaxial growth method is a SLG synthesis method on silicon carbide (SiC) substrate when the relevant parameters are used. Epitaxial graphene was grown using the direct current heating method on a SiC substrate within an ultra-high vacuum (UHV) chamber, maintaining a base pressure of approximately 10^{-10} mbar. In its simplest terms, the epitaxial growth method can be explained as the formation of graphene structure by annealing the SiC substrate at high temperature, evaporating the Si atoms from the surface, and forming a hexagonal lattice of the remaining C atoms⁹⁴. The UHV chamber and controller panel was shown in Figure 3.2 (a) and (b). SiC substrates were diced into 4 mm x 10 mm sizes and placed in epitaxial growth chamber. To remove the nature oxide layers on diced SiC substrate, diced SiC pieces were kept in 15% hydrofluoric acid (HF) solution for 3 minutes. After washing with distilled water 3 times, it is dried with nitrogen gas. Before the growth process, the samples were placed in the UHV chamber and subjected to overnight degassing at 600 °C. This step is essential to thermally clean the organic substances and potential contaminants from the sample surface. SLG was grown on SiC substrates under UHV conditions. The substrates were heated to 1050 °C for 5 minutes to eliminate the native oxide layer from the surface. Subsequently, the temperature was raised to 1300 °C for 7 minutes to promote grain boundary enlargement. Prior to SLG growth, this protocol was implemented for all the samples. Subsequently, the temperature was raised to 1350 °C for a duration of 3 minutes to facilitate the

evaporation of Si atoms. As a result, the remaining carbon atoms formed the SLG on the substrate's surface. (Figure 3.2 (c)).



Figure 3.2. a) Ultra-high vacuum epitaxial graphene growth set up b) control panel and c) graphene growth at 1350 °C

3.1.2.1. Deposition of SiO₂ with Thermal Evaporation System

After the growth of epitaxial graphene, 15 nm thick SiO₂ film was deposited by the thermal evaporation (TE) system to obtain wrinkled structure (Figure 3.3). There are 4 different targets which are SiO₂, Au, Ni, Cr. For the evaporation of SiO₂, tungsten (W) basket was used. During the deposition process, the current and power settings were adjusted to 40 A and 217 W, respectively. Evaporating SiO₂ atoms accumulate in the quartz crystals and when they reach the set thickness, the shutter closes, breaking the relationship between the substrate and the evaporating SiO₂ target in tungsten boat. While depositing the SiO₂ thin film, the temperature of the sample was recorded as 60°C. Following the deposition stage, the sample was gradually cooled down to room temperature (around 24°C) within the vacuum chamber before being transferred to the ambient environment.



Figure 3.3. Thermal evaporation system for SiO₂ deposition

3.1.2.3. Deposition of SiO₂ with Pulsed Electron Deposition

Pulsed Electron Deposition (PED) is a relatively unexplored thin film deposition technique. It is determined by the target's thermal conductivity, heat capacity, and other material qualities as well as the range of electrons present. In PED, the high-power electrons can strongly couple to the target material (SiO₂), leading to SiO₂ film deposition⁹⁵. After the growth of epitaxial graphene, samples were placed sample holder and 100 nm thick SiO₂ film was deposited by PED system. The encapsulated SiO₂ was grown 100 nm thick under 5.5 mTorr O₂ pressure with 9.5 kV discharge voltage under room temperature conditions (Figure 3.4).

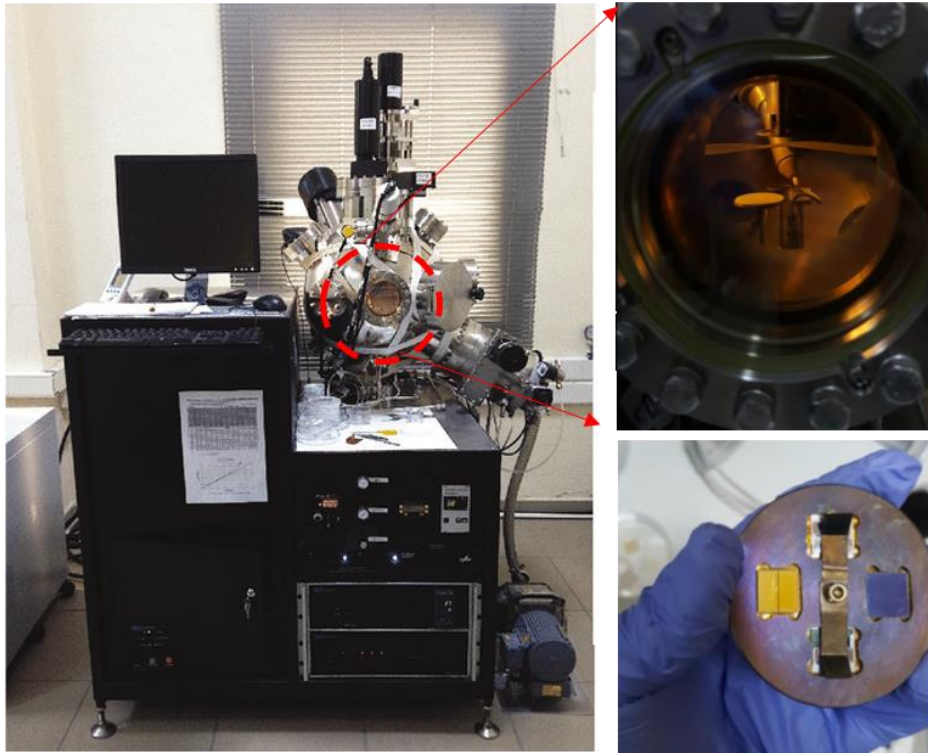


Figure 3.4. Pulsed Electron Deposition (PED) system for SiO₂ deposition

3.1.3. Chemical Vapor Deposition (CVD) Growth of Graphene

Bilayer graphene (BLG) was grown on 25 mm thick Cu foil by chemical vapor deposition (CVD) process. The CVD chamber (Figure 3.5) was prepared by placing the Cu foil inside and evacuating it to 4 Torr while maintaining an annealing temperature of 1035 °C. The growth reaction for BLG was conducted at 1035 °C for 60 s by introducing 10 sccm of methane (CH₄). Following the growth process, the furnace was gradually cooled down to room temperature under atmospheric pressure (760 Torr). BLG grown on copper foil was transferred onto glass substrate. For this, Microposit S1813 G2 photoresist (PR) were drop-cast onto graphene that was holding Cu surfaces. The photoresist was allowed to harden gently in an oven at 70 °C overnight. The hardened photoresist on the graphene holding Cu was then placed into a ferric chloride (FeCl₃) solution to etch the Cu foils. Once the Cu foil was completely etched away, the graphene holding the photoresist was placed into DI water for 30 minutes to remove any FeCl₃ residues. The sample was then exposed to 70 °C for 30 seconds and 120 °C for 2 minutes to reflow the photoresist on the graphene. During the reflow process, the photoresist liquefies and releases the graphene layers onto the target substrate. Removing the

photoresist with acetone yields a large area of graphene on the desired substrate. This process is crucial for producing high-quality graphene on specific substrates for various applications.

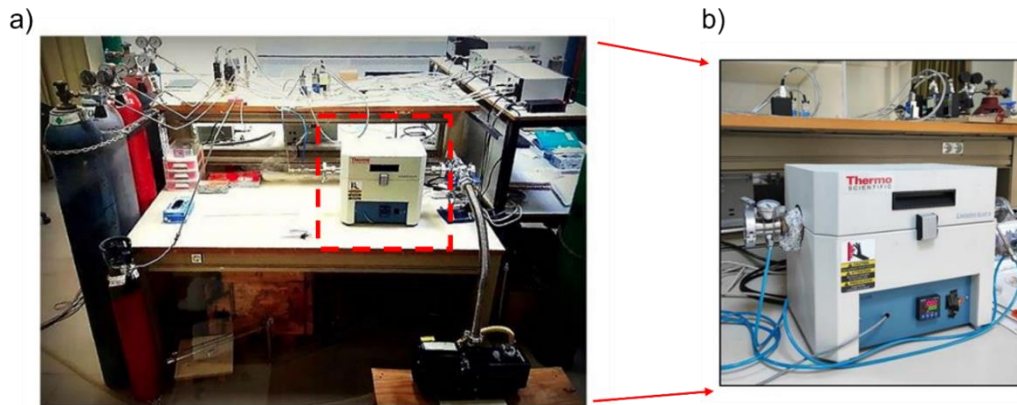


Figure 3.5 a) The CVD growth set-up and b) furnace for BLG growth

3.1.4. Gas Sensor Platform Fabrication

PMMA has been preferred to create for gas sensor platform because it is a flexible and easily shaped polymer. Polymer nanofibers obtained by electrospinning method will be fiberized on PMMA substrate to suspended structure. The sensor substrates were designed with various sizes and models, and they were transmitted to the Laser Cutter device's interface using the CoralDraw x8 designing program before the PMMA plate was cut. The PMMA substrate, which consists of 11 different patterns, was cut using a laser cutter using various parameters to build a sensor platform that provides the best efficiency and enables the nanofibers to be coated using the electrospinning method to hang on the surface. The PMMA layer with the dimensions of 300 x 400 mm and 3 mm thickness was cut with the Epilog Zing Laser Cutter device in sizes suitable for sensor production which was shown in Figure 3.6.

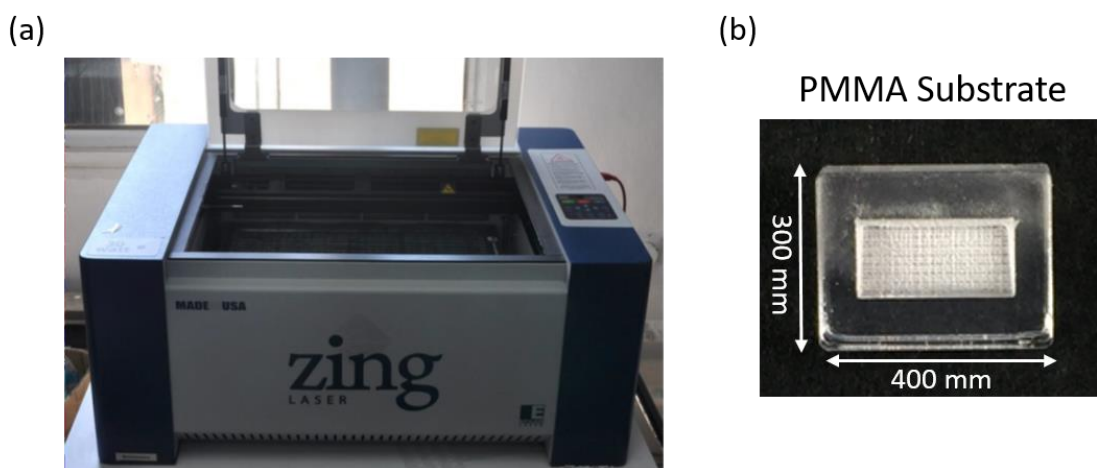


Figure 3.6. Image of Laser Cutter b) digital image of designed PMMA sensor substrate after cut via Laser Cutter

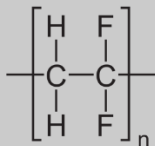
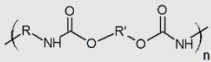
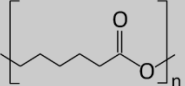
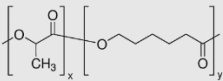
3.1.4.1. Nanofiber Production

An adaptable and practical method for creating ultrathin fibers is electrospinning. Developing electrospinning techniques and creating electrospun nanofibers that fit or enable numerous applications has advanced remarkably⁹⁶. Nanofibers were produced from polymeric materials using the electrospinning technique. This technique produced uniform, nano- or micron-sized fibers in a manageable way. Three major components make up the electrospinning apparatus employed in this technique: a metal needle, a power source, and a collector. A syringe is used to deliver the pre-prepared dense polymer solution (in this study, these are PVDF, PU, PCL, PLLCL) to the metal needle at a steady rate. The polymers used and their chemical structures are presented in detail in Table 3.1.

Poly (L-lactide-co- ϵ -caprolactone) (PLLCL) nanofibers were fabricated by electrospinning technique. 1.435 g PLLCL (10wt %) was weighed in 20 mL vial and dissolved in 9 mL of DCM and 1 mL of DMF solvent mixture and mixed on magnetic stirrer for one day. After PLLCL completely dissolved, 20 mL syringe was filled with polymer solution and connected to syringe pump of the electrospinning set up. The same procedure was performed with PCL and PU nanofibers. PMMA substrates placed on aluminum foil were placed in the collector. Electrospinning was performed for twenty-five minutes. Electrospinning parameters were adjusted as indicated; 25kV voltage, 3mL/h flow rate, 180 mm tip collector distance.

A 25 ml vial was used to weigh 4.38 g of PVDF, which was then dissolved in a mixture of 20 mL DMF and 4 mL Acetone to create a 25% wt. polymer dispersion. A magnetic bar was added to the vial, and the dispersion was sealed before being placed under a stirrer. It was stirred at 60°C and 300 rpm for a day. The next day, the fully dissolved solution was transferred to a 20 mL syringe and connected to a syringe pump in the electrospinning instrument. The instrument's collector was coated with aluminum foil. Each PMMA substrate prepared in the previous section was positioned at the center of the collector with a 2 cm spacing. Up to 12 substrates were electrospun simultaneously. The instrument parameters were set as follows: a flow rate of 5 ml/h, a distance of 170 mm, and an applied voltage of 24 kV. Additionally, the collector rotation was set to 500 rpm. Each set of devices underwent electrospinning for two minutes.

Table 3.1. The polymers used in the study and their chemical structures

POLYMER	CHEMICAL NAME	CHEMICAL STRUCTURE
PVDF	Polyvinylidene fluoride	
PU	Polyurethane	
PCL	Polycaprolactone	
PLLCL	Poly(L-lactide-co-caprolactone)	

The power source's electric current induces the polymer solution to accumulate at the needle's tip. The liquid jet starts to expand up to the collector and develops a filamentous structure. As it stretches, the solvent in the liquid jet evaporates. As a result, the collector is constantly being filled with nanometer-sized polymer fibers. Figure 3.7 shows the electrospinning apparatus that we employed in the investigations. The device's

configuration dictated that the electrospinning process be done axially. It is possible to alter the flow rate of the polymer solution, the applied potential difference, the collector rotation speed, and the collector-needle distance in order to implement the electrospinning method. These characteristics could be altered to produce nanometric and micrometric fibers.

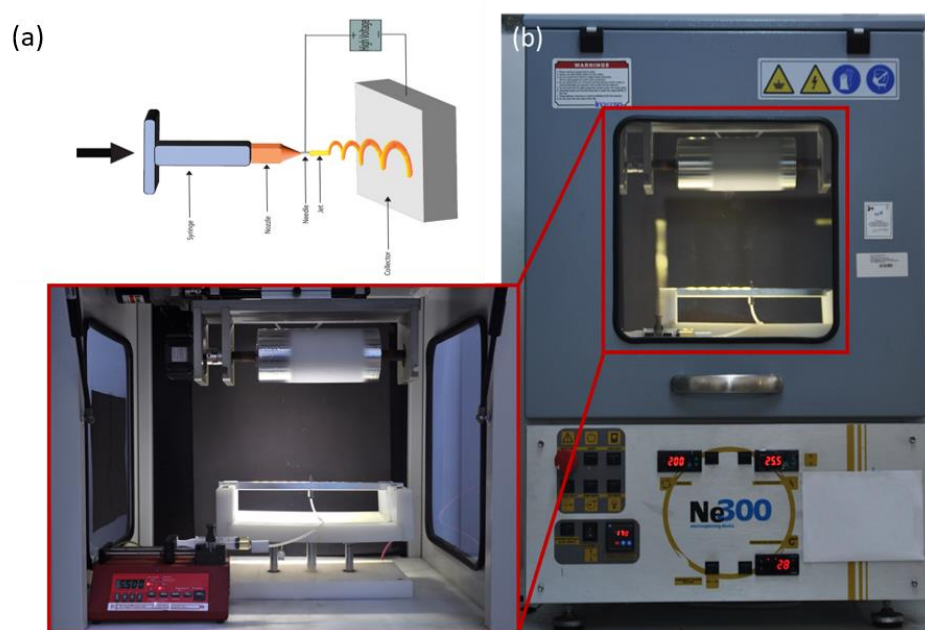


Figure 3.7. (a) Schematic representation of the electrospinning device (b) The electrospinning device we used in the studies

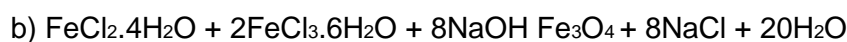
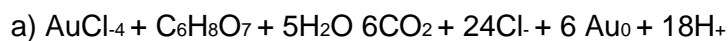
3.1.4.2. PEDOT: PSS and MWCNT Preparation

The nanofibers produced by electrospinning were modified with conductive conjugated MWCNT and PEDOT:PSS to form the sensor interface. The PEDOT:PSS dispersion was used without undergoing chemical treatment, while the MWCNT was treated with acid before use to increase the electrical conductivity⁹⁷. For acid treatment of MWCNT, 0.1 g of MWCNT is weighed and transferred to an erlenmeyer flask. Next, a mixture of 4 ml H₂SO₄ and 1.6 ml HNO₃ solution is poured onto the MWCNT, and the resulting mixture is sonicated for 1 hour before being left in a fume hood overnight. Then, 1.6 ml of HCl is added to the solution, followed by the slow addition of a total of 20 ml of NH₄OH solution to the mixture until gas release ceases, in order to neutralize it. Once the pH reaches 7, the solution is filtered through a 0.2 micron cellulose acetate filter paper. The filtered product is transferred to a erlenmeyer flask, and distilled water is added until

the solution's pH falls within the range of 5.5 - 6. The solution is filtered again, this time using a 0.2 μm porous filter paper. Finally, the resulting product is dried in a drying oven for 2 hours at 40 $^{\circ}\text{C}$. A 0.2% dispersion by weight of both conductive elements was prepared and coated onto the PVDF, PU, PCL and PLLCL polymers using a 40 μL dropper method. The coated polymers were then kept in an oven at 60 $^{\circ}\text{C}$ for 3 hours. To obtain ohmic contacts, the contact points of the conductive elements with copper tape were coated with silver paint.

3.1.4.3. Synthesis of Metal Nanoparticles

Gold (Au) and iron (Fe) were doped with nanoparticles to improve the sensors' selectivity and ability to store organic volatile compounds. The Turkevich method was used to create gold nanoparticles⁹⁸. This procedure involved heating 98 mL of distilled water in a 200 mL flask using an oil bath and a magnetic stirrer until the temperature reached 100 $^{\circ}\text{C}$. Then, 2 mL of a solution containing 12.7 mM chloroauric acid (HAuCl_4) was added. After that, water-dissolved sodium citrate ($\text{C}_6\text{H}_5\text{Na}_3\text{O}_7$) was added to the reaction solution. The yellow Au^{+3} ions were converted to colorless Au^{+1} ions by adding sodium citrate solution to the medium, and by the end of the eighth minute, the solution's hue had changed from translucent to purple, red, and blue. The resulting Au nanoparticles were purified from excess sodium citrate molecules by centrifugation and washing processes. The reaction mechanisms of Au and Fe nanoparticle synthesis are as follows:



Co-precipitation was used to reduce Fe^{2+} and Fe^{3+} ions at room temperature, resulting in the creation of Fe nanoparticles. Using this technique, 80 mL of ultrapure water was used to dissolve 4.17 g of ferric chloride hexahydrate ($\text{FeCl}_3 \cdot 6\text{H}_2\text{O}$) and 1.52 g of iron chloride tetrahydrate ($\text{FeCl}_2 \cdot 4\text{H}_2\text{O}$). 1 drop per second of 6 mL of 35% NH_4OH was added to the resultant solution. By using magnetic filtration to extract it from the solution, the resulting black Iron (II, III) Oxide (Fe_3O_4 ($\text{FeO} \cdot \text{Fe}_2\text{O}_3$)) precipitate was then washed with water. After this process was repeated 4 times, it was dried in an oven at 60 $^{\circ}\text{C}$ and made ready for use.

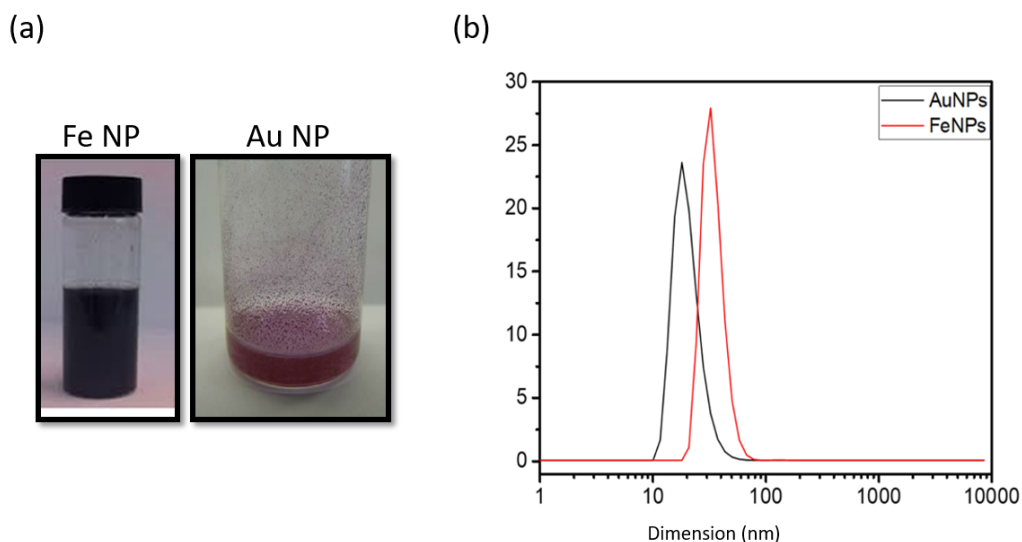


Figure 3.8. (a) Digital image of synthesized Fe and Au nanoparticles (b) DLS spectra showing the diameters of the synthesized Au and Fe nanoparticles

The mean diameters of the produced Au and Fe metal nanoparticles were estimated to be 46.15 nm and 46.30 nm, respectively, based on the dynamic light scattering (DLS) spectra in Figure 3.8. Because of the increased contact surface area caused by the small particle size, organic volatiles are detected more frequently. Metal nanoparticles are included into the conjugated polymer dispersion at a rate of 0.1% by mass to create nanoparticle added conjugated polymer dispersion.

3.1.4.4. Sensor Fabrication

The steps of the prepared sensor platform are shown in the Figure 3.9. In Figure 3.9 (a), the laser-cut PMMA substrate is schematically presented. Both ends are covered with copper tape to ensure electrical conductivity. Thus, both electrical conductivity was ensured and the conductive polymers coated with the electrospinning method were linearly oriented at both ends (Figure 3.9 (b)). After the conductive polymers are positioned on the PMMA substrate, MWCNT or PEDOT: PSS is dripped onto the surface and dried, the final state of the sensor platform is shown as a digital picture in Figure 3.9 (c).

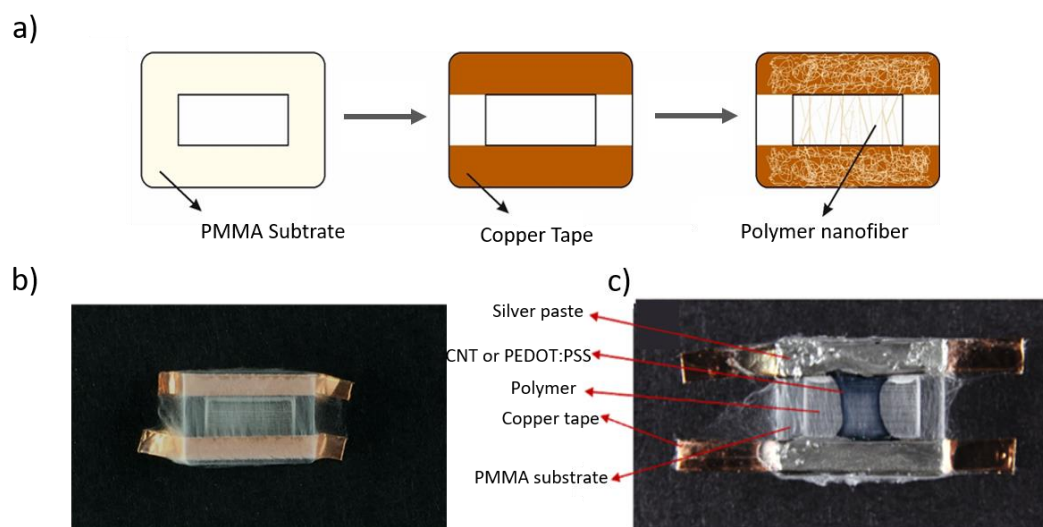


Figure 3.9. a) Schematic representation of sensor platform formation b) Digital image of polymer nanofiber formation on PMMA substrate c) Functionalized sensor platform with MWCNT or PEDOT:PSS

3.2. Characterization Techniques

After SLG, BLG, and MLG graphene is grown and transferred to a glass substrate, the presence and quality of the graphene film should be monitored. For the creation of high performance devices, it is crucial that the graphene remain continuous throughout the graphene transfer process without any contamination and surface cracks. In order to verify the presence and quality of graphene in our work, Scanning Electron Microscopy, Atomic Force Microscopy and Raman spectroscopy were all used. Electrical characterizations were also carried out for the sensor response.

3.2.1 Scanning Electron Microscopy

Particularly in the last few years, as the size of materials utilized in diverse applications has continued to decrease, scanning electron microscope (SEM) have developed into strong and adaptable tools for material characterization. In scanning electron microscopy, the sample is scanned using an electron beam in a raster pattern. Initially, electrons are generated at the upper part of the column through an electron source. These electrons are emitted when the thermal energy surpasses the work function of the source material. Subsequently, they are accelerated and drawn towards the

positively-charged anode. In this work, scanning electron microscopy (FEI QUANTA 250 FEG) used to determine surface morphology and characteristics of graphene after SiO₂ deposition and polymer nanofibers after electrospinning (Figure 3.10).



Figure 3.10. Scanning Electron Microscopy

3.2.2. Atomic Force Microscopy

Atomic force microscopy (AFM) is widely regarded as the most flexible and potent microscopy technique for investigating nanoscale samples. Its versatility stems from the fact that an atomic force microscope can not only capture three-dimensional topographic images but also offer diverse surface measurements tailored to the requirements of scientists and engineers. Moreover, AFM demonstrates its power by delivering images with atomic resolution and providing height information at the angstrom scale, all while requiring minimal sample preparation. AFM's working principle relies on the detection of the forces between the probe tip and the sample surface, enabling high-resolution imaging and characterization of nanoscale features and properties. In addition to topographic imaging, AFM can be used in various modes to measure other surface properties. For example, it can perform measurements of surface roughness, mechanical properties, conductivity, magnetic forces, and chemical interactions by modifying the experimental setup or using specialized probe tips. In this work, we used AFM to examine the surface morphologies of the sensor samples we prepared and also to

measure the changes in the surface conductivity of the conductive polymers we coated on the sensor surface atomically using the conductive AFM (c-AFM). Similar to traditional AFM, c-AFM uses a sharp probe tip attached to a cantilever and the probe tip is modified to have an electrically conductive coating.

In this study, we used the Nanosurf Core AFM device (Figure 3.11) in our laboratory for our measurements. For the surface topography, we used a contact mode type beam shaped cantilever with a force constant of 0.2 N/m. For conductivity measurements, we used a Pt coated Multi75E-G cantilever with a force constant of 3 N/m, a length of 225 μm , a width of 28 μm , and a diameter of 10 μm . While taking conductivity measurements, we made sure that there was a contact between the sample and the cantilever and applied a potential difference of 1V.



Figure 3.11. Digital image of atomic force microscopy in our laboratory

3.2.3. Raman Spectroscopy

Raman spectroscopy is an important characterization technique which is used to determine the number and orientation of layers, the quality and types of edge, such as electric and magnetic fields, strain, doping, disorder and functional groups. The layer number and quality of graphene was identified in this study through the use of Raman spectroscopy. All measurements were conducted using a Raman spectrometer, specifically the Monovista from Princeton Instruments (Figure 3.12). The Raman signals were captured within the spectral range of 1000 – 3100 cm^{-1} , using an Ar^+ ion laser with a 488 nm (2.54 eV) excitation, which allowed for the observation of all D, G, and G' peaks of graphene due to the 600 grooves/mm grating. Each obtained spectrum was analyzed through the TriVista software.

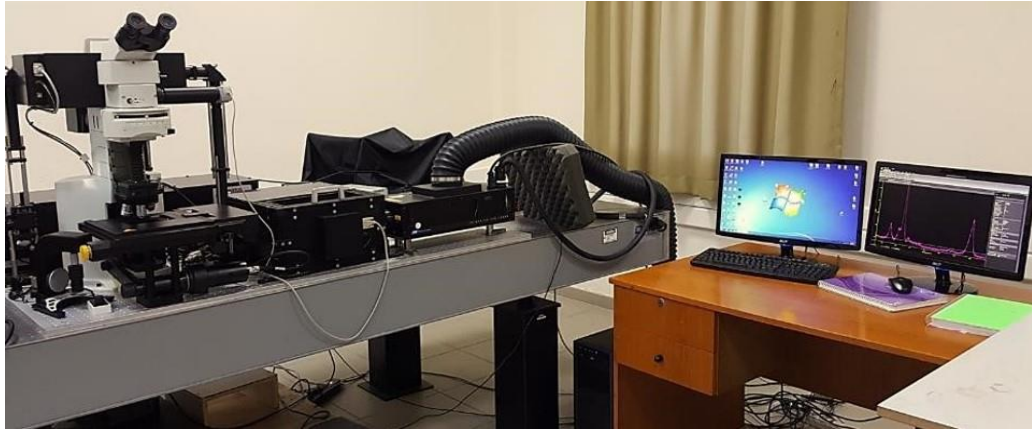


Figure 3.12. Raman spectroscopy measurement system

Three major peaks at the designated wavenumbers can be found in the Raman spectrum of graphene. Raman spectra of graphene have peaks at 1350 cm^{-1} for the D peak, 1581 cm^{-1} for the G peak, and 2700 cm^{-1} for the 2D peak⁹⁹. The G' and D bands, which are significant in revealing information about the electrical and geometrical structure through the double resonance process, as well as the G-band, which is common to all sp^2 carbon forms¹⁰⁰. The G peak in graphene stands for in-plane vibrations of sp^2 bonded C-C pairs. It represents the strong graphitic quality of the material. On the other hand, the 2D peak provides information about the number of graphene layers present. A strong G peak and a weak D peak suggest high-quality graphitic structure. Furthermore, the intensity ratio between the 2D and G peaks (I_{2D}/I_G) is an important factor in determining the layer nature of graphene. When this ratio is greater than one ($I_{2D}/I_G > 1$), it confirms that the graphene layer is a monolayer. In the case where the I_{2D}/I_G ratio equals one ($I_{2D}/I_G = 1$), it indicates the presence of bilayers of graphene. On the other hand, if the I_{2D}/I_G ratio is less than one and the values are akin to each other, it suggests that the number of graphene layer consists of multi layers¹⁰¹. The Raman spectra of single layer, bilayer and few layer graphene was shown in Figure 3.13.

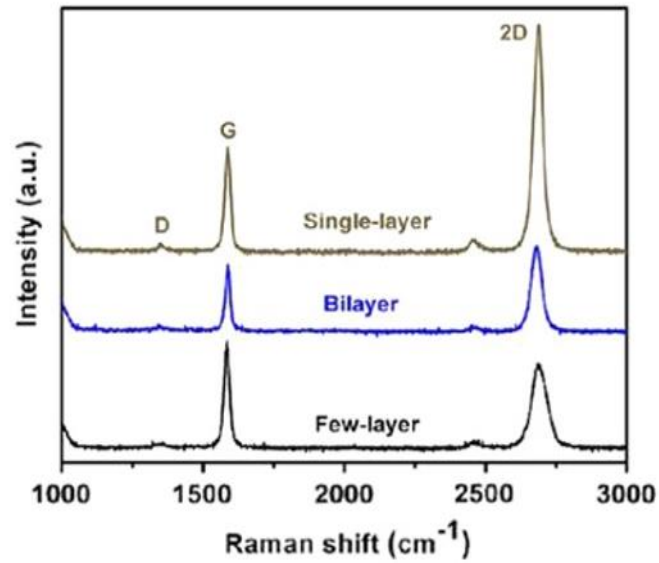


Figure 3.13. Raman spectroscopy measurements of single layer, bilayer and few layer graphene¹⁰².

3.2.4. Electrical Characterizations

The electronic characterizations of the fabricated all sensors were performed in a flow-controlled gas chamber connected to a Keithley 2400 general purpose sourcemeter and HP4145B parameter analyzer (Figure 3.14).

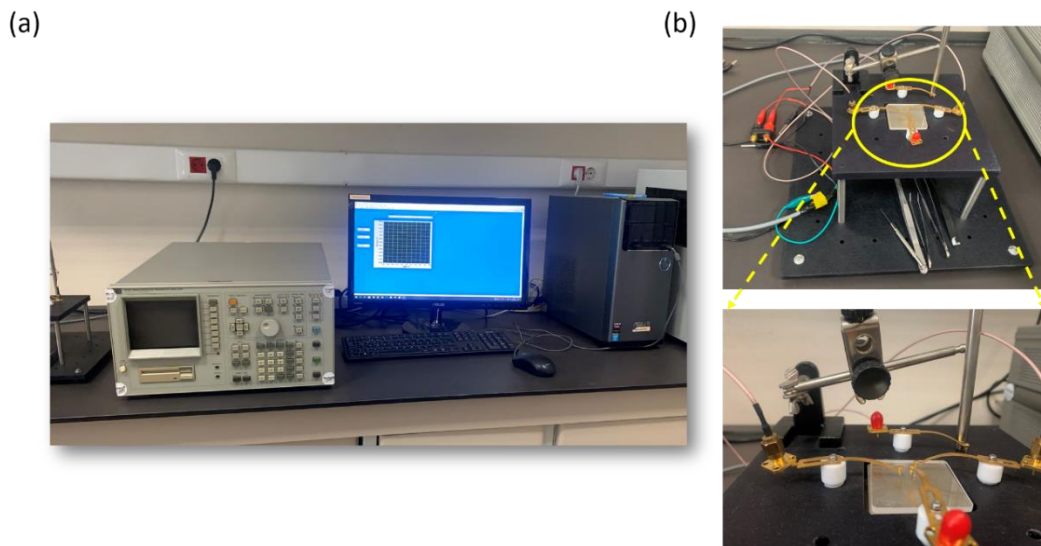


Figure 3.14. (a) HP4145B parameter analyzer that we use in electrical measurements (b) Two probe sample holder station

The electrical responses of gas sensors formed with nanofibers produced from various polymers functionalized with CNT and PEDOT to various volatile organic compound gases such as acetone and ethanol were investigated. The gas cell used in gas sensor measurements, VOC station and mass flow controller are shown in the Figure 3.15. The gas flow is given to the system using the mass flow control component. The prepared sensors are placed in the gold needle tipped sample holder inside the gas cell and the gas cell is sealed so that there is no gas inlet or outlet. With the mass flow controllers, the amount of gas that will go to the gas cell is adjusted in ppm and sent to the gas cell. After each measurement, N_2 gas is sent to the gas cell and the gases adsorbed on the surface are desorbed. Electrical responses are recorded using the interface.



Figure 3.15. VOC detection system in our laboratory

CHAPTER 4

RESULTS AND DISCUSSION

4.1. Lipid Bilayer on Wrinkled-interfaced Graphene Field Effect Transistor

In this chapter presents a detailed description of a sensor interface based on lipid bilayers, integrated with graphene field effect transistors (GFETs) encapsulated in a SiO₂ layer. The SiO₂ layer serves as a compatible surface for lipid bilayer formation. Two different surface morphologies were achieved: a wrinkled morphology through thermal evaporation (TE) and a flat morphology through pulsed electron deposition (PED). The sensing performance of the wrinkled and flat interfaced-GFETs was thoroughly investigated, revealing that the pH sensitivity of the wrinkled interfaced-GFETs was ten times greater than that of the flat ones. This improved sensitivity can be attributed to the thinning of the oxide layer caused by the formation of wrinkles, which facilitates electrostatic gating on the graphene. The ultra-thin yet stable oxide layer located inside wrinkles provide protection of graphene while not mitigating electrostatic gating and doping. The formation bioelectronic interface made of lipid bilayer has been characterized, upon bilayer formation the I-V characteristics of wrinkled and flat interfaced-GFET devices monitored. The wrinkled interfaced-GFET platforms have exhibited one order of magnitude higher sensitivity by lipid bilayer formation as compared to flat interfaced devices.

Experimental processes were shown in Figure 4.1 step by step. In Figure 4.1 (a), 4 mm x 10 mm rectangular SiC substrate was shown prior growing process. After epitaxial growth on SiC substrate, due to the tantalum contacts there was a 2 -cm-rectangular region which was not covered by graphene as seen in Figure 4.1 (b). To achieve the effective area of graphene and prevent electrical short, we decided to etch graphene as the size of 6 mm x 2 mm area using Ni mask. To do this etching, first of all we designed a 6 mm x 2 mm mask made of stainless steel. The mask is placed on our graphene samples and 40 nm Ni was deposited through the sample with a thermal evaporation system under high vacuum. After the deposition, we removed the mask from

the sample and Ni was etched with FeCl_3 (30 %). The uniform 6 mm x 10 mm rectangular graphene area was obtained Figure 4.1 (c). After the etching process, Cr/Au electrodes was deposited using masks with a thermal evaporation system. To achieve the gold adhering to the surface, 5 nm Cr was deposited first, then 80 nm Au was evaporated to the sample surface. Therefore, electrodes were contacted to the graphene surface with 0.5 cm^2 area. Cr/Au contacts was deposited onto epitaxially growth graphene sensor surface by thermal electrode deposition. 3 mm x 10 mm stainless stain mask was designed, and 4 nm chromium and 80 nm gold were evaporated above the glass substrates with thermal evaporation system (Figure 4.1 (d)). For wrinkled structure, SiO_2 was deposited on a 6.5 cm x 4 mm area over the epitaxial graphene as shown in Figure 4.1 (e). Therefore, conductive wires soldered to gold contacts with indium wire and contacts were achieved in this way successfully (Figure 4.1 (f)).

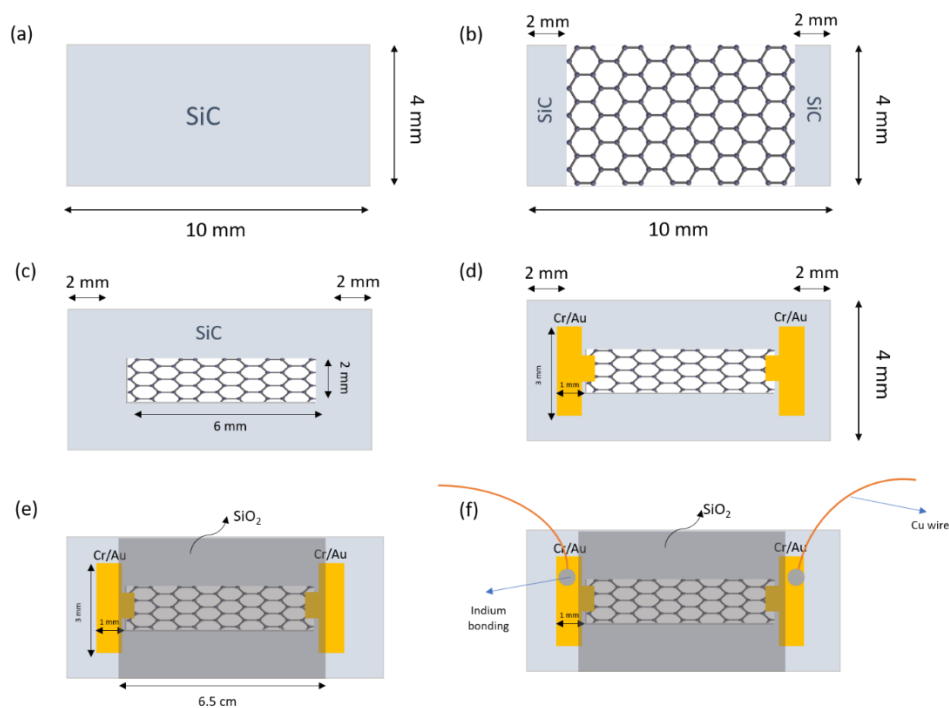


Figure 4.1. Designed device fabrication step by step.

Figure 4.2 provides a visual representation of the diverse surface morphologies resulting from the deposition of a SiO_2 thin film on a SiC substrate with epitaxially grown graphene, using two techniques: TE and PED. The TE technique generated a wrinkle pattern that showcased the hexagonal symmetry of the underlying epitaxial graphene template, while PED produced a flat SiO_2 layer. The formation of wrinkles occurred

during the cooling process, as the temperature decreased from the deposition temperature to room temperature. This surface dynamics suggests that the wrinkling phenomenon can be attributed to the abrupt relaxation of the TE-grown SiO₂ thin film on the epitaxial graphene layer, resulting from compressive strain. The frequent observation of a mesh-like network of ridges in monolayer graphene grown at high temperatures indicates that the formation of wrinkles is associated with the thermal-induced buckling of the monolayer graphene, which occurs due to its negative thermal expansion coefficient ($\alpha_{\text{graphene}} = -8 \times 10^{-6} \text{ K}^{-1}$) in epitaxial graphene¹⁰³. Considering the TEC and Young's modulus values of SiO₂ ($\alpha_{\text{SiO}_2} = 0.5 \times 10^{-6} \text{ K}^{-1}$, $E_{\text{SiO}_2} \approx 70 \text{ GPa}$)^{104,105} and of single crystal SiC ($\alpha_{\text{SiC}} = 4.1 \times 10^{-6} \text{ K}^{-1}$, $E_{\text{SiC}} \approx 700 \text{ GPa}$)^{106,107}, for the given deposition parameters, the magnitude of strain experienced by the SiO₂ film on a bare SiC surface is expected to be significantly greater than that of the SiO₂ layer on epitaxial graphene. However, the thickness of SiO₂ coated with PED technique is much thicker (10 times more) compared to that coated with TE, the wrinkling structure is not observed here and acts as a thin film on the epitaxial graphene surface. Thus, it gives an opportunity to show how two different morphologies (wrinkle and flat) on the same material (SiO₂) changes the sensor behavior in electrically.

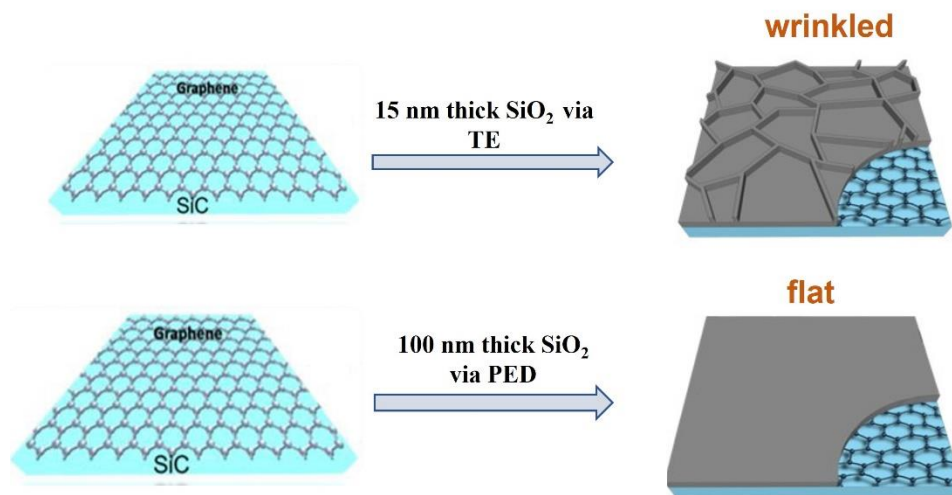


Figure 4.2. Schematic representation of wrinkled and flat surface structure after 15 nm and 100 nm thick SiO₂ deposition via TE and PED, respectively.

A 1 L supply of 1X PBS was used to make a variety of buffers with varying pH values for pH measurements. Sodium hydroxide (NaOH) or hydrochloric acid (HCl) can be used to change pH values from 5 to 9. Furthermore, lipid vesicles are prepared by

French Pressure Cell (extrusion) method ¹⁰⁸, for his purpose a stock solution of phosphatidylcholine (PC) is prepared. 25 mg of PC was dissolved in 250 μ l chloroform. Before extrusion a working solution is prepared by using 50 μ l stock solution first step of working solution preparation was removal of chloroform via N₂ stream. Then dried stock solution is dissolved in 5ml 1x PBS solution and frozen. Working solution was defrosted by ultrasonic bath and the freeze-thaw process was carried out for eight cycles. Afterwards 1 ml of working solution was used for extrusion process. For the procedure, a membrane filter with 200 nm pore size was used, and each sample underwent 21 cycles of extrusion. (Figure 4.3). The prepared pH and lipid vesicles were dripped onto the sensor surface and made ready for electrical measurement ^{109,110}.

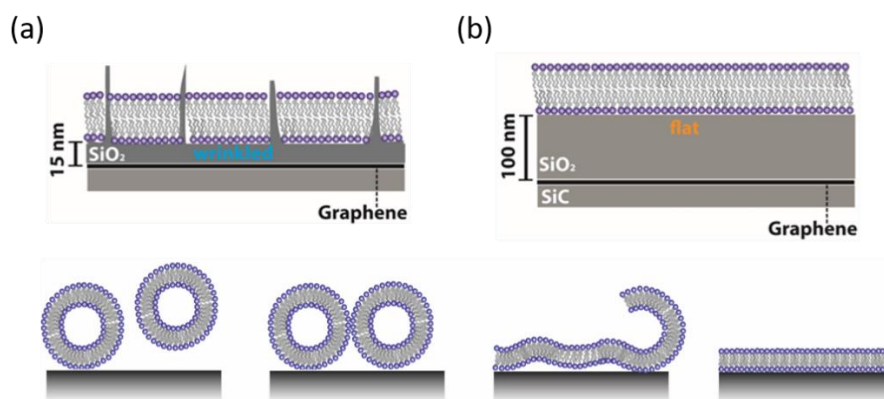


Figure 4.3. Schematic figure of lipid bilayer formation on wrinkled a) and flat b) SiO₂ surface

The surface morphology of both wrinkled and flat sensor surface was characterized with scanning electron microscopy (SEM) as seen in Figure 4.4. These images were taken under 3 kV voltage and 1000X magnification. High magnification SEM analysis revealed that the wrinkles separate into two distinctive parallel threads. Three of these stranded wrinkles fold and intersect strongly, and when they combine, they form distinct nodes. The wrinkle pattern's hexagonal lattice properties were suggested by the angle of 118° between the two wrinkles. According to SEM images, the wrinkle network primarily consists of wide and narrow branches.

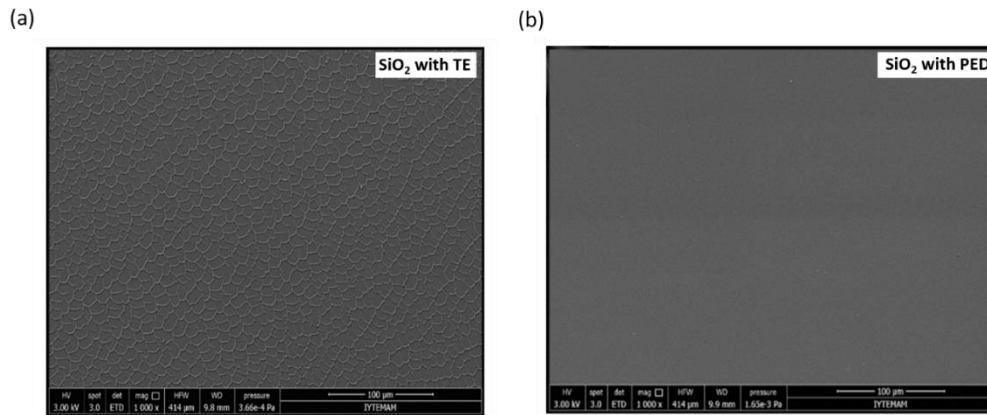


Figure 4.4. High magnification scanning electron microscopy images of (a) wrinkled and (b) flat oxide surfaces

The AFM operating in tapping mode was employed to assess the topography measurements of the SiO₂ wrinkle structures on epitaxial graphene. A Tap-150-g centilever, possessing a force constant of 5 N/m, was utilized for this purpose. The analysis revealed that the wrinkle network exhibited wrinkle sizes ranging from 35 to 40 μm. Furthermore, measurements along various surface orientations determined an average distance of approximately 13 μm between adjacent wrinkles. Based on the morphology and height profiles observed in the AFM topography image (Figure 4.5 (a)), linear protrusions were identified and categorized as primary and secondary wrinkles. To differentiate between these two types of wrinkles, it was noted that primary wrinkles follow a zigzag path without intersecting to form wrinkle nodes (Figure 4.5 (b)). In contrast, secondary wrinkles exhibit a maximum height (0.28 μm) that is generally lower compared to primary wrinkles (0.4 μm), as depicted in Figure 4.5 (c).

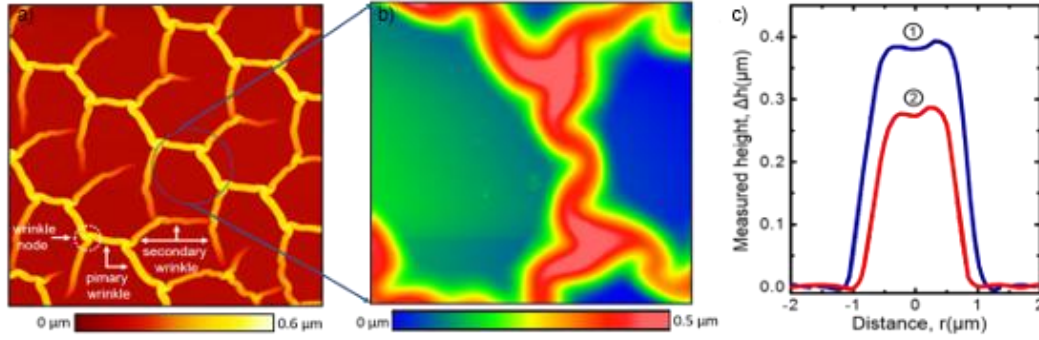


Figure 4.5. (a) AFM topography image of TE deposited SiO₂ wrinkle network on epitaxial graphene (50 x 50 μm² area) (b) Zoomed in AFM topography image of localized height protrusions (10 x 10 μm² area) (c) The cross-sectional line profiles of primary and secondary wrinkles were examined, with the primary wrinkles denoted as 1 and the secondary wrinkles as 2.

The electrical response of GFET sensor to the pH buffer and lipid vesicles was done by Hewlett –Packard model 4145B Semiconductor Parameter Analyzer. All I-V measurements were performed under 3V bias. Figure 4.6 illustrates the variation in conductivity of both flat and wrinkled interfaced-GFET in response to different pH values. During the experiment, the pH values were altered within a range of 5 to 9. The pH measurements indicated that as the density of H⁺ ions decreased from 10⁻⁵ to 10⁻⁶, a noticeable difference in maximum current was observed between the wrinkled and flat surfaces. Under a 3V bias, the maximum current experienced a notable increase to 199.5 μA on the wrinkled surface, as depicted in Figure 4.6 (b). In contrast, the current on the flat surface remained relatively low at only 2.59 μA, as shown in Figure 4.6 (a). The sensing mechanism employed for detecting H⁺ ions on the SiO₂ surface relies on the electrostatic gating effects, which can be described by the Gouy-Chapman-Stern-Graham model¹¹. In the Gouy-Chapman-Stern-Graham model

$$n = n_0 \exp(-ze\Psi/kT) \quad 4.1$$

where, n₀ is the Bulk concentration, z is the charge on the ion, e is the charge on proton, k is the Boltzmann constant and T is the temperature. The Gouy-Chapman-Stern-Graham model describes the distribution of adsorbed ions on a charged particle surface that interacts with an aqueous electrolyte solution. This model takes into account the electrostatic effects that arise due to the presence of ions of a particular charge attached to the surface, as well as an equal number of ions of the opposite charge in the surrounding solution. It is important to note that the counter ions are not firmly attached to the surface,

and tend to diffuse into the liquid phase until their departure creates a counter potential that limits their movement. The kinetic energy of the counter ions will, in part, affect the thickness of the resulting diffuse double layer. The diffuse double layer was studied by Gouy and Chapman, who independently developed theories to describe it. According to these theories, the concentration of counter ions near a charged surface changes in accordance with the Boltzmann distribution. As the concentration and valence increase, the thickness of the double layer decreases. Additionally, the concentration of oppositely charged ions decreases as distance from the surface increases. In the case of the SiO₂ dielectric surface, the presence of hydroxyl species (-OH) and H⁺ ions in the solution can lead to alterations in the surface charge density. When compared to the flat surface under a 5V bias, the conductivity of the wrinkled surface is approximately 100 times higher, reaching 1027 A at pH 9. The inset plots in Figure 4.6 display the current versus pH characteristics for both flat and wrinkled surface GFETs, with -3V and 3V biases applied, respectively. These graphs reveal that wrinkled surface GFETs exhibit 80 times greater sensitivity to changes in pH compared to flat GFETs.

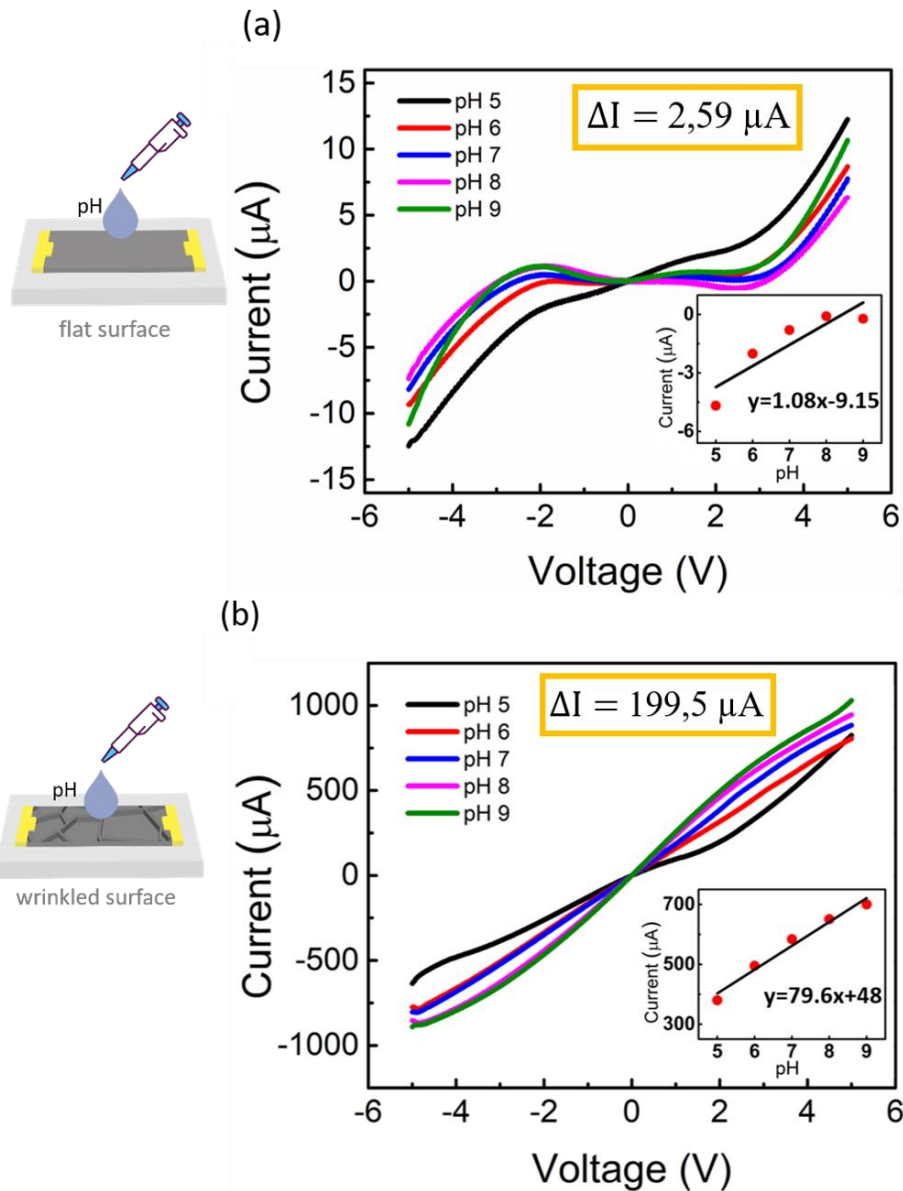


Figure 4.6. I-V characteristics depicting the pH dependence are presented for both (a) flat interfaced-GFET and (b) wrinkle interfaced-GFET. Insets in the figure illustrate the linear fitting of current versus pH values for the flat interfaced-GFET and the wrinkle interfaced-GFET, respectively.

In Figure 4.7, the conductivity variation over time is depicted for both exposure to a lipid solution (indicated by the black line) and a blank buffer (indicated by the red line). The accompanying I-V measurements are shown for biases ranging from -3V to 3V. The graph reveals four distinct steps observed during the process, starting from the addition of lipid vesicles and leading to the formation of a bilayer. The four steps observed in the process are as follows: vesicle adsorption (1), surface saturation by vesicles (2), vesicle rupture (3), and bilayer formation (4). Step 1 involved a sudden increase in current

within 350 seconds for both wrinkled and flat surfaces. For the wrinkled interfaced-GFET (Figure 4.7 (a)), the current rose from 550 μA to 750 μA ($\Delta i = 250 \mu\text{A}$) upon vesicle injection. Similarly, for the flat interfaced-GFET (Figure 4.7 (b)), the current changed from 110 μA to 127.5 μA within 250 seconds. These findings align with previous studies that have reported current changes in the range of 10 to 100 μA when vesicles are exposed to graphene surfaces¹¹². The adsorption of lipid vesicles alters the Fermi energy level of graphene, leading to a reduction in resistance. During step 2, the current change ceased and reached an intermediate baseline for both wrinkled and flat interfaced-GFETs. This behavior indicates that the SiO₂ surfaces of both devices became saturated with vesicles, reaching a state of equilibrium¹¹³. During step 3, a significant current increase was observed in the wrinkled interfaced-GFET, rising from 750 μA to 875 μA ($\Delta i = 125 \mu\text{A}$). In contrast, the flat interfaced-GFET exhibited only a small increase of approximately 4 μA . This abrupt current change can be attributed to vesicle rupture, which induces a reorganization of surface charge and subsequently leads to electrostatic gating effects. The response to vesicle rupture was found to differ significantly between the wrinkled and flat interfaced-GFETs. The disparity in performance between the two GFETs can be attributed to the thickness of the oxide layer in the devices, which directly influences the extent of electrostatic gating. In step 4, the current response stabilized for both types of GFETs, indicating the presence of a stable lipid bilayer formed on the surface. In summary, during the process of bilayer formation, a current change of 19 μA was observed on the flat surface, whereas a significantly larger change of 390 μA was observed on the wrinkled surface. This substantial difference indicates that the binding of lipids to the wrinkled surface is approximately 19 times more sensitive compared to the flat surface, emphasizing the enhanced sensitivity of the wrinkled surface to lipid interactions.

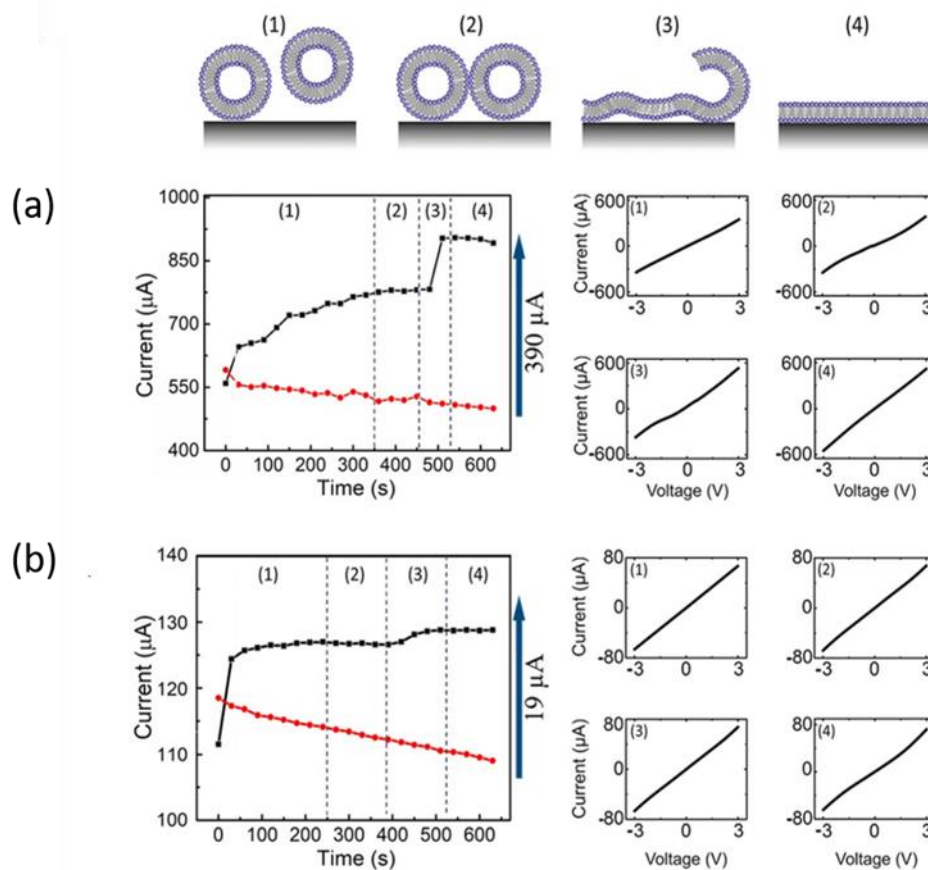


Figure 4.7. The time-dependent current measurements of lipid vesicle adsorption characteristics are illustrated for (a) wrinkle interfaced-GFET surface and (b) flat interfaced-GFET surface.

The data presented in Figure 4.8 illustrates the current change histogram of the wrinkled interfaced-GFET sample after the removal of lipid vesicles from the surface using a sodium dodecyl sulfate (SDS) solution, followed by lipid adsorption on the cleaned surface. As is known in literature detergents (like SDS) solubilize lipid bilayers from the surface.¹¹⁴ The findings indicate that the lipids return to the initial current value (approximately 50 μA) after removal from the surface and an increase in the current value (approximately 200 μA) is observed upon attachment to the surface. The current change histogram of the wrinkled interfaced-GFET sample is shown in Figure 4.8 following the removal of lipid vesicles from the surface with SDS solution and subsequent lipid adsorption on the freshly cleaned surfaces. When the lipids were attached to the surface, the current value increased, and when they were removed, the current value went back to its original value. In order to test for repeatability, lipids were first extracted from the surface using SDS solution and then reabsorbed.

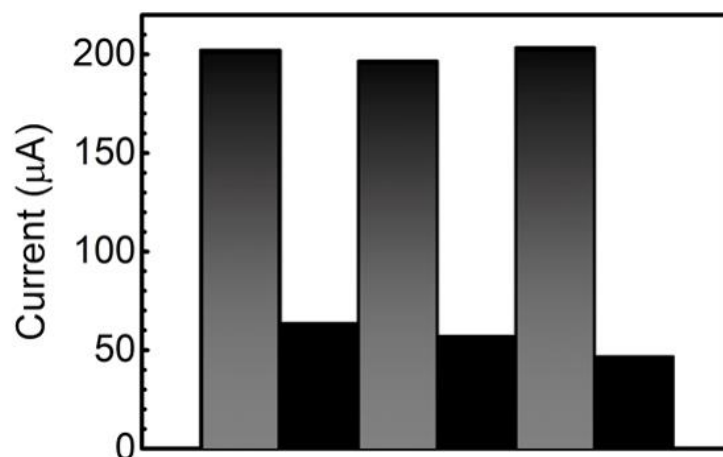


Figure 4.8. A histogram showing the repeatability of absorbing and dissipating lipid vesicles from SiO₂ surface. Black columns show the current change of lipid vesicles adsorbing on the SiO₂ surface. Gray columns depict the current change of lipid vesicle dissipating via SDS solution from SiO₂ surface.

4.2. Multi-layered Graphene Based Gas Sensor Platform for Volatile Organic Compounds Discrimination via Differential Intercalation

Selective and sensitive volatile organic compound (VOC) detection is essential for industrial applications, disease diagnostics, and environmental monitoring. Primary alcohol intoxication has received a lot of research attention since it negatively affects the nervous systems, leading to blindness and comas and even being fatal at high exposure levels. However, because of the similarities in terms of molecular structure, it is very difficult to detect primary alcohols specifically. Here, we have made an effort to look into the diverse single, bi, and multi-layer graphene morphologies' methanol (MeOH)-ethanol (EtOH) discriminative capabilities. In addition to this, our study aimed to explore the ability to differentiate structurally similar VOCs by utilizing graphene in different morphologies.

Before the growth procedure, all substrates (SiC and glass) were cleaned with RCA cleaning procedure. This part was very crucial for samples to get rid of organic residues from the substrate surface. For RCA cleaning procedure, deionized water, ammonium hydroxide (29%) and hydrogen peroxide (30%) solution by volume 5:1:1 by volume are added into the beaker in this order. The mixture is taken on the heater fixed at 80 °C. Air bubbles are observed in the mixture with increasing temperature. Heating is continued until the air bubbles are greatly reduced or gone (Approximately 20 minutes).

The mixture is taken over the heater and the substrates are taken into a separate beaker and washed several times with plenty of distilled water. In the second stage, the wafer is kept in a solution of deionized water, hydrochloric acid (37%) and hydrogen peroxide (30%) at a ratio of 6:1:1 by volume, at 80 degrees for 10 minutes ¹¹⁵. (At this stage, alkali and transition metals are removed from the surface). Substrates are taken into a separate beaker and washed several times with plenty of distilled water. As the final step, substrates are air dried with inert N₂ gas so that they are not contaminated again. After cleaning steps, as mentioned in the previous section gold electrodes (8 nm Cr /80 nm Au) were coated both SiC and glass substrates before growth procedure via thermal evaporation for I-V measurements. After, for SLG, BLG and MLG growth process was performed. While SLG was grown on SiC substrate, BLG was grown and transferred on copper foil but for MLG, the GF gold electrode is fixed on the coated glass surface with double-sided conductive carbon tape. One of the sensors prepared for SLG, BLG and MLG is shown in Figure 4.9.

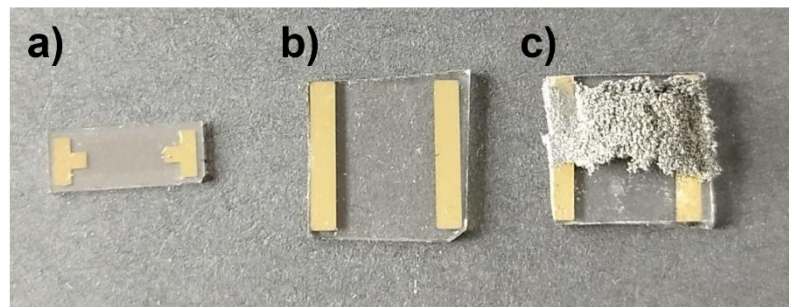


Figure 4.9. a) SLG b) BLG and c) MLG devices

The Raman measurements of SLG (black line), BLG (red line) and MLG (blue line) devices was performed in Figure 4.10. I_{2D}/I_G ratios of 1.8, 1 and 0.5 confirms the SLG, BLG and MLG, respectively ^{116,117}. The presence of an asymmetric 2D shape in the Raman peak at approximately 2700 cm^{-1} confirms that the MLG consists of more than 10 layers of graphene¹⁰¹.

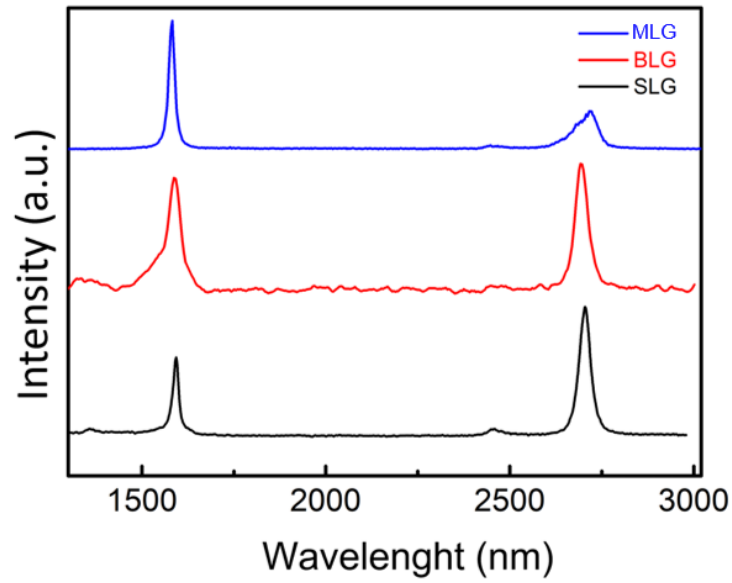


Figure 4.10. Raman spectra of SLG (black), BLG (red) and MLG (blue)

High resolution SEM images of SLG, BLG and MLG were examined to examine the surface morphology. For this, SEM images of the prepared sensor surfaces at different magnifications were analyzed. Figure 4.11 demonstrates that SLG exhibits a uniform surface, indicating a homogeneous epitaxial growth on the silicon substrate. Although the growth process is under ultra-high vacuum, it is possible to observe it at some points on the surface since the sensor measurements are made under room conditions. Therefore, all sensors are kept in a desiccator immediately after growth, rather than at room conditions.

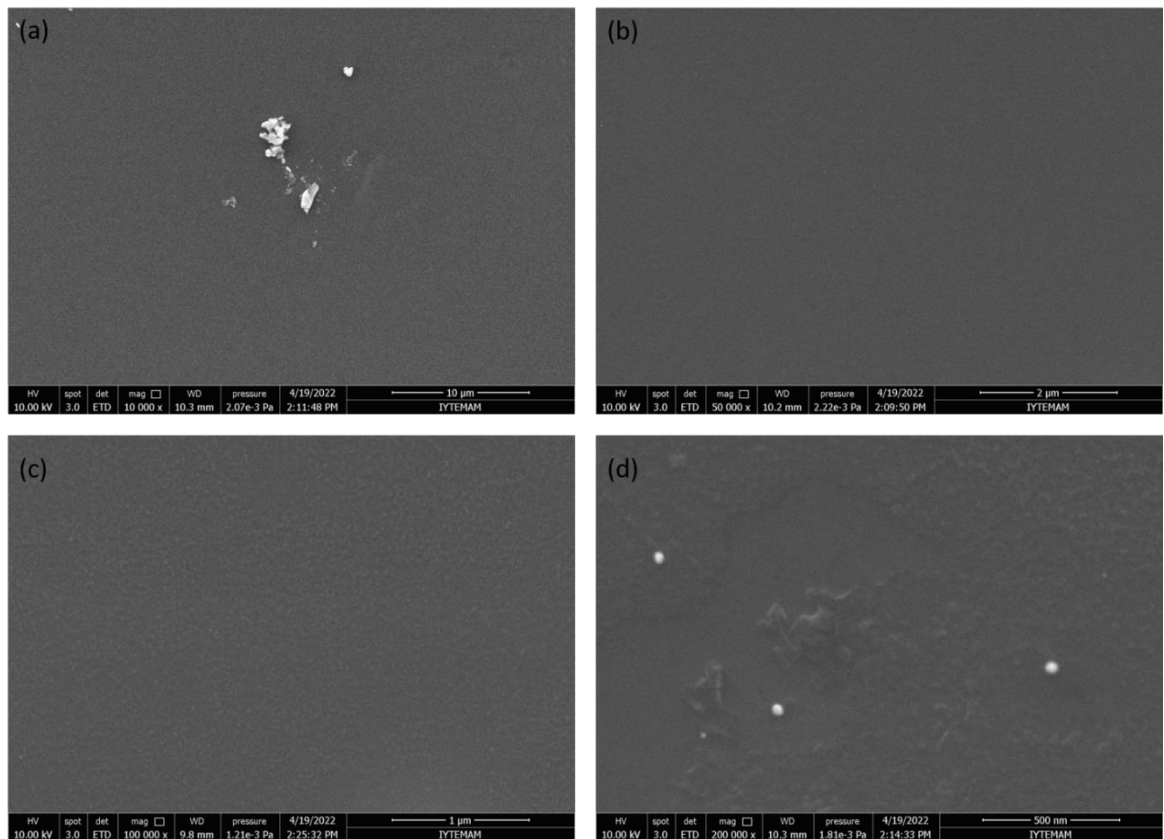


Figure 4.11. SEM images of SLG grown on SiC substrate with (a) 10.000 x (b) 50.000 x (c) 100.000 x and (d) 200.000 x magnifications

In contrast to SLG, the surface of BLG displays features with varying contrasts, including darker and lighter regions. These variations can be attributed to the formation of the second layer of graphene on top of the SLG, following the growth protocol utilized in the study. In Figure 4.12 the places where the contrast is high represent two layers, and the places where the contrast is low represent a single layer.

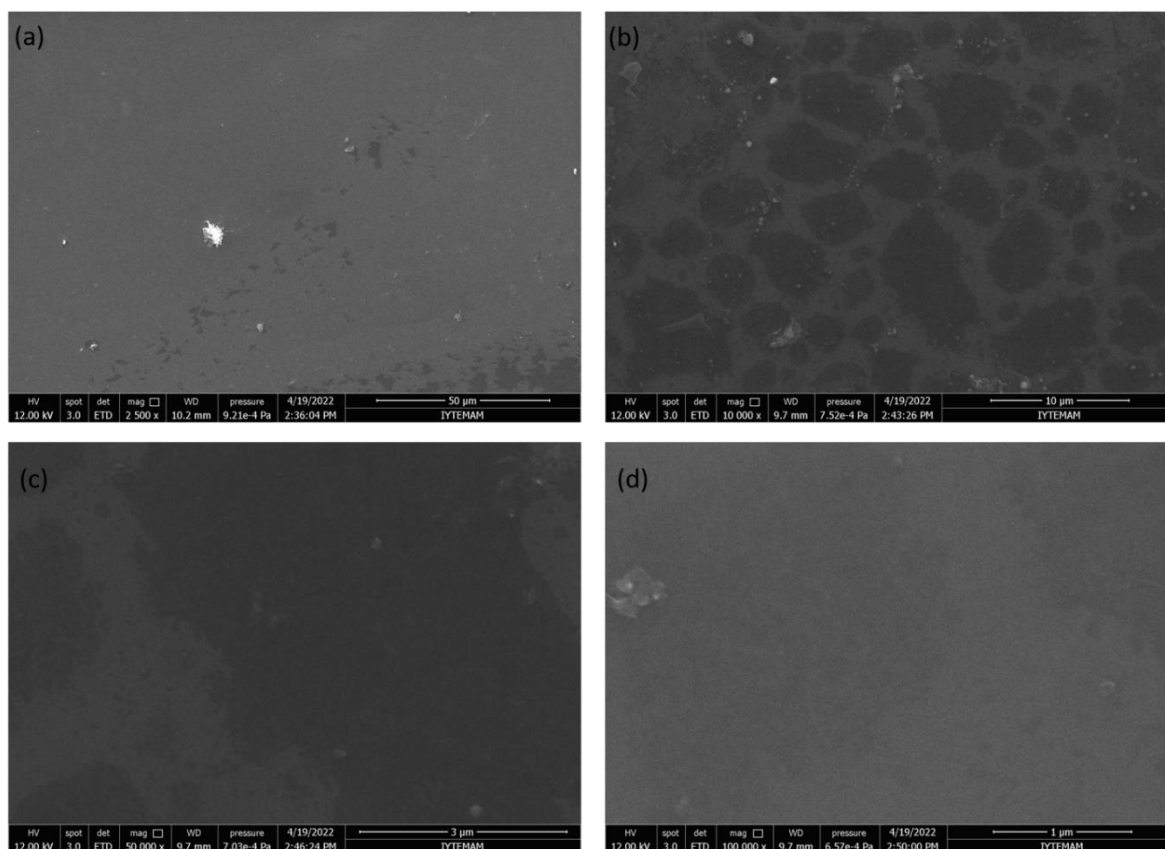


Figure 4.12. SEM images of BLG grown on SiC substrate with (a) 2.500 x (b) 50.000 x (c) 100.000 x and (d) 200.000 x magnifications

Upon synthesis, the MLG exhibits an interconnected morphology with an average pore size of 400 μm . This pore size is comparable to the pore size of the Ni template used in the MLG synthesis, indicating that the MLG conforms to the morphology of the Ni template. In comparison to SLG and BLG, the MLG possesses a significantly larger surface area due to its porous nature. This increased surface area, multiplied by several orders of magnitude, has the potential to enhance the binding of VOCs to the MLG material, thereby amplifying the detection sensitivity. In the cross-sectional SEM image of MLG presented in Figure 4.13 (a) inset, struts with walls having thicknesses in the range of a few nanometers can be observed. The darker and lighter areas in the transmission electron microscopy (TEM) image of MLG, as shown in Figure 4.13 (b), correspond to graphene with many and few layers, respectively. The Selected Area Electron Diffraction (SAED) pattern of graphene exhibits a high degree of crystallinity in MLG. Considering that the diameters of MeOH and EtOH molecules are 3.0 and 4.4 \AA , respectively, layered graphene materials with an interlayer distance of 3.35 \AA , such as MLG, may facilitate selective intercalation, as depicted in Figure 4.13 (c).

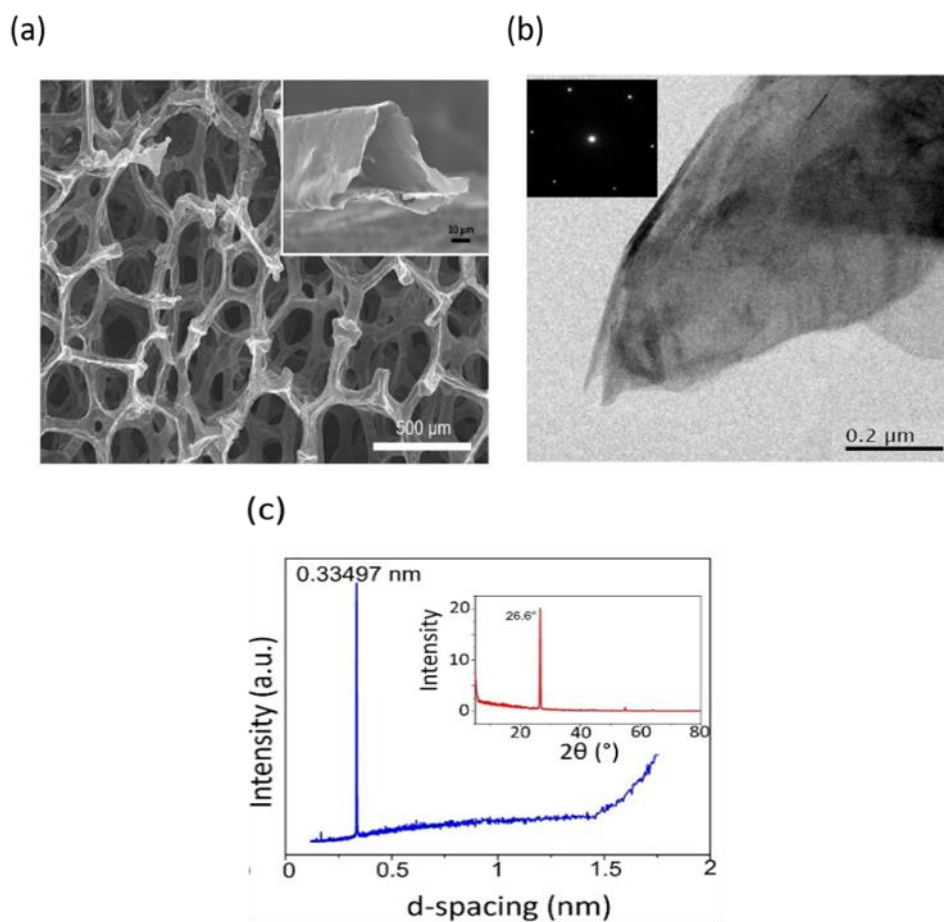


Figure 4.13. (a) SEM images of MLG (b) TEM image of MLG framework and inset related SAED pattern (c) d-spacing between graphene layers is assessed using the MLG XRD spectrum. (inset).

The surface topography, homogeneity and conductivity of the SLG and BLG were assessed through AFM and conductive AFM analysis following chemiresistor fabrication. However, it is not suitable for AFM measurement due to the 3D and porous structure of MLG. Figure 4.14 (a) and (b) depicts the surface topography and conductivity measurements of SLG, respectively. The analysis showed that both SLG surfaces were smooth, with height variations ranging from 1-3 nm. This indicates that the synthesis of SLG was epitaxial without significant defects. Furthermore, the cross-sectional analysis indicated that SLG exhibited a surface cross-section of approximately 1 nm, with a roughness of approximately $0.5 \text{ nm}/\mu\text{m}^2$. These findings suggest a high level of surface homogeneity across the chemiresistor. Conductive mapping of the device showed that the current density ranged between 2-10 nA over an area of $50 \times 50 \mu\text{m}^2$ for SLG. The histogram analysis revealed that the surfaces of SLG were highly homogeneous, displaying a narrow range of current density distribution centered around $2 \text{ nA}/\mu\text{m}^2$.

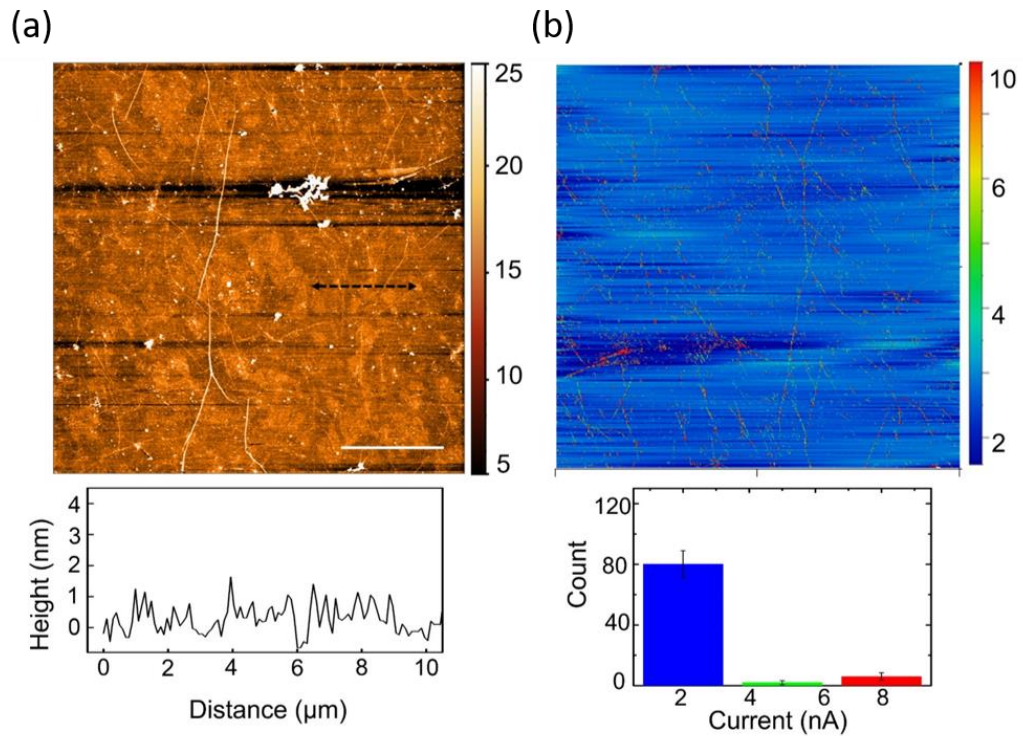


Figure 4.14. (a) AFM topography image measuring $50 \times 50 \mu\text{m}$ and its corresponding cross-sectional profile (b) Conductive AFM current mapping performed on SLG, and the resulting current distribution histogram

In addition to this, the surface topography and surface conductivity of BLG was also measured with AFM and c-AFM. Figure 4.15 depicts the surface topography with surface undulation and conductivity map corresponding area. In Figure 4.15 (a), BLG indicates 2-6 nm variations in height from the surface topography AFM measurement. The surface roughness of $50 \times 50 \mu\text{m}$ area BLG was analyzed as $0.5 \text{ nm}/\mu\text{m}^2$. This roughness value is almost 2 times less than SLG. In addition to this, conductive mapping depicts that current density changes between the 70-150 nA range (Figure 4.15 (b)).

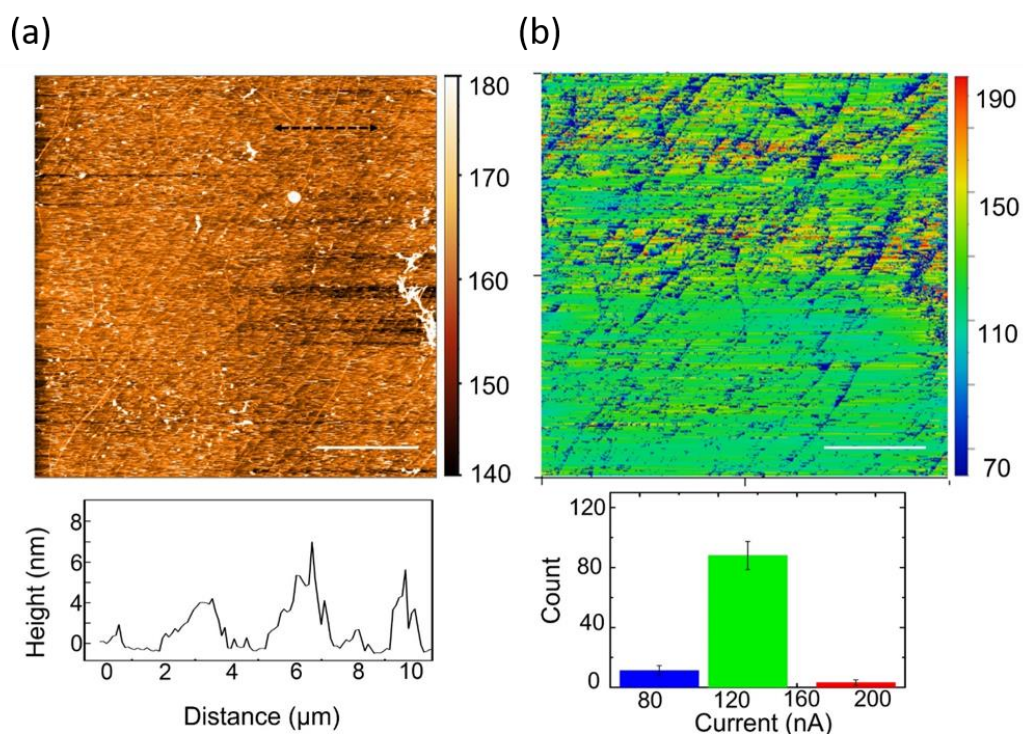


Figure 4.15. (a) AFM topography image measuring 50 x 50 μm and its corresponding cross-sectional profile (b) Conductive AFM current mapping performed on BLG, and the resulting current distribution histogram

In Figure 4.16, Figure 4.17 and Figure 4.18 ; the adsorption of MeOH and EtOH on the surfaces of SLG, Bilayer Graphene BLG, and MLG leads to varying chemiresistor responses. These responses can be attributed to a synergistic effect arising from differences in the molecular size of MeOH and EtOH, the adsorption capacity, and the clustering behavior of MeOH and EtOH on the surface of the graphene layers. Before conducting the VOC testing, the stability of the three devices was confirmed through N₂ purging as shown in these figures as gray line. First, the SLG device was exposed to ethanol and methanol gases with 0.2 ppm to 50 ppm gas concentrations and time dependent resistivity was measured at 1V bias under room temperature conditions (Figure 4.16). Before the gas exposure, base resistivity values (R_0) was recorded as 50 s. While the base resistivity is 0,28 Ω for ethanol exposure to SLG device, 0.23 Ω for methanol exposure. When different amounts of MeOH and EtOH were introduced, there was not a noticeable difference in the SLG chemiresistor response. Following and before to MeOH / EtOH exposure both VOCs result in a sheet resistance modulation of less than 100 mΩ. However, when it comes to the adsorption on the surface of SLG, the process can be seen as random and non-cooperative. This adsorption process is more closely related to the

surface population of molecules rather than their size and specific chemical properties. This is despite the fact that Chen et al. ¹¹⁸ used clustering of EtOH molecules as an example and suggested that this would yield differential responses for MeOH and EtOH. Furthermore, no significant and distinct responses to exposure to MeOH and EtOH were seen because of the SLG's poor ability for adsorption.

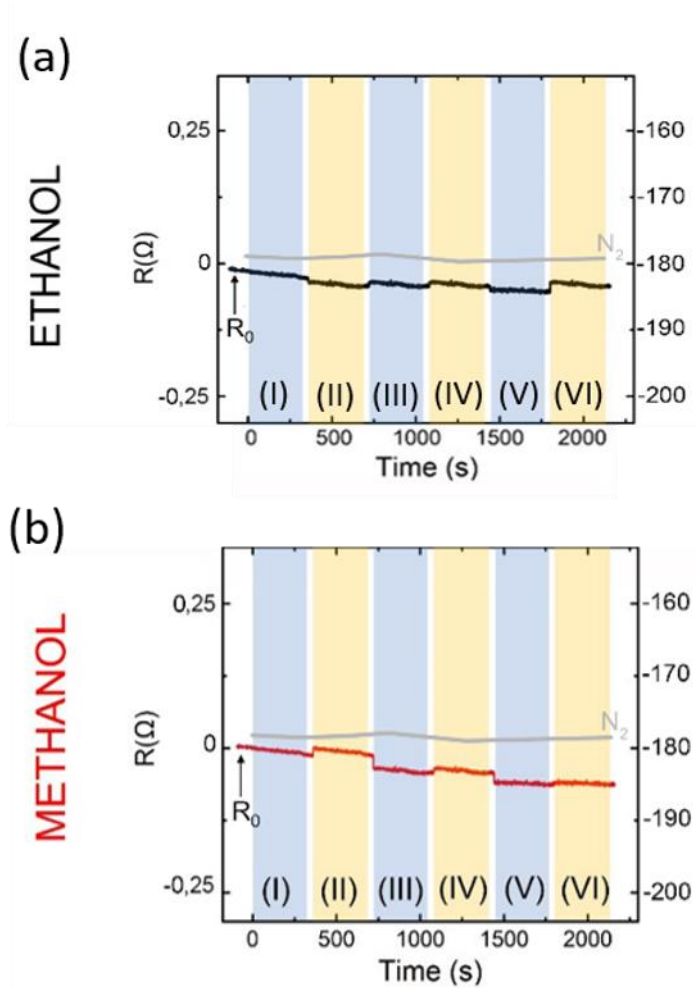


Figure 4.16. Concentration dependent chemiresistor responses of SLG upon exposure to (I) 0.2 ppm (II) 0.5 ppm, (III) 2.5 ppm (IV) 5 ppm (V) 25 ppm and (VI) 50 ppm of MeOH (red) and EtOH (black), measured at room temperature (22 °C). (The gray traces in the graph illustrate the baseline and response stability SLG)

As the concentrations of MeOH and EtOH increased, chemiresistors based on BLG exhibited significant responses. The sheet resistance modulated from 40 Ω to 180 Ω and from 180 Ω to 360 Ω when exposed to 0.2 ppm and 50 ppm of EtOH and MeOH, respectively. Due to the VOCs' adsorption on the BLG surface, the sheet resistance drops across the 100 s VOC exposure window and returns to baseline after the gas chamber is

vented. For both ethanol and methanol, the average response and recovery times were calculated as 80 s and 220 s, respectively, to achieve 90% of steady-state responses ¹¹⁹. The superior adsorption capability of MeOH relative to EtOH is exemplified through the adsorption and desorption behaviors showcased in Figure 4.17, underscoring the value of MeOH adsorption. Therefore, the response of BLG chemiresistors could potentially be influenced by the diffusion and intercalation of VOCs between the layers of graphene, indicating a possible contribution to their behavior which cannot be solely attributed to VOC adsorption on the graphene surface. The intercalation of the MeOH within the two layers of BLG may be the cause of the greater response of MeOH compared to EtOH.

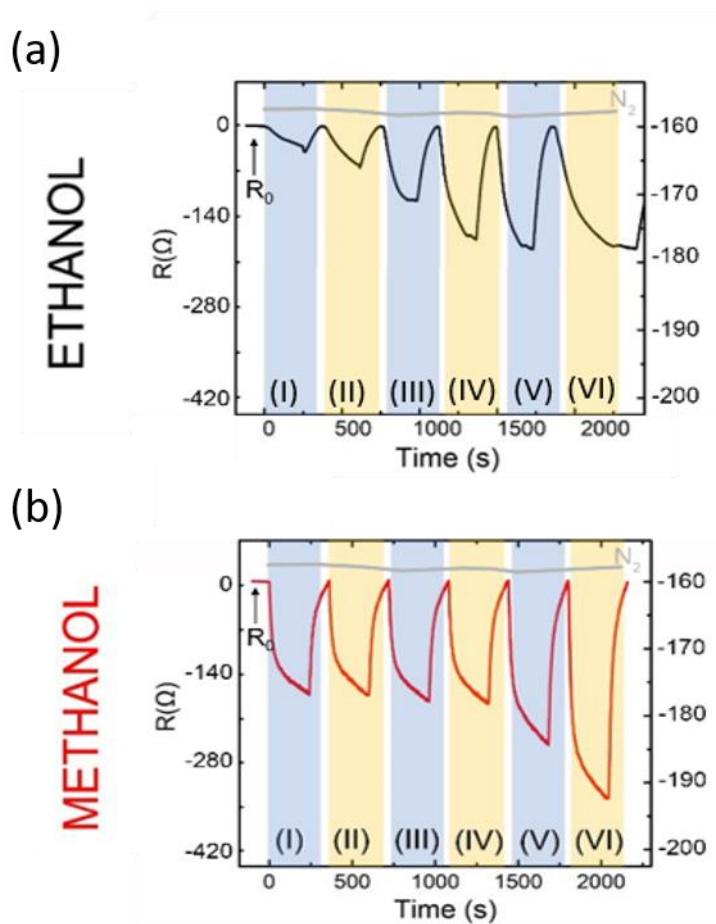


Figure 4.17. Concentration dependent chemiresistor responses of BLG upon exposure to (I) 0.2 ppm (II) 0.5 ppm, (III) 2.5 ppm (IV) 5 ppm (V) 25 ppm and (VI) 50 ppm of MeOH (red) and EtOH (black), measured at room temperature (22 °C). (The gray traces in the graph illustrate the baseline and response stability BLG))

For all of the studied concentrations of EtOH and MeOH, MLG chemiresistors showed much bigger modulations in sheet resistance compared to SLG and BLG (Figure 4.18). The increased responses observed for all test concentrations, surpassing those of SLG/BLG counterparts (reaching up to 2 k Ω for EtOH and 3.2 k Ω for MeOH at the highest test concentration), can potentially be attributed to the larger surface area and multi-layered three-dimensional structure of the sensors. This morphology enhances their capacity for VOC absorption. More importantly, it appears that the MLG shape exhibits stronger signal separation between MeOH and EtOH. This supports the theory that By intercalating MeOH into the layers of graphene, the overall sheet resistance of multilayer graphene MLG is effectively reduced.

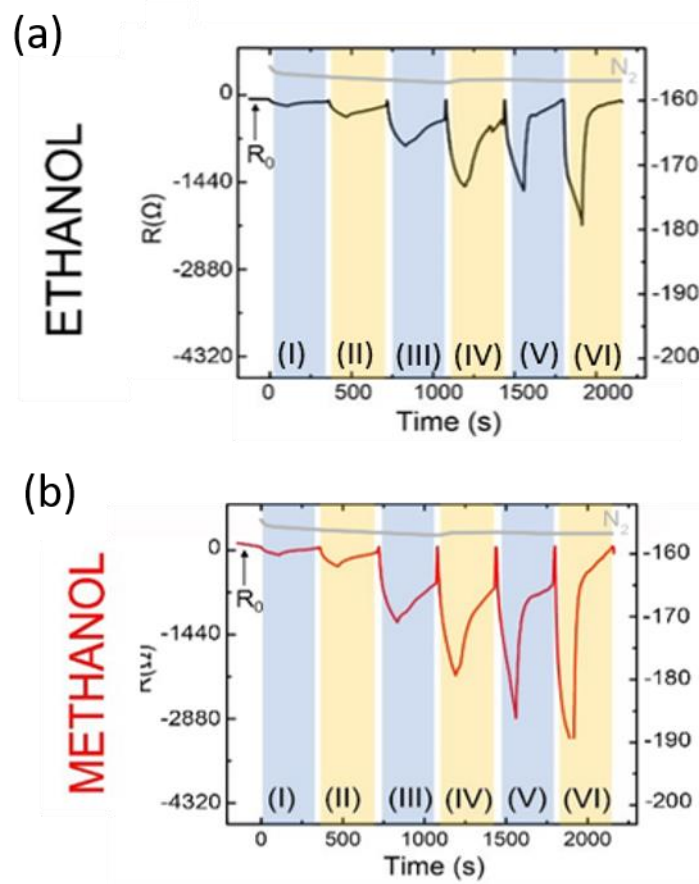


Figure 4.18. Concentration dependent chemiresistor responses of MLG upon exposure to (I) 0.2 ppm (II) 0.5 ppm, (III) 2.5 ppm (IV) 5 ppm (V) 25 ppm and (VI) 50 ppm of MeOH (red) and EtOH (black), measured at room temperature (22 °C). (The gray traces in the graph illustrate the baseline and response stability MLG)

For the exploration of interactions between MeOH/EtOH and graphene morphologies, density functional theory (DFT)-based calculations were carried out using Vienna ab-initio Simulation Package (VASP) with the constructed plane-wave projector-augmented wave (PAW) potentials^{120,121}. The exchange-correlation function was approximated by the generalized gradient approximation (GGA) in the Perdew-Burke-Ernzerhof form¹²². The optB86b-vdw function¹²³ took into account the van der Waals interactions. Bader analysis¹²⁴ was used to determine the charge distribution of the individual MeOH/EtOH molecules and their clusters. The energy cutoff of the plane-wave basis was adjusted at 500 eV for a trustworthy approximation of the molecule-surface system. The set thresholds for electronic and ionic convergence were 10^{-5} and 10^{-4} eV, respectively. At least 10 Å of vacuum space was established to prevent interactions between nearby molecular species. The pressures were optimized structurally until they were less than 1 kB in all directions. The interactions between the graphene surface and a single MeOH/EtOH molecule were then investigated using DFT research. The charge density of the graphene surface and the MeOH/EtOH molecules are adjusted and redistributed at the beginning of adsorption. By using cyan and green colors, respectively, DFT calculations show the graphene and individual MeOH/EtOH molecule charge modulation zones (Figure 4.19 (a)). Individual MeOH molecules' predicted interaction energies of 297 meV and 395 meV, respectively, for EtOH's adsorption on the graphene surface, point to the development of electron transport channels that cause p-type doping of the material. Therefore, the graphene current increases of chemiresistors and the sheet resistance is decreased as a result of MeOH and EtOH adsorption. Regardless of the sizes of the molecule clusters, DFT calculations show that the interaction of EtOH with the graphene surface is energetically more favorable than that of MeOH. The interaction energies of MeOH and EtOH clusters with two to five molecules are shown in Figure 4.19 (b-e). The interaction energy rises as the cluster size does, for example, the pentamer cluster, which contains five molecules, has an interaction energy of 1387 and 1910 meV with the graphene surface for MeOH and EtOH clusters, respectively. Because of the increased interaction energy, larger EtOH cluster sizes are guaranteed to remain on the graphene surface, which prevents their intercalation inside the graphene layers. Additionally, DFT study supports earlier results based on interlayer distance, which would enable molecular size-dependent selective intercalation of tiny compounds, and on interaction energy between analytes and graphene surface. In conclusion, DFT

investigations show that MeOH and EtOH both adsorb on graphene, but MeOH is more likely to intercalate inside the layered graphene than EtOH.

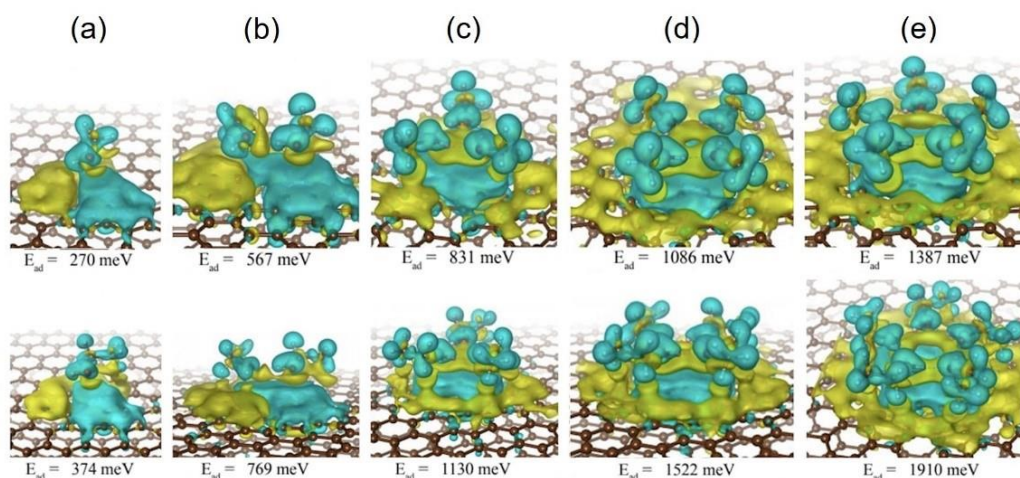


Figure 4.19. Theoretical results indicating the modulations in charge density distributions of graphene (green) and MeOH/EtOH (cyan) molecules upon their adsorption on graphene surface, (a) individual molecule and (b) to (e) two to five molecules, respectively.

By performing chemiresistor measurements at low (20%) and high (80%) RH levels, the effect of relative humidity (RH) on the response of volatile organic compounds (VOCs) was examined. When tested with a concentration of 25 ppm, Figure 4.20 shows that all three chemiresistors displayed comparable reactions at both RH levels, suggesting that variations in humidity levels have little impact on VOC responses. Additionally, the sensor response of the multilayer graphene (MLG) device was evaluated when air and carbon monoxide (CO) were present as interfering gases. According to these results, for MeOH in N_2 , in the presence of CO and air, respectively, the MLG device achieved a response of 95% and 93%. This finding provides evidence for multilayer graphene's (MLG) specific sensitivity to low molecular weight alcohols, contrasting with its lack of response to CO and air. When exposed to different concentrations of MeOH and EtOH; SLG, BLG, and MLG exhibit normalized responses (calculated using $(R-R_0)/R$). The intercalation phenomenon allows for the differentiation between these two VOCs, where the differential responses between MeOH and EtOH increased with the number of graphene layers. The combination of layered morphology and enhanced surface area facilitates the intercalation of MeOH, leading to selective and sensitive detection of MeOH.

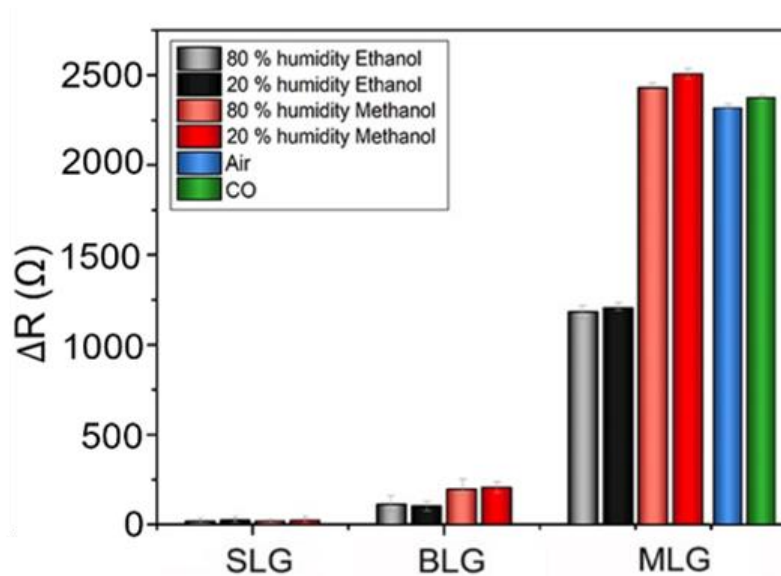


Figure 4.20. Bar graph of RH on chemiresistor responses at 25 ppm of EtOH and MeOH

Figure 4.21 presents the normalized chemiresistor responses of SLG, bilayer graphene BLG, and MLG when exposed to different concentrations of MeOH and EtOH. These graphs depict the varying levels of discrimination observed by the chemical resistors, ranging from no discrimination to partial discrimination and enhanced discrimination of MeOH compared to EtOH. The related regression equations provided in the insets further illustrate these findings.

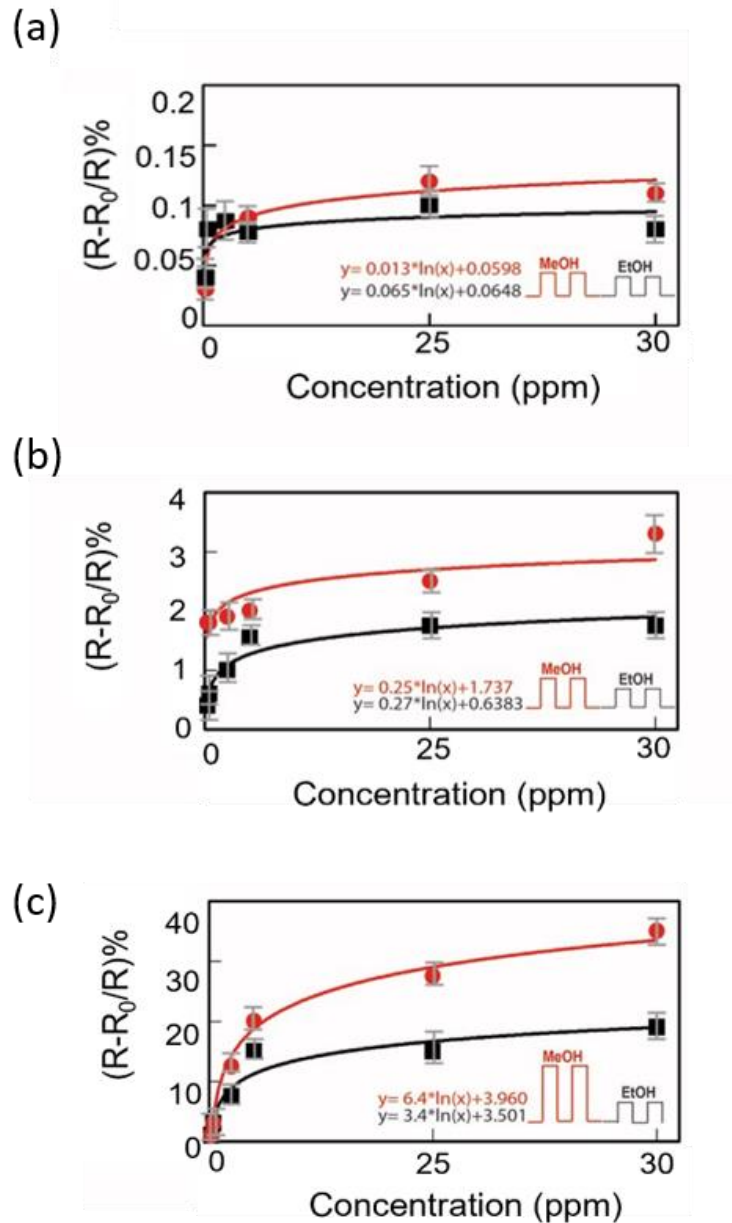


Figure 4.21. Normalized chemiresistor responses of (a) SLG and (b) BLG and (b) MLG upon exposure to varying concentrations of MeOH (red) and EtOH (black).

The impact of temperature fluctuations on the responses of the MLG device was examined at two distinct temperatures, namely 20 °C and 30 °C. Figure 4.22 demonstrates that the chemiresistor responses of MLG exhibited minimal variations within the tested temperature ranges.

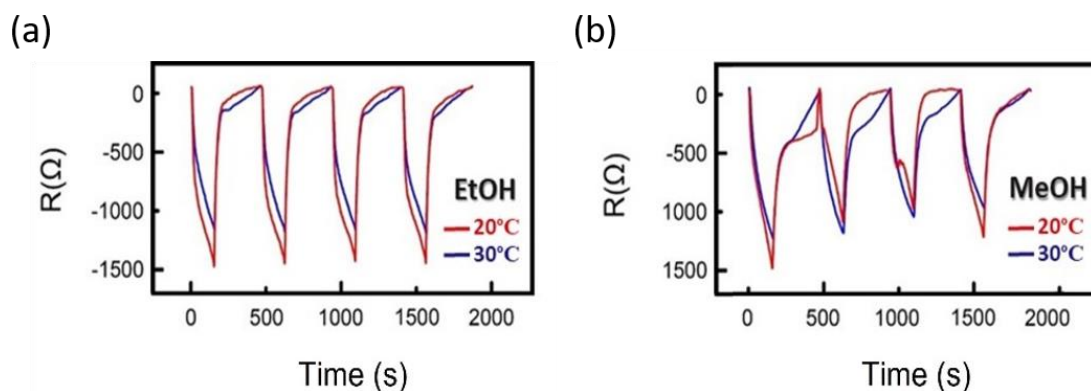


Figure 4.22. (a) The effect of temperature on chemiresistor responses at 25 ppm of EtOH and MeOH measured at room temperature 20 °C and 30 °C

Water/MeOH and water/EtOH intercalation within graphene layers was observed. As seen in Figure 4.23, water/MeOH mixes produced bigger chemiresistor results than water/EtOH mixtures. This finding confirms that the MeOH differential intercalation process as hypothesized is caused by the molecular structure and size of MeOH, which fits the MLG interlayer gap.

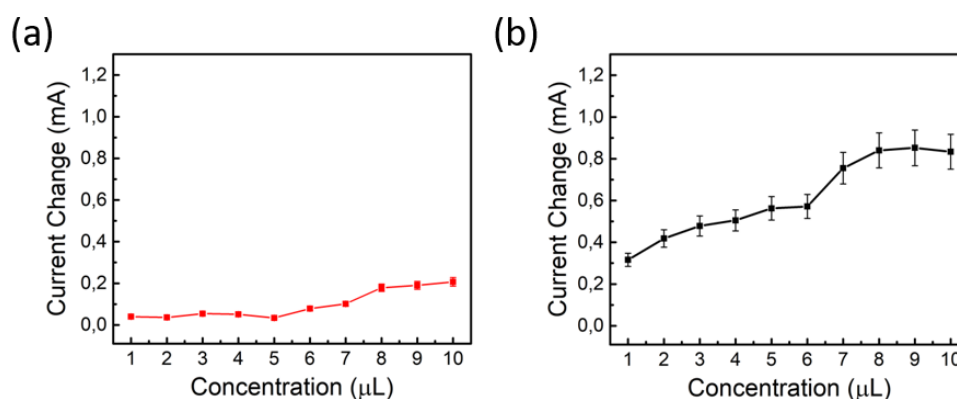


Figure 4.23. a) Concentration dependent response of MLG device in the existence of a) water/EtOH and b) water/MeOH

4.3. Cost-Effective Portable Breath Analyzer for Determination of Volatile Organic Compounds

The importance of developing new diagnostic and detection technologies for the growing number of clinical challenges is rising each year. One safe method for examining human metabolism is breath testing for volatile organic compounds (VOCs). VOCs are a

diverse group of gases that we commonly encounter in our daily lives, including acetone, ethanol, methanol, chloroform, toluene, hexane, isoprene, and others. These hazardous substances can enter our bodies through external exposure to products like paints, adhesives, cleaning agents, disinfectants, cosmetics, air fresheners, and automobile sprays, or they can be produced in our bodies or absorbed from the environment as pollutants. Frequent exposure to VOCs can lead to a variety of serious health issues from a health standpoint, including liver or nervous system problems, an increased risk of cancer¹²⁵⁻¹²⁷ (especially lung cancer), emphysema^{128,129}, allergies¹³⁰ and asthma^{129,131} in humans.

In recent years, high-precision, high time of detection, fast response in a real time, reproducible, stable and inexpensive sensors have become more popular. Heterojunction chemo resistor devices obtained by hybridization of conductive polymers and inorganic nanoparticles provide significant advantages in gas determination because they are easily fabricated, chemically versatile, owing to their low-cost and can be integrated into currently available sensing platforms. In addition, the use of flexible fiber-like nanostructures obtained from conductive polymers in sensor technology provides easy processing and compatibility in the diagnosis of the disease. Fabrication of free-standing nanofibers (Poly (L-lactide-co- ϵ -caprolactone) (PLLCL), Polyurethane (PU) and Polycaprolactone (PCL)) with electrospinning composed of continuous fibers with diameters ranging from tens of nanometers to several micrometers. For flexible sensors, conductive polymers (CPs) draw attention due to their dramatic regulatable conductivity¹³², ease of synthesis¹³³ and low cost¹³⁴. CPs like Poly (3,4-ethylenedioxythiophene) (PEDOT) steps forward based on its high conductivity, stability and optical transparency in the conducting state. On the other hand, carbon nanotube (MWCNT), another interesting nanomaterial, was first observed by Iijima¹³⁵ and multi-walled MWCNT (MWCNT) based gas sensors had great interest owing to their high electron mobility¹³⁶ and high capability of gas adsorption¹³⁷. MWCNT behaves electrically as a thin-film semiconductor with p-type conductivity with the advantage of the sensing properties of the individual nanotubes or their bundles/ropes incorporated in the network. This effect of MWCNTs in the sensing films can be explained by high surface to volume ratio and this results in increasing conducting paths between the electrodes.

Gas sensors have found a wide range of applications from air quality monitoring, detection of toxic gases and explosives, food quality monitoring to medical diagnosis through breath analysis. Most of the commercial sensors in the current market are based

on metal oxides. Although they have good performance, metal oxide based sensors have extreme power consumption and poor chemical selectivity. Mentioned problems have pushed researchers to develop new sensing materials based on organic and composite materials since they have lower power consumption and better chemical selectivity. In addition to this, it is known that humidity plays a significant role in biology, chemistry, human health and even automated industrial processes. In recent years, several CO₂ gas sensors based on a range of physical and chemical principles have been described even though optical devices are the most frequently used today. However, compared with chemiresistive CO₂ sensing devices, they suffer from many drawbacks, such as high cost¹³⁸, complicated and short device life-time¹³⁹ and susceptible to interference gases¹⁴⁰. In this work, surface functionalization of electrospun PLLCL with PEDOT:PSS/MWCNT with Fe and Au NPs is reported and subsequent evaluation of the real time response of these Fe/Au NP functionalized PEDOT:PSS hybrid sensors in humidity environment towards sensing three volatile organic compounds namely acetone, ethanol and hexane is performed.

PVDF dispersion was made by mixing PVDF pellets at a ratio of 25% in 15 mL of 4:1 DMF acetone mixture at 60 °C for 12 hours at 300 cycles in order to create PVDF nanofibers that would be employed as the carrier of the conductive polymer. The prepared dispersion is poured into a syringe with a 20 mL capacity, which is then inserted into the electrospinning apparatus. By using a potential difference of 24 kV, nanofiber production was done at a flow rate of 5 mL/h. The pickup is set to a continuous rotation speed of 500 revolutions per minute during the electrospinning procedure. In order to obtain fiber with the appropriate size and homogeneity, electrospinning was carried out at three different distances. SEM images of PVDF nanofibers produced by electrospinning are shown in Figure 4.24 at distances of 45 mm, 145 mm, and 170 mm. When the distance between the needle and the collection was 170 mm, the images showed the most uniform distribution of nanofibers.

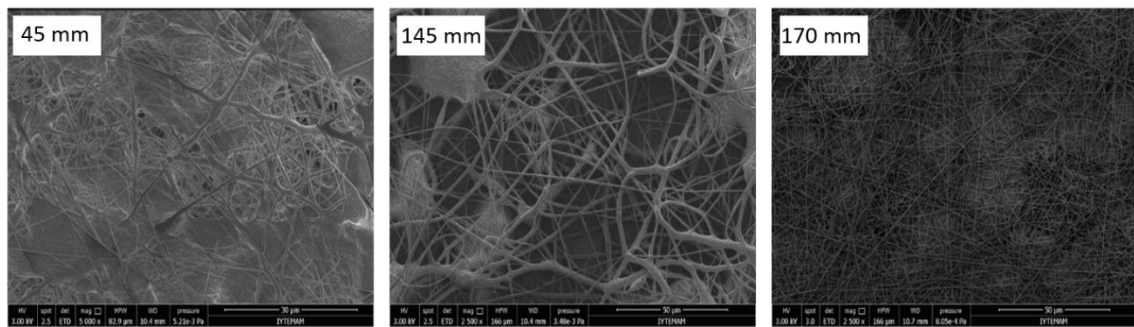


Figure 4.24. Scanning electron microscope images of PVDF nanofibers obtained by electrospinning at a distance of (a) 45 mm, (b) 145 mm and (c) 170 mm

A sensor platform was created using PVDF nanofibers electrospun on a PMMA substrate and modified with CNT and PEDOT: PSS. High resolution surface images were captured using a scanning electron microscope (SEM) at various magnifications to analyse the distribution of the platforms of these conductive components on the surface. CNT bundles are positioned on the surface in the direction of the fibers as a result of the development of PVDF nanofibers as a thin film layer on the surface. It was seen from the images in Figure 4.25 (a-c) that CNT was evenly distributed over the suspended PVDF nanofibers. In addition to this, PEDOT: PSS was covered entirely over the PVDF surface which was clearly seen in Figure 4.25 (d-f).

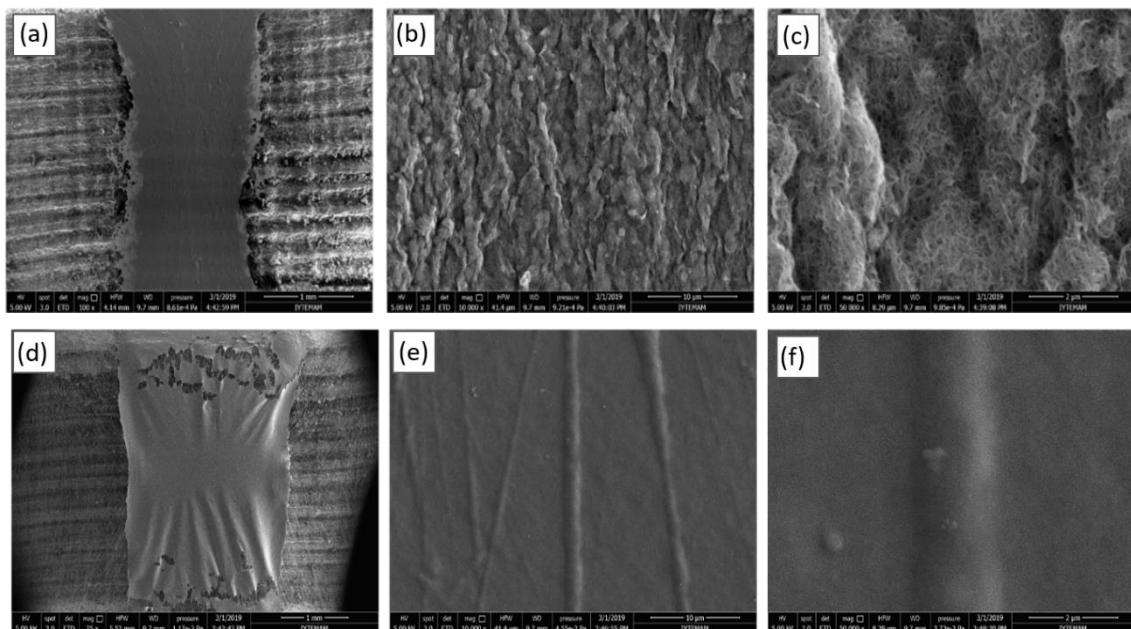


Figure 4.25. Scanning electron microscopy images of (a-c) CNT coated and (d-f) PEDOT: PSS coated PVDF structures at different magnifications coated on PMMA surface by electrospinning method

Figure 4.26 (a-c) depicts SEM images of the gas sensor platform decorated with Au and Fe nanoparticles (NPs) by coating with CNT on PVDF nanofibers at various magnifications. The observations made at 50,000 times magnification revealed the presence of Fe nanoparticles on the PVDF nanofibers. The coating was evenly spread throughout the surface, and no surface tearing was seen, similar to the CNT coated undecorated gas sensor sample. On the other hand, SEM images of the gas platform decorated with Au nanoparticles by coating with CNT on PVDF nanofibers are presented in Figure 4.26 (d-f) at various magnifications. In the same way as with other sensors, homogeneity is not affected. Au NPs were seen to be localized on the CNT in surface pictures that were magnified 50,000 times.

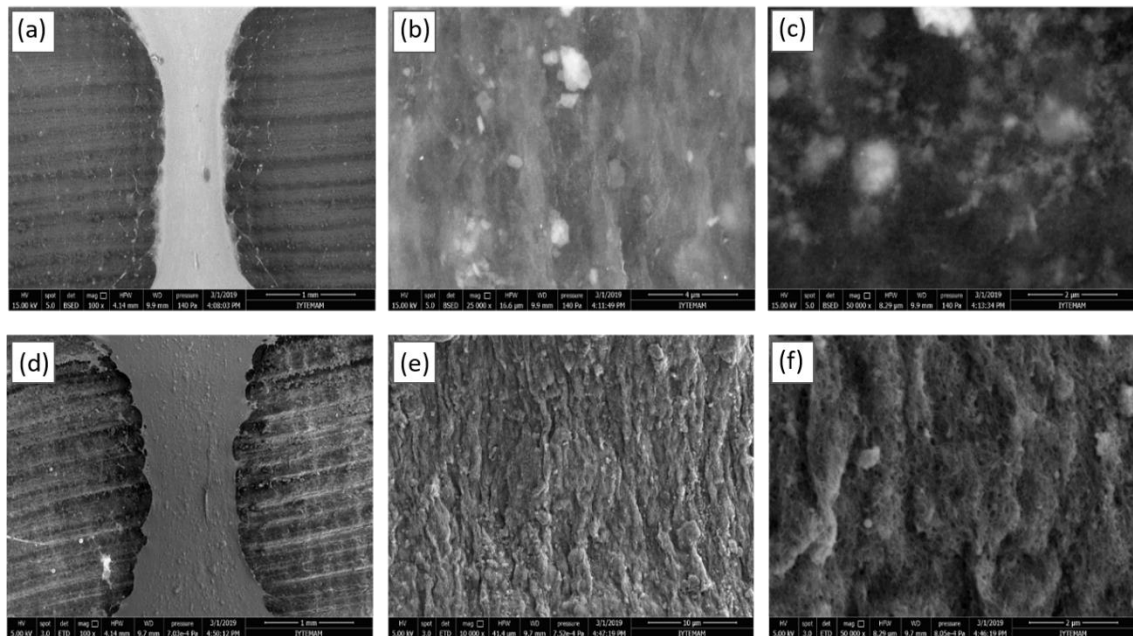


Figure 4.26. Scanning electron microscopy images of (a-c) PVDF-CNT-Au NP and (d-f) PVDF-CNT-Fe NP coated structures at different magnifications coated on PMMA surface by electrospinning method

Figure 4.27 shows various magnifications of SEM images of the gas sensor coated with PEDOT: PSS polymer on PVDF nanofibers. Tears were seen on the PVDF nanofibers coated with PEDOT: PSS polymer, but not on the PVDF nanofibers coated with CNT. The primary causes of ripping are due to phase separation¹⁴¹ of the hybrid material generated by PEDOT:PSS and PVDF during drying and the resultant reduction in the mechanical strength of the layers rich in PEDOT:PSS or PVDF. In general, it has been found that when the film thickness is greater than 500 nm, cracks develop on the sensor contact. The surface image of PVDF nanofibers decorated with Au and Fe

nanoparticles was also displayed in Figure 4.27 (a-c) and (d-f), respectively, and it was found that the PEDOT:PSS sample with Fe nanoparticles had the greatest tearing impact. More tears were produced as a result of the aggregated Fe nanoparticles' effect on the PEDOT:PSS polymer's ability to reduce the mechanical strength of the nanofibers. As a result, CNT-PVDF and PEDOT:PSS-PVDF were accepted as mechanically stable, but metal nanoparticle modification was found to cause partial deformations on the surface in these configurations.

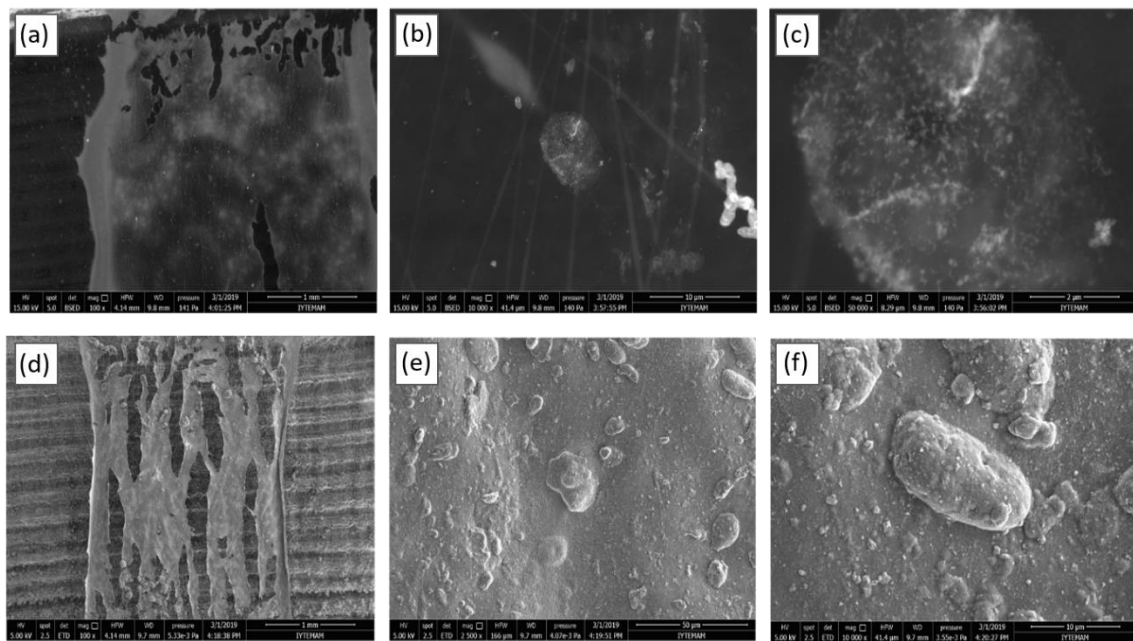


Figure 4.27. Scanning electron microscopy images of (a-c) PVDF-PEDOT: PSS-Au NP and (d-f) PVDF- PEDOT: PSS -Fe NP coated structures at different magnifications coated on PMMA surface by electrospinning method

15% by weight PU dispersion was created by mixing in the presence of a DMF solution at 500 cycles for a period of 12 hours in order to create PU nanofibers that would be applied to a PMMA substrate. Using a potential difference of 25 kV, nanofiber synthesis was carried out at a flow rate of 2 mL/h using the produced dispersion in a 20 mL syringe within the electrospinning apparatus. The needle-to-collector distance was adjusted to 170 mm, and the collector's continuous rotation speed was 500 revolutions per minute during the electrospinning procedure. Figure 4.28 shows the high resolution SEM images of electrospun PU nanofiber coated with CNT and PEDOT: PSS on PMMA surface. According to the images, CNT shows (Figure 4.28 (c-d)) a homogeneous distribution on PU nanofibers. On the other hand, PSS particles are seen on the PU sensor platform coated with PEDOT: PSS Figure 4.28 (e-f).

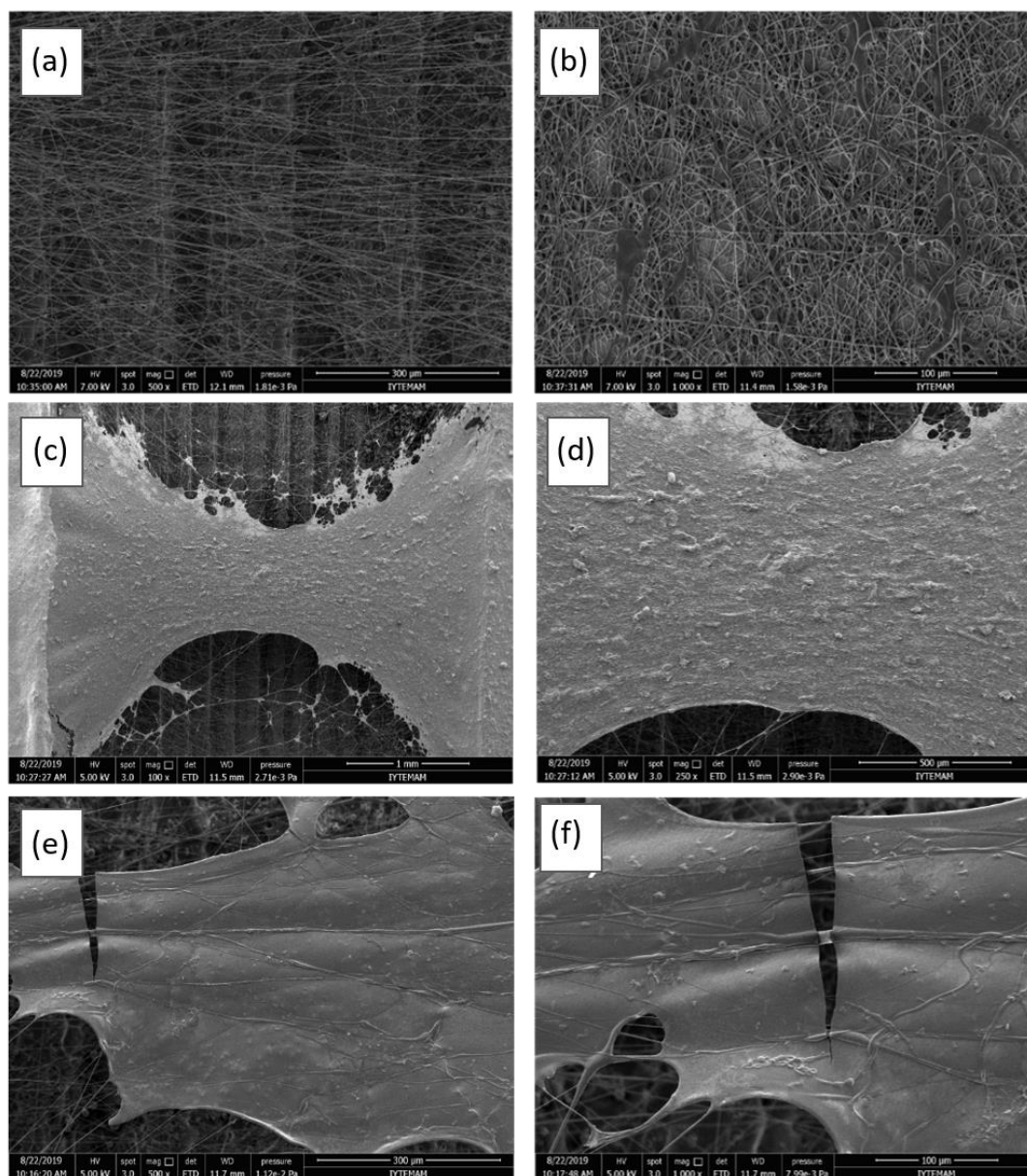


Figure 4.28. Scanning electron microscopy images of (a-c) PU, (d-f) CNT coated and (g-i) PEDOT: PSS coated PU structures at different magnifications coated on PMMA surface by electrospinning method

20% by weight PCL dispersion was created by mixing in a DCM/DMF (4:1) solvent mixture at 500 cycles for 12 hours in order to create PCL nanofibers. A 20 ml syringe was used to transfer the produced dispersion into the electrospinning apparatus. The settings for the electrospinning process were 29 kV voltage, 2 ml per hour flow rate, and 170 mm needle-to-collector distance. The collector rotated at a steady 500 revolutions per minute during the electrospinning process, producing nanofibers. Figure 4.29 shows the high resolution SEM images of electrospun PCL nanofiber coated with CNT and PEDOT: PSS on PMMA surface. According to the images, CNT shows (Figure 4.29 (c-

d)) a homogeneous distribution on PCL nanofibers. On the other hand, PSS particles are seen on the PCL sensor platform coated with PEDOT: PSS Figure 4.29 (e-f).

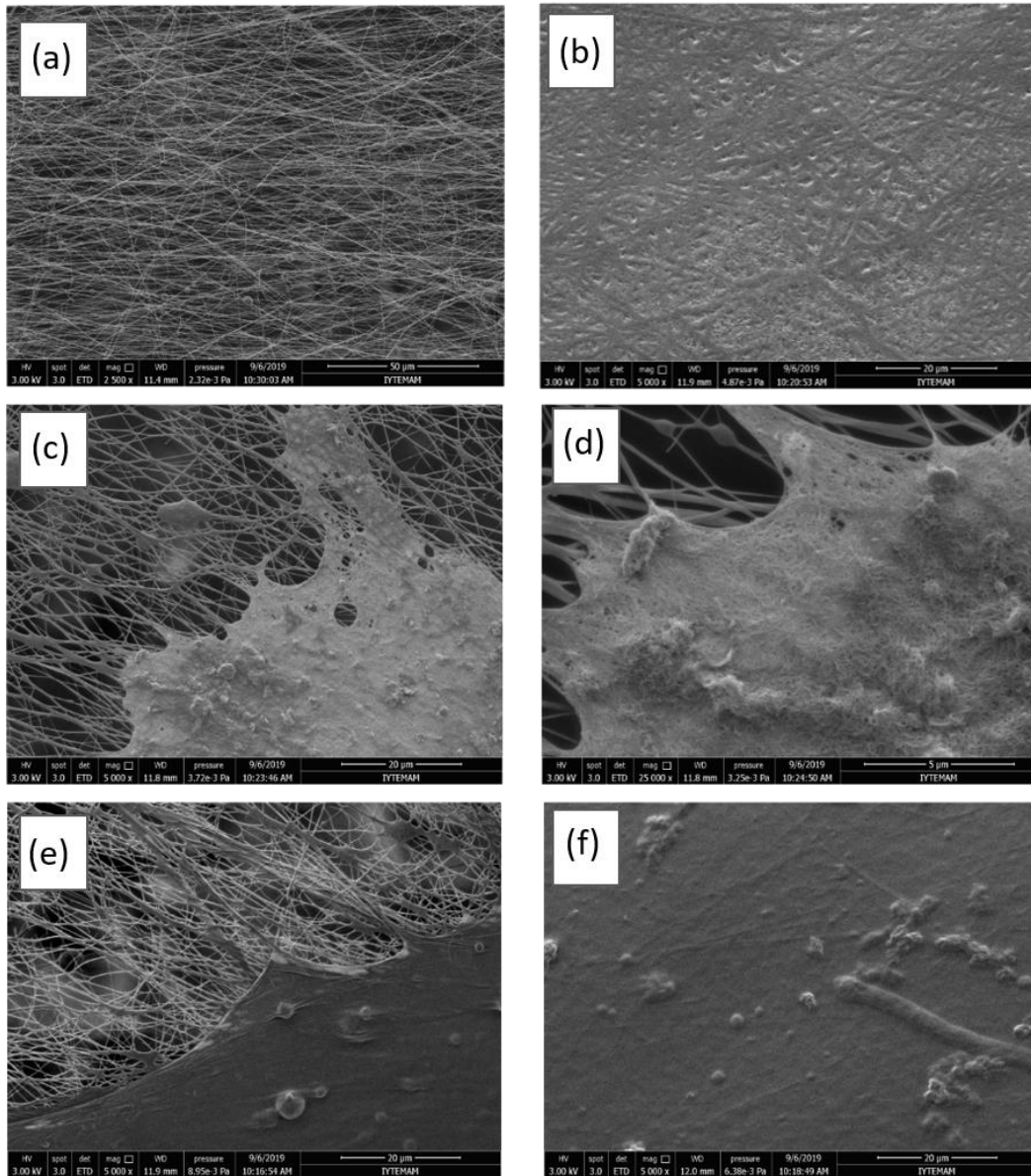


Figure 4.29. Scanning electron microscopy images of (a-c) PCL, (d-f) CNT coated and (g-i) PEDOT PSS coated PCL structures at different magnifications coated on PMMA surface by electrospinning method

10% by weight PLLCL dispersion was created in a DCM/DMF (9:1) solvent mixture and swirled on a magnetic stirrer for one day in order to create PLLCL nanofibers. The 20 ml syringe was filled with the polymer solution when the PLLCL had been entirely dissolved, and it was attached to the electrospinning assembly's syringe pump. On the collector, PMMA substrates are positioned and covered with aluminium

foil. The electrospinning parameters were adjusted to a voltage of 25 kV, a flow rate of 3 mL/h, and a needle-to-collector distance of 180 mm. Figure 4.30 (a-b) shows SEM images of PLLCL nanofibers at various magnifications. The radius of the PLLCL fibers were measured as approximately 0.7 μm . When SEM images of PLLCL nanofibers coated with CNT were examined, it was seen that the structure showed a homogeneous distribution on the fibers Figure 4.30 (c-d). On the other hand, the same behaviour was observed on PLLCL fibers coated with PEDOT: PSS. In addition, it is clearly presented in Figure 4.30 (e-f) that no tear was observed on the PEDOT: PSS coated surface.

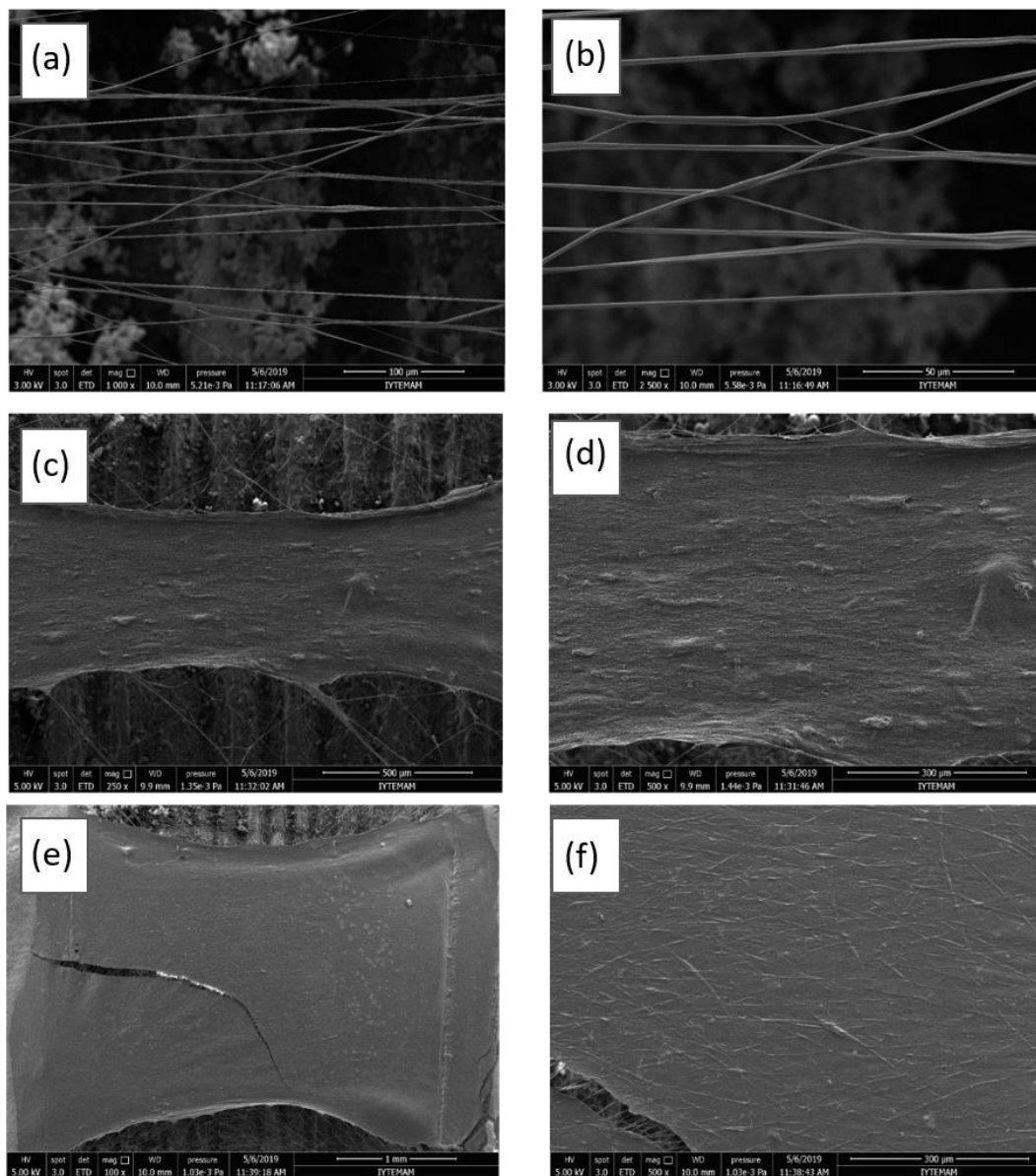


Figure 4.30. Scanning electron microscopy images of (a-c) PLLCL, (d-f) CNT coated and (g-i) PEDOT: PSS coated PLLCL structures at different magnifications coated on PMMA surface by electrospinning method

Figure 4.31 shows that surface characteristics of free-standing PEDOT: PSS-PVDF and MWCNT-PVDF conductive nets with AFM measurements. As can be seen in the two-dimensional AFM images, PEDOT: PSS-PVDF conductive net is made of PSS domains (few hundreds nm in diameter) embedded in PEDOT phase (Figure 4.31 (a)). Figure 4.31 (b) shows cross section of PEDOT:PSS-PVDF conductive net and the root mean square roughness was found to be as $0.12\ \mu\text{m}$. Figure 4.31 (c) depicts the AFM imaging of MWCNT-PVDF conductive nets that exhibit single phase, rough surface property. The root mean square roughness was calculated as $1.53\ \mu\text{m}$ (see the height profile in Figure 4.31 (d)). The mechanical strength of free-standing conductive nets was analyzed by nano indentation measurement shown in Figure 4.31 (e). The Young's modulus of two conductive nets of PEDOT: PSS and MWCNT were calculated as $0.18\ \text{Pa}$ and $0.3\ \text{Pa}$, respectively. As shown in Figure 4.31 (e) inset, there is a significant difference between the maximum pull-off force ($30\ \text{nN}$) of PEDOT: PSS and MWCNT (nearly $0\ \text{nN}$). This difference may be attributed to the strong adhesion due to electrostatic interactions between AFM tip and PSS domains. In contrast MWCNT and AFM tip only exhibit Van der Waals interactions hence pull-off force is substantially weak. That's why the sensing network plays a crucial role in the sensor and its structural characteristics will affect directly the sensing performance.

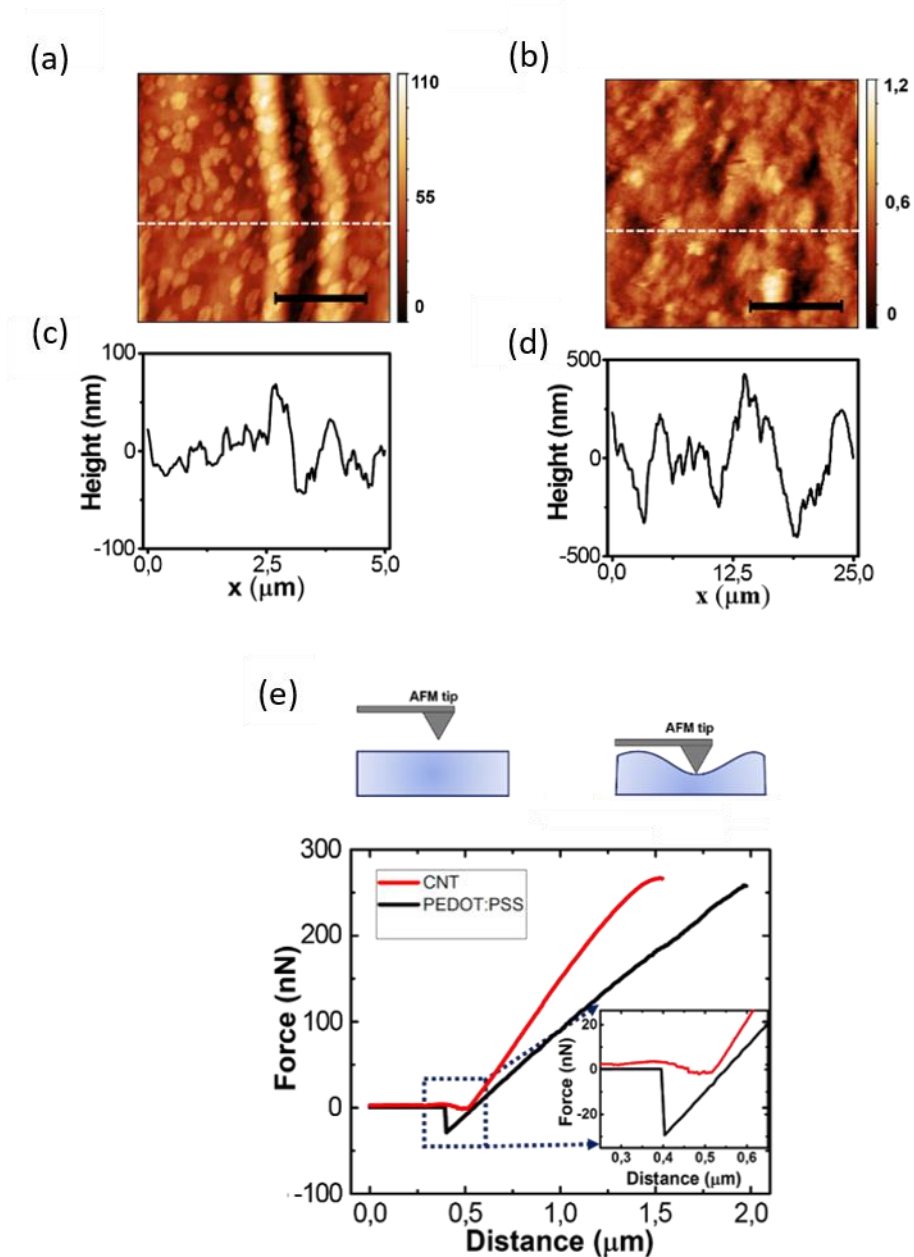


Figure 4.31. 2D topographical image of PVDF-PEDOT: PSS and PVDF-CNT conductive nets with the range of μm scale (scale bars are $10 \mu\text{m}$ and $2 \mu\text{m}$, respectively) (a-b) their height profiles (c-d) and e) F-d analysis of PVDF-PEDOT: PSS and MWCNT network

Figure 4.32 (a) and (b) depicts the 3D conductive AFM (c-AFM) images of PEDOT: PSS and MWCNT layer onto PVDF substrate with three different points, respectively. As seen from the topography measurements, MWCNT was homogeneously coated on the surface, while crystallized PSSs were observed with the formation of a homogeneous film consisting of PEDOT on the PVDF nanofibers. MWCNTs, on the other hand, are homogeneously distributed over the entire surface by entangling each

other. These results suggest with the surface conductivity of PEDOT: PSS and MWCNT coated elements. According to these results, while MWCNT surfaces exhibit homogeneous I-V behavior and I-V measurements taken from 3 different points, the current value was measured as 150 nA at each point. However, PEDOT: PSS coated surfaces show more variable. While the current value measured according to the I-V measurement taken over PEDOT is 20 nA, the maximum current value read over the PSS islands is 130 nA. In addition, the current read from the surface is measured as only 2 nA. The lack of electrical conductivity is due to the insulating PSS shell that restricts the transmission of charge across the grains, even though the core is rich in conductive PEDOT. Therefore, the heterogeneous structures recorded on the PEDOT: PSS surface suggest that PEDOT-rich aggregates and the remainder of the film are composed of insulating PSS^{142,143}. It was thought that this heterogeneity would affect the final sensor response. For this reason, PEDOT: PSS and MWCNT hybrids will be doped with Au and Fe nanoparticles, as it is thought that these configurations will change the electrical conductivity of the sensor platforms and thus increase the volatile organic compound selectivity.

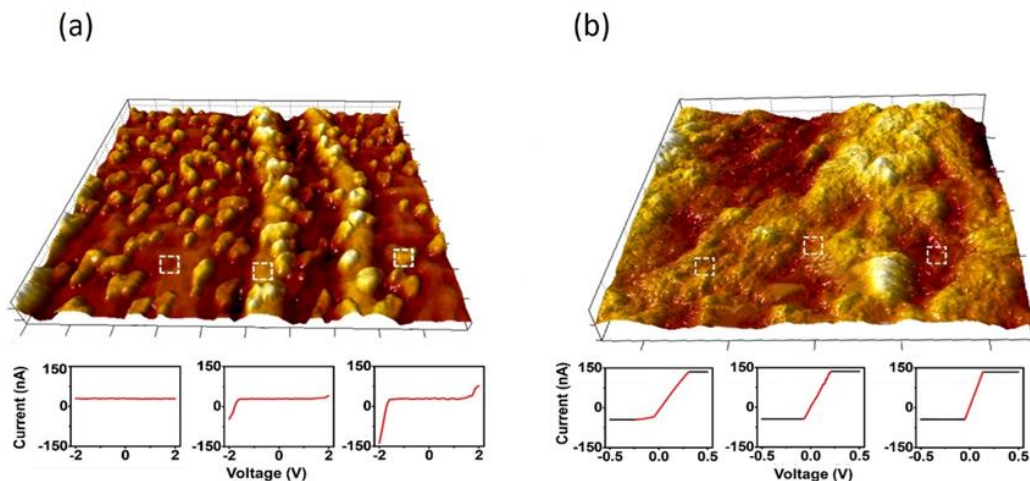


Figure 4.32. Conductive AFM topography imaged and I-V characteristics of (a) PEDOT: PSS and (b) MWCNT nets which were measured from three different locations (below)

Chemical sensing behaviours were analysed against acetone and ethanol. The gas chamber containing VOC vapour was generated from bubblers that were immersed in carrier gas. Gas concentration adjusted to the desired amount (0.5 ppm to 100 ppm) by using computer driven mass flow controllers. Typical experiments consisted of repeated

exposure to the VOC gas (4 min) and a subsequent purging with pure N₂ (2 min). The temperature of the sensor platform was kept at room temperature (23 °C) with the help of temperature control.

The repeatability (Figure 4.33 (a)) and time dependent current change results (Figure 4.33 (b)) of the responses of PVDF-MWCNT, PU-MWCNT, PCL-MWCNT and PLLCL-MWCNT structured sensor platforms to ethanol and acetone gases are shown under 1V voltage with 400 seconds intervals (the mean and standard deviation of five different sensors from each platform are taken into account). According to the results, the sensors in the PVDF-MWCNT and PLLCL-MWCNT give responses at only 0.5 ppm both acetone and ethanol gases. However, in the PVDF-MWCNT structured sensor, the standard deviation was found to be high in 0.5 ppm. For PLLCL-MWCNT structured sensor platform, the current change between 0.5-100 ppm ethanol was recorded as 5-25 μ A while current change between 0.5-100 ppm acetone was recorded as 0-17 μ A. In addition to this, the lowest standard deviation for both acetone and ethanol over the entire concentration range was observed for sensors in the PLLCL-MWCNT sensor platform. In literature, it is well to increase the resistance thus decrease the current when compared to high dielectric constant analyte ($\epsilon_{\text{ethanol}} = 24.3$)^{144,145}. Thus, high dielectric constant with ethanol reduce the Coulomb interaction and screening effect occurs between PLLCL and MWCNT. This screening effect enhances the hopping rate and conductivity. Therefore, the current we measured in the PLLCL/MWCNT hybrid sensor structure of ethanol gas, especially at high concentrations, is about 2 times higher than that of acetone gas. As a result, this results indicates that the PLLCL-MWCNT hybrid structure has exhibited effects such as increasing mechanical strength, reducing the irreversible effects of gas, and preserving fiber flexibility, resulting in the formation of a sensor structure with high repeatability and responsiveness between 0.5-100 ppm acetone and ethanol.

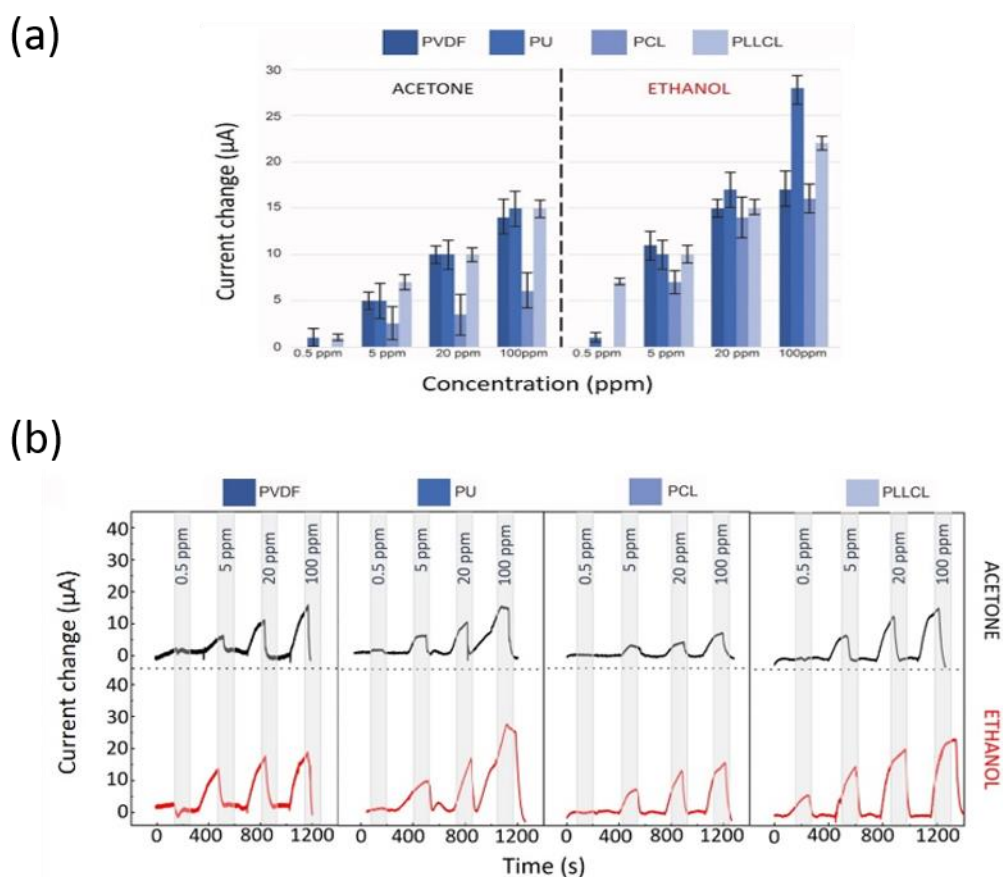


Figure 4.33. (a) PVDF-MWCNT, PU-MWCNT, PCL-MWCNT and PLLCL-MWCNT structured sensor platforms reproducibility results of their responses to ethanol and acetone gases (b) Time dependent current change measurements given to ethanol and acetone between 0.5-100 ppm gas concentrations (average and standard deviation of five different sensors from each platform were taken into account).

Figure 4.34 (a) and (b) indicates that the reproducibility and time dependent current change results of the responses of PVDF-PEDOT: PSS, PU- PEDOT: PSS, PCL- PEDOT: PSS and PLLCL- PEDOT: PSS structured sensor platforms to ethanol and acetone gases, respectively. Contrary to MWCNT-structure based sensor platforms, responses were obtained only from the sensor in the PVDF- PEDOT: PSS-configuration at 0.5 ppm both acetone and ethanol. However, in the PEDOT: PSS-PVDF configuration, it was found that the standard deviation was high at 0.5 ppm. Although PLLCL-PEDOT: PSS structure response to ethanol and acetone at 0.5 ppm was not observed, signal increase was observed due to the increased amount of gas at other concentrations and the current change was measured as about 18 µA at 100 ppm for acetone and ethanol. The reason for the lower response of sensors coated with PEDOT: PSS compared to ethanol gas in all sensor configurations is due to the swelling of PEDOT: PSS nanofibers when

exposed to acetone ¹⁴⁶. This swelling leads to damage to the conductive pathways between PEDOT and PSS. In the light of all these results, it has been measured that the responses of PLLCL-based hybrid structures in conductive fiber structure decorated with MWCNT and PEDOT: PSS against acetone and ethanol vapour are most suitable for the sensor structure.

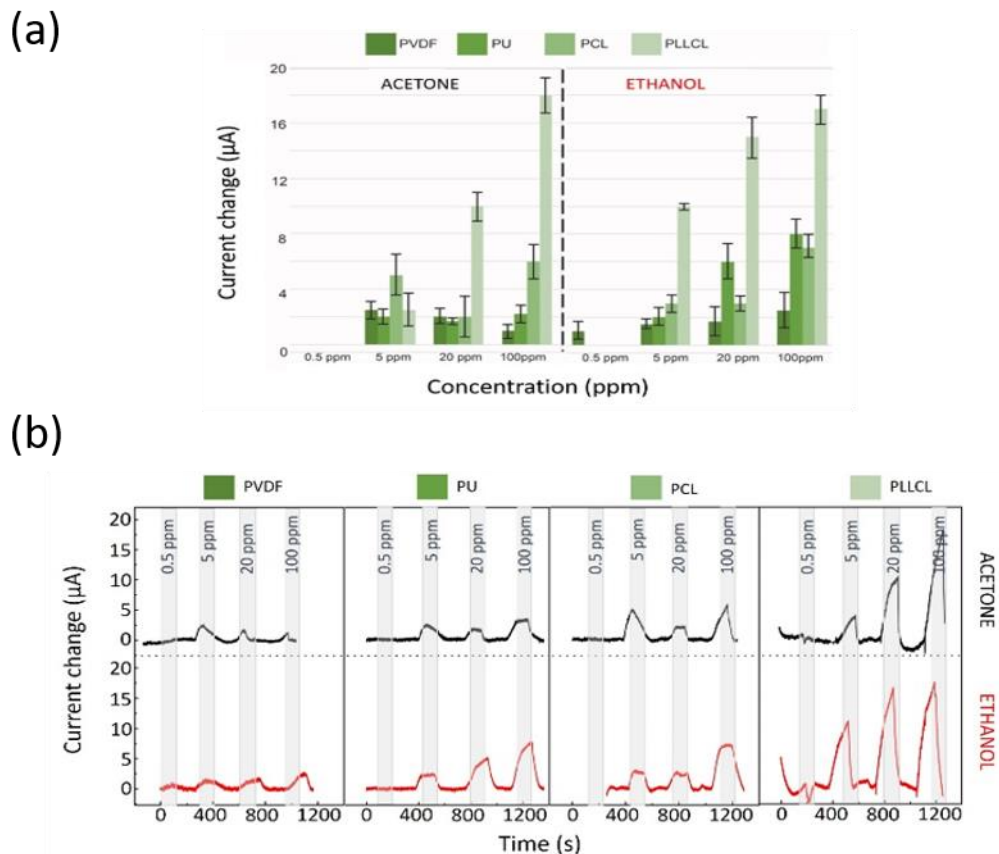


Figure 4.34. (a) PLLCL- PEDOT: PSS structured sensor platforms reproducibility results of their responses to ethanol and acetone gases (b) Time dependent current change measurements given to ethanol and acetone between 0.5-100 ppm gas concentrations (average and standard deviation of five different sensors from each platform were taken into account).

MWCNT based PLCLL hybrid sensor platforms were decorated with conductive Au and Fe nanoparticles (NP) to improve the electrical response to acetone, ethanol and hexane in humidity environment. Time dependent current change graph of Au and Fe NP decorated PLLCL-MWCNT based sensor platforms to acetone, ethanol and hexane (0.5 ppm to 100 ppm) to 30%, 50% and 70% humidity environment measurement was measured. For both devices and the humidity conditions, sensor response rises along the humidity increases. This increment behaviour can be explained that the MWCNTs are p-

type semiconductors, in which air holes serve as the primary charge carriers. Water molecules can provide MWCNTs electrons since water vapour is often a reduced gas. When a MWCNT based sensor is exposed to water molecules, a charge transfer occurs between the water molecules and MWCNT. The observed phenomenon leads to a reduction in the carrier concentration present within the MWCNT, consequently resulting in a decrease in the conductivity of the sensor¹⁴⁷. In the case of humidity environment, Au and Fe decorated sensor exhibit diminished sensitivity to water molecules. This leads to an enhanced performance characterized by improved stability as well as enhanced response and recovery capabilities.

In humidity environment, a linear response to acetone between 0.5-100 ppm was not obtained on the MWCNT-PLLCL and MWCNT-PLLCL-Au sensor platform (Figure 4.35). The interference caused by moisture (water vapour) has shown to disrupt the response to acetone in the PLLCL MWCNT- and PLLCL- MWCNT-Au sensor platforms. In this case, two scenarios can be considered i) water molecules interacting with the PLLCL surface, causing deformation in the polymer nanofibers, and indirectly creating extra roughness on the MWCNT surface, creating a conductivity-reducing effect ii) interactions of water molecules with the MWCNT surface, weakening the volatile organic-MWCNT interaction (volatile organic MWCNT removal from the surface). Bachar and Bayn indicates the effect of relative humidity water molecules^{148,149}. The first scenario involves measuring the return of the base current to its initial level after the evacuation of volatile organic compounds with N₂ at different relative humidity levels. This supports the notion that the interaction between water molecules and volatile organics with the surface is reversible. In the second scenario, the negative impact of relative humidity on the sensor performance is explained by the signal-reducing effect of water molecules on field-effect transistor-type gas sensor platforms made of polyaromatic layers. This occurs because the condensation of water molecules on the hydrophobic layer prevents the interaction of volatile organics with the surface. As a result, the decline in sensor performance caused by an increase in relative humidity can be attributed to the interaction and condensation of water molecules with the surface of the MWCNT. The impact of 30% relative humidity on the PLLCL- MWCNT-Fe hybrid chemoresistor platform is shown as a black line. The sensor was exposed to acetone concentrations ranging from 0.5 to 100 ppm in an environment with 30% relative humidity, and it demonstrated an increasing response between 1-20 μ A as the concentration increased. The presence of Fe NPs in the configuration, ensures that the sensor operates unaffected

by moisture, compared to the response observed in the absence of Fe NPs. This is possible due to the surface properties of the Fe NPs, which lead to the condensation of water molecules on themselves²⁹. On the other hand, the sensor platform made of PLLCL-MWCNT and PLLCL-MWCNT-Au did not exhibit a linear response between 0.5-100 ppm of acetone in all humidity conditions. However, it was observed that despite experiencing a loss of 2.5 μA at 100 ppm, the correlation between concentration and current increase was not affected and the sensor still provided a response. When exposed to acetone ranging from 0.5 to 100 ppm concentrations in an environment with 70% relative humidity, the sensor exhibited an increasing response between 4-17.5 μA as the concentration increased. Although there was no loss observed at 100 ppm compared to the results obtained in 50% relative humidity, the current response deviated from the linear increase response at concentrations of 0.5 and 5 ppm, as well as at 20 and 50 ppm, affecting the correlation between concentration and current increase. These measurements indicates that 70% relative humidity is close to the limit of Fe NPs water-carrying capacity.

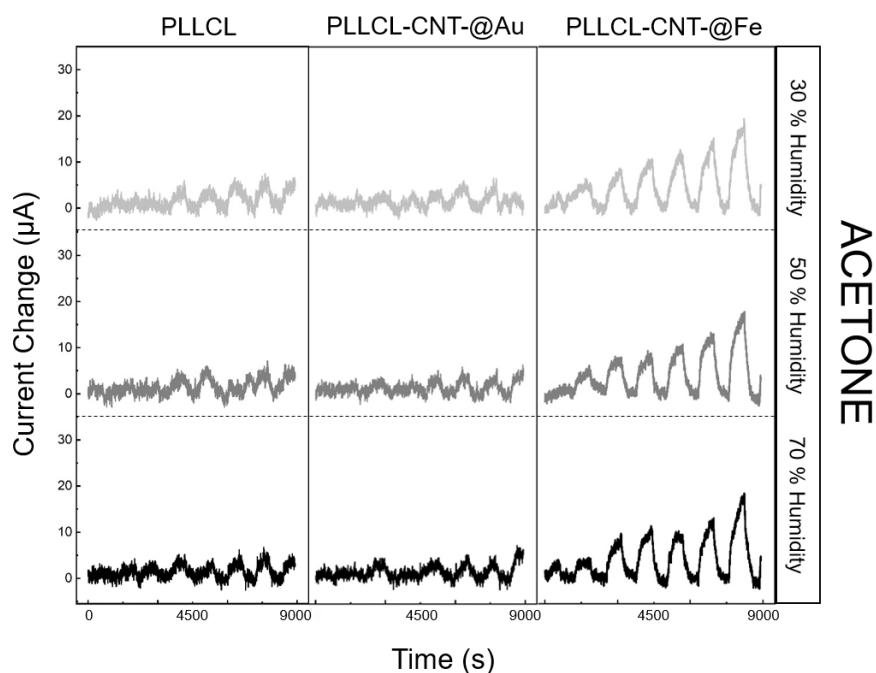


Figure 4.35. Time dependent current change graph of PLLCL, PLLCL-MWCNT-Au and PLLCL-MWCNT-Fe nanoparticle decorated sensor platform measurements to 0.5-100 ppm range of acetone with 30%, 50% and 70% humidity environment.

The electrical responses of the sensor platform PLLCL-MWCNT decorated with Au and Fe nanoparticles to ethanol in the humidity environment are shown with red tones in Figure 4.36. In humidity environment, the PLLCL-MWCNT sensor platform did not respond to ethanol concentrations of 0.5, 5, and 10 ppm, but exhibited an increased current response between 20-100 ppm. On the other hand, responses that were mostly considered as noise were obtained with the PLLCL- MWCNT-Au sensor. The PLLCL-MWCNT-Fe sensor, which was exposed to 0.5-100 ppm ethanol in a 30% relative humidity environment, gave an increased response between 2.5-30 μA at 50% humidity compared to the concentration increase. On the other hand, in the PLLCL-MWCNT-Fe sensor platform at 70% humidity, no response loss was observed compared to 50% relative humidity. Based on the measurements conducted, it can be concluded that the PLLCL-MWCNT-Fe sensor platform was the least affected by humidity conditions and exhibited the smallest loss in performance. However, in humidity environment, the PLLCL-MWCNT and PLLCL- MWCNT-Au sensor platforms dose not exhibit an increased current response within the hexane concentration range (Figure 4.37). The signal-to-noise ratio was found to be high while the concentration correlation was low, which calculated as 1 at hexane concentrations of 0.5 and 5 ppm, and 3 at 100 ppm.

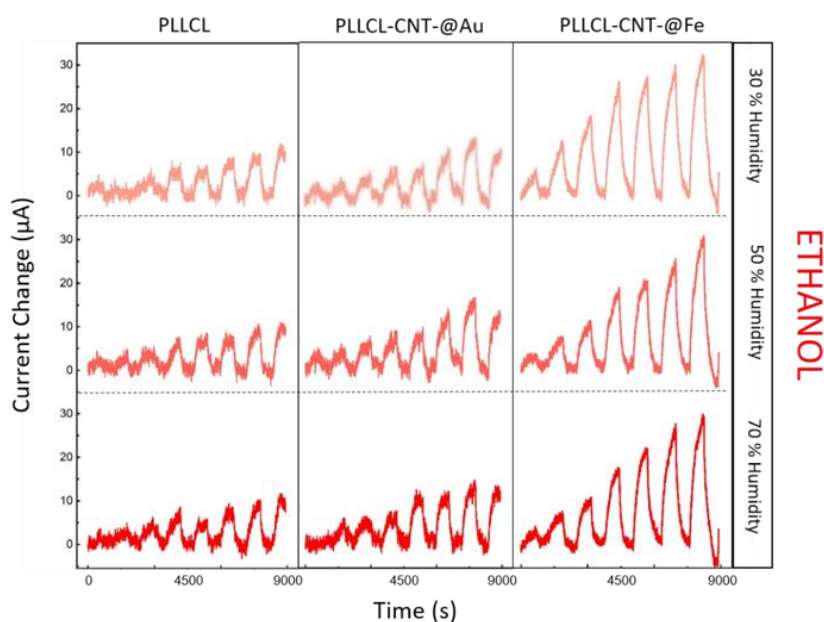


Figure 4.36. Time dependent current change graph of PLLCL, PLLCL-MWCNT-Au and PLLCL-MWCNT-Fe nanoparticle decorated sensor platform measurements to 0.5-100 ppm range of ethanol with 30%, 50% and 70% humidity environment

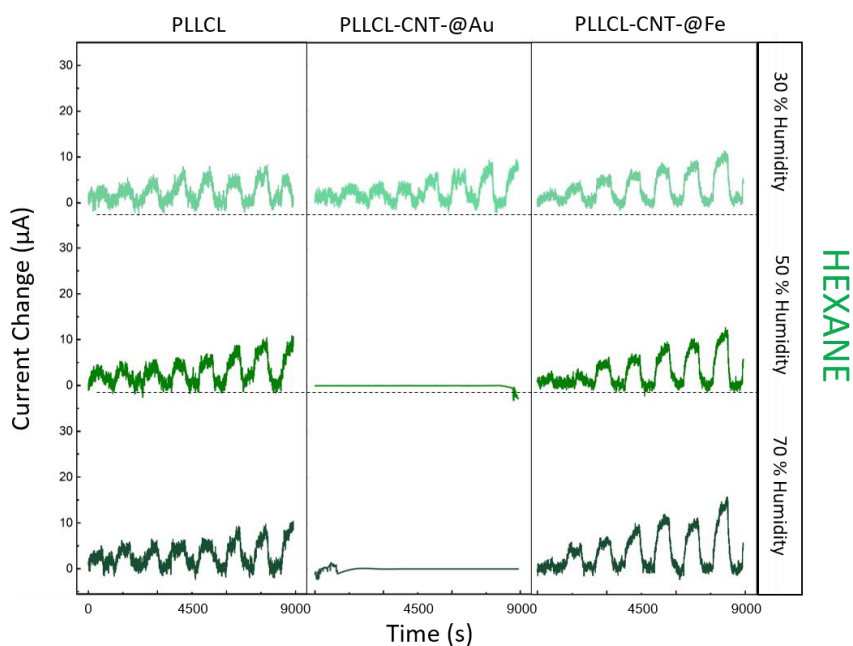


Figure 4.37. Time dependent current change graph of PLLCL, PLLCL-MWCNT-Au and PLLCL-MWCNT-Fe nanoparticle decorated sensor platform measurements to 0.5-100 ppm range of hexane with 30%, 50% and 70% humidity environment.

A prototype of the device capable of detecting carbon dioxide/VOC was produced and end-user tests were completed. The test results were presented by principal component analysis (PCA) and the data obtained from two different concentrations of acetone, toluene, formaldehyde and ethanol were evaluated (Figure 4.38). Aggregation trend was investigated for ethanol, acetone, toluene, and formaldehyde using infrared (IR) and principal component analysis of data collected from the sensor. In this analysis, the first component is the signal strength (IR absorbance value), and the second component was chosen as the wave number (characteristic peaks: acetone=1710 cm^{-1} , Formaldehyde= 2785 cm^{-1} , Toluene= 700 and 1440 cm^{-1} , Ethanol= 3350 cm^{-1}). It was determined that in the case of VOC concentration of 10 ppm, all four VOCs were separated from each other and could be distinguished. Especially, toluene showed a narrower distribution compared to other volatiles. The results revealed that VOCs can be separated from each other at the ppm level and the sensor behaves selectively.

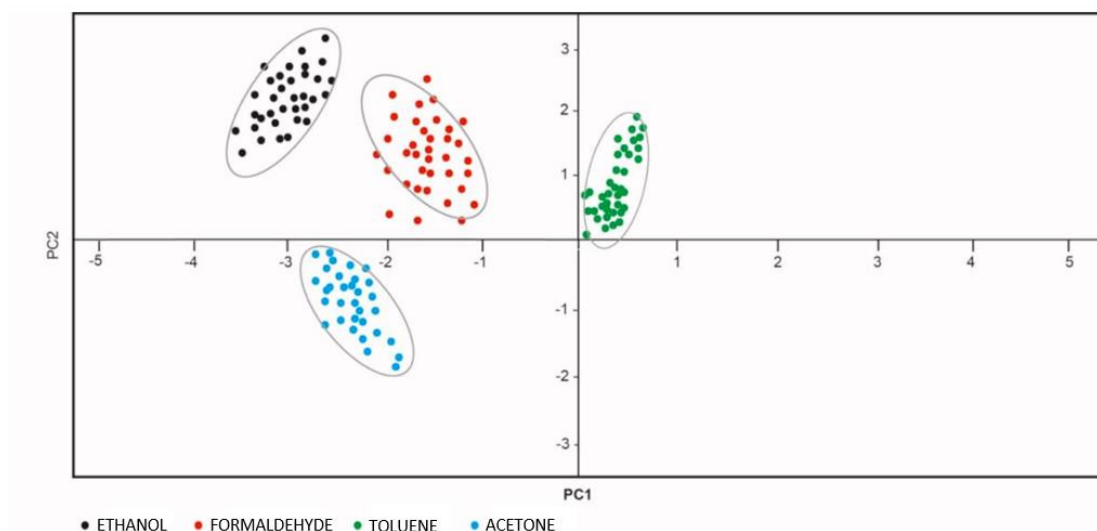


Figure 4.38. Principal component analysis result of an average of thirty determinations of (10 ppm) Ethanol, Formaldehyde, Toluene, and Acetone from the integrated instrument.

Figure 4.39 shows the Principal component analysis result of an average of thirty determinations of Ethanol, Formaldehyde, Toluene and Acetone obtained from the integrated instrument at 0.5 ppm. It is clearly seen that ethanol and formaldehyde do not show aggregation tendency. This can be attributed to the fact that the intensity of ethanol and formaldehyde characteristic peaks is not sufficiently strengthened on the nanoparticle decorated sensor surface. On the other hand, aggregation and a significant correlation were observed in acetone and toluene, albeit partial. The device, which allows for the selective determination of acetone at 500 ppb level, did not show the same performance for other VOCs.

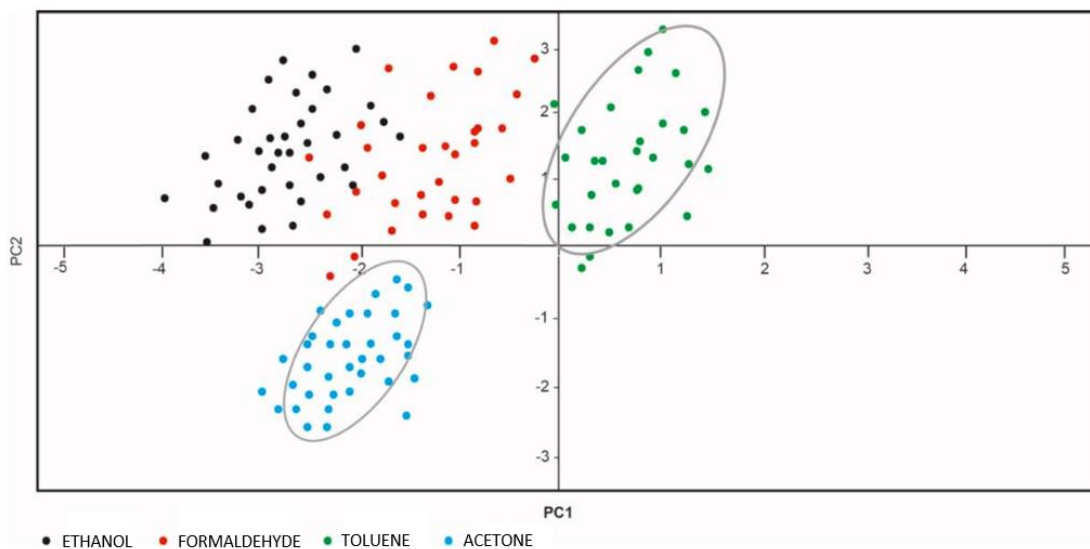


Figure 4.39. Principal component analysis result of an average of thirty determinations of Ethanol, Formaldehyde, Toluene and Acetone obtained from the integrated instrument at 0.5 ppm

CHAPTER 5

CONCLUSION

This thesis focuses on two-dimensional material, the use of graphene as a field-effect transistor, and its use in biological applications. For experimental studies, a sensor platform was created by synthesizing monolayer, bilayer and multilayer graphene films by CVD and epitaxial growth method and transferring them onto glass substrates, surface functionalization and surface and electrical measurements were made to determine the response characteristics of gas molecules and lipid molecules. In addition to this work, the determination of volatile organic compounds harmful to human health, such as ethanol and methanol, was selectively and sensitively electrically characterized on graphene surfaces in different layers. Furthermore, using polymer nanofiber / carbon nanotube or poly (3,4-ethylenedioxythiophene) / gold and iron oxide metal particle hybrid bioelectronic interface, low concentrations of acetone and ethanol, which are present in human breath and can be a symptom of some diseases, were determined in a humid environment. The results of the experiments were summarized in following.

In Chapter 4.1, the lipid bilayer formation and pH sensitivity on the SiO₂ surface were electrically characterized using a graphene field-effect transistor sensor platform with a wrinkled and flat interface. The GFET structure formed by the 15 nm thick SiO₂ layer coated with the TE method on the graphene surface grown epitaxially on SiC and the 100 nm thick SiO₂ based GFET surface coated with PED differed both structurally and electrically. As a result of the surface characteristic measurements made with AFM, wrinkle structures of approximately 40 μm were observed on the surface of the GFET coated with TE, while a flat morphology was observed on the surface of the GFET coated with PED. This surface dynamics indicates that the wrinkling can be associated with the sudden relaxation of the TE grown SiO₂ thin film on the epitaxial graphene layer due to the compressive strain. Electrical conductivity measurements at different pH values (pH 5 to 9) were made in both wrinkled-interfaced and flat-interfaced GFET sensors. As a result of these measurements, H⁺ ions density decreases from 10⁻⁵ to 10⁻⁶, for the wrinkled surface, the maximum current changes were recorded as 199.5 μA while on the flat surface is 2.59 μA. Also, the conductivity of wrinkle surface is approximately 100 times higher than flat surface at 5V bias. Wrinkled surface GFETs showing that wrinkled

surface GFETs are 80 times responsive to pH change as compared to flat one. The sensing mechanism for H⁺ ions on SiO₂ surface relies on the electrostatic gating effects based on the Gouy-Chapman-Stern- Graham model. H⁺ ions in the solution interact with hydroxyl species (–OH) on SiO₂ dielectric surface and therefore different H⁺ concentrations can induce changes of the surface charge density on the dielectric. On the other hand, lipid detection and bilayer formation mechanism was explained into four step. In overall the bilayer formation, there is a 19 μA current change is observed on the flat surface while this value is 390 μA on the wrinkled surface. This dramatic difference reveals that the lipid binding of the wrinkle surface is 19 fold more sensitive than the flat surface. Based on the outcomes of these experiments, we anticipate that the wrinkled SiO₂ interfaced-GFET described here exhibits great potential as a sensing platform that mimics cell membranes. This platform shows promise for various innovative bioelectronics applications.

Selective and sensitive detection of ethanol and methanol based on graphene based sensor platform and their results was explained in detail in Chapter 4.2. Single layer (SLG), bi-layer (BLG) and multi-layer graphene (MLG) are used to fabricate chemiresistors and their surface characteristics and number of layers were characterized by SEM and Raman spectroscopy. Surface conductivity of SLG and BLG in atomic scale was performed with AFM in conductive mode. Both SLG and BLG surface are homogeneous with a narrow range of current density distribution centered on 2 nA/μm² and 135 nA/μm², respectively. The surface roughness of SLG and BLG was measured as approximately 0.5 nm/μm². Chemiresistor responses of three devices was performed upon exposure to 0.2 ppm -50 ppm of ethanol and methanol over 2000 seconds. Both VOCs yield a sheet resistance modulation of less than 100 mΩ after and prior MeOH/EtOH exposure. For SLG, significant and differential responses were not observed upon exposure of MeOH and EtOH due to SLG surface which was correlated to the surface population of molecules rather than their size and chemical properties. On the other hand, for BLG the favorable adsorption of MeOH as compared to EtOH. The reason for the larger response of MeOH compared to EtOH can be attributed to the intercalation of MeOH within the two layers of BLG. The measurements indicate that the response of BLG chemiresistors cannot be solely attributed to the adsorption of volatile organic compounds (VOCs) on the graphene surface. Instead, it suggests that the diffusion and intercalation of VOCs between the layers of graphene may also contribute to the chemiresistor response. Unlike SLG and BLG, significantly larger changes in sheet

resistance were observed in chemiresistors made of MLG for all tested concentrations of EtOH and MeOH. Based on the measurements and density functional theory (DFT) calculations, the high VOC absorption capacity observed in MLG can be attributed to its multi-layered, three-dimensional morphology, which provides a larger surface area for adsorption. In this study, we showed that the intercalation mechanism is crucial for the discrimination of MeOH due to its molecular size, which matches the interlayer distance of the graphene layers. This matching molecular size facilitates the intercalation process, distinguishing MeOH from other primary alcohols with larger molecular sizes. In addition to this, we performed the responses of the chemiresistors that we prepared to ethanol and methanol concentrations at 25 ppm in a humid environment. From the measurements, variation in humidity levels does not significantly influence the VOC responses. However, in CO₂ and air ambient, MLG shows selective response to methanol rather than CO₂ and air. All experimental results shows that by increasing the number of graphene layers, distinct differential responses were observed between MeOH and EtOH, confirming that the intercalation phenomenon allows for differentiation between these two volatile organic compounds. The layered morphology of graphene, combined with the increased surface area, facilitated the intercalation of MeOH and consequently enabled sensitive and selective detection of MeOH.

In Chapter 4.3, by forming polymer nanofiber (PVDF, PU, PCL and PLLCL) / CNT or PEDOT:PSS hybrid bioelectronic interface was produced, the electrical responses of the prepared sensors to certain concentrations of acetone, ethanol and hexane gases in a humid environment were investigated. Also, the increase in the response of sensors decorated with Au and Fe nanoparticles to these gases was performed. The surface morphologies of the nanofiber conductive polymers coated on PMMA substrate by electrospinning were measured with MWCNT and PEDOT:PSS, and the conductivity measurements at atomic scale were measured by AFM (c-AFM). In the c-AFM measurements, it was shown that the current value obtained from the PVDF nanofiber coated with MWCNT is approximately 10 times higher than the PEDOT:PSS surface. The prepared polymer nanofiber/MWCNT-PEDOT:PSS sensor platforms were exposed to acetone and ethanol gases at 0.5-100 ppm concentrations. As a result of the electrical measurements made, the PLLCL-MWCNT hybrid chemiresistor gave the highest current change against acetone and ethanol. The response of PLLCL sensor covered with MWCNT to ethanol gas is about 2 times compared to that coated with PEDOT:PSS, and therefore, its surface is decorated with Au and Fe nanoparticles to increase the response

performance of the PLLCL-MWCNT hybrid structure. Then, its reaction to acetone, ethanol and hexane gas in a humid environment was investigated. As a result of these measurements, the presence of Fe NPs in the configuration, ensures that the sensor operates unaffected by moisture, compared to the response observed in the absence of Fe NPs. This is possible due to the surface properties of the Fe NPs, which lead to the condensation of water molecules on themselves. It can be concluded that the PLLCL-MWCNT-Fe sensor platform was the least affected by humidity conditions and exhibited the smallest loss in performance.

To summarize, his thesis may serve towards uncovering the potential of graphene, which is a two-dimensional material, as a field-effect transistor in the determination of bio-membrane dynamics and in the differential determination of volatile organic compounds provides important advantages.

REFERENCES

- (1) Fenoy, G. E.; Marmisollé, W. A.; Knoll, W.; Azzaroni, O. Highly Sensitive Urine Glucose Detection with Graphene Field-Effect Transistors Functionalized with Electropolymerized Nanofilms. *Sensors & Diagnostics* **2022**, *1* (1), 139–148.
- (2) Hao, Z.; Huang, C.; Zhao, C.; Kospan, A.; Wang, Z.; Li, F.; Wang, H.; Zhao, X.; Pan, Y.; Liu, S. Ultrasensitive Graphene-Based Nanobiosensor for Rapid Detection of Hemoglobin in Undiluted Biofluids. *ACS Applied Bio Materials* **2022**, *5* (4), 1624–1632.
- (3) Schuck, A.; Kim, H. E.; Moreira, J. K.; Lora, P. S.; Kim, Y.-S. A Graphene-Based Enzymatic Biosensor Using a Common-Gate Field-Effect Transistor for l-Lactic Acid Detection in Blood Plasma Samples. *Sensors* **2021**, *21* (5), 1852.
- (4) Barik, M. A.; Sarma, M. K.; Sarkar, C. R.; Dutta, J. C. Highly Sensitive Potassium-Doped Polypyrrole/Carbon Nanotube-Based Enzyme Field Effect Transistor (ENFET) for Cholesterol Detection. *Applied biochemistry and biotechnology* **2014**, *174*, 1104–1114.
- (5) Fenoy, G. E.; Marmisollé, W. A.; Azzaroni, O.; Knoll, W. Acetylcholine Biosensor Based on the Electrochemical Functionalization of Graphene Field-Effect Transistors. *Biosensors and Bioelectronics* **2020**, *148*, 111796.
- (6) Ren, Y.; Zhu, C.; Cai, W.; Li, H.; Ji, H.; Kholmanov, I.; Wu, Y.; Piner, R. D.; Ruoff, R. S. Detection of Sulfur Dioxide Gas with Graphene Field Effect Transistor. *Applied Physics Letters* **2012**, *100* (16), 163114.
- (7) Rashid, M. H.; Koel, A.; Rang, T. Simulations of Graphene Nanoribbon Field Effect Transistor for the Detection of Propane and Butane Gases: A First Principles Study. *Nanomaterials* **2020**, *10* (1), 98.
- (8) Ganguli, A.; Faramarzi, V.; Mostafa, A.; Hwang, M. T.; You, S.; Bashir, R. High Sensitivity Graphene Field Effect Transistor-Based Detection of DNA Amplification. *Advanced Functional Materials* **2020**, *30* (28), 2001031.
- (9) Ohno, Y.; Okamoto, S.; Maehashi, K.; Matsumoto, K. Direct Electrical Detection of DNA Hybridization Based on Electrolyte-Gated Graphene Field-Effect Transistor. *Japanese Journal of Applied Physics* **2013**, *52* (11R), 110107.
- (10) Perumal, J.; Wang, Y.; Attia, A. B. E.; Dinish, U. S.; Olivo, M. Towards a Point-of-Care SERS Sensor for Biomedical and Agri-Food Analysis Applications: A Review of Recent Advancements. *Nanoscale* **2021**, *13* (2), 553–580.
- (11) Ohno, Y.; Maehashi, K.; Yamashiro, Y.; Matsumoto, K. Electrolyte-Gated Graphene Field-Effect Transistors for Detecting PH and Protein Adsorption. *Nano letters* **2009**, *9* (9), 3318–3322.

- (12) Kanai, Y.; Ohmuro-Matsuyama, Y.; Tanioku, M.; Ushiba, S.; Ono, T.; Inoue, K.; Kitaguchi, T.; Kimura, M.; Ueda, H.; Matsumoto, K. Graphene Field Effect Transistor-Based Immunosensor for Ultrasensitive Noncompetitive Detection of Small Antigens. *ACS sensors* **2020**, *5* (1), 24–28.
- (13) Lee, H.; Paeng, K.; Kim, I. S. A Review of Doping Modulation in Graphene. *Synthetic Metals* **2018**, *244*, 36–47.
- (14) Alexander-Webber, J. A.; Sagade, A. A.; Aria, A. I.; Van Veldhoven, Z. A.; Braeuninger-Weimer, P.; Wang, R.; Cabrero-Vilatela, A.; Martin, M.-B.; Sui, J.; Connolly, M. R. Encapsulation of Graphene Transistors and Vertical Device Integration by Interface Engineering with Atomic Layer Deposited Oxide. *2D Materials* **2016**, *4* (1), 011008.
- (15) Kalkan, S. B.; Aydın, H.; Özkendir, D.; Çelebi, C. The Effect of Adsorbates on the Electrical Stability of Graphene Studied by Transient Photocurrent Spectroscopy. *Applied Physics Letters* **2018**, *112* (1), 013103.
- (16) Puglisi, D.; Eriksson, J.; Bur, C.; Schuetze, A.; Lloyd Spetz, A.; Andersson, M. Catalytic Metal-Gate Field Effect Transistors Based on SiC for Indoor Air Quality Control. *Journal of Sensors and Sensor Systems* **2015**, *4* (1), 1–8.
- (17) Rahimi, R.; Solimannejad, M. B3O3 Monolayer with Dual Application in Sensing of COVID-19 Biomarkers and Drug Delivery for Treatment Purposes: A Periodic DFT Study. *Journal of Molecular Liquids* **2022**, *354*, 118855.
- (18) Surya, S. G.; Raval, H. N.; Ahmad, R.; Sonar, P.; Salama, K. N.; Rao, V. R. Organic Field Effect Transistors (OFETs) in Environmental Sensing and Health Monitoring: A Review. *TrAC Trends in Analytical Chemistry* **2019**, *111*, 27–36.
- (19) Rungreunghanapol, T.; Homma, C.; Akagi, K.; Tanaka, M.; Kikuchi, J.; Tomizawa, H.; Sugizaki, Y.; Isobayashi, A.; Hayamizu, Y.; Okochi, M. Volatile Organic Compound Detection by Graphene Field-Effect Transistors Functionalized with Fly Olfactory Receptor Mimetic Peptides. *Analytical Chemistry* **2023**, *95* (9), 4556–4563.
- (20) Bur, C.; Bastuck, M.; Puglisi, D.; Schütze, A.; Spetz, A. L.; Andersson, M. Discrimination and Quantification of Volatile Organic Compounds in the Ppb-Range with Gas Sensitive Sic-Field Effect Transistors. *Procedia Engineering* **2014**, *87*, 604–607.
- (21) Konvalina, G.; Haick, H. Sensors for Breath Testing: From Nanomaterials to Comprehensive Disease Detection. *Accounts of chemical research* **2014**, *47* (1), 66–76.
- (22) Isidorov, V. A.; Zenkevich, I. G.; Ioffe, B. V. Volatile Organic Compounds in the Atmosphere of Forests. *Atmospheric Environment (1967)* **1985**, *19* (1), 1–8.
- (23) Islam, M.; Shahin Ahmed, K.; Karim, R.; Nath, B. D.; Prosad Moulick, S.; Islam, R.; Mahmudul Hassan, S. M.; Hossain, H.; Moniruzzaman, M.; Jahan, M. S. Alcohol-Based Hand Sanitizers amid COVID-19: Chemical Formulation, Analysis, Safety. *ChemistrySelect* **2022**, *7* (45), e202203290.

- (24) Reddy, C. S.; Murali, G.; Reddy, A. S.; Park, S.; In, I. GO Incorporated SnO₂ Nanotubes as Fast Response Sensors for Ethanol Vapor in Different Atmospheres. *Journal of Alloys and Compounds* **2020**, *813*, 152251.
- (25) Liu, H.; Chu, Y.; Liu, Y.; Hayasaka, T.; Joshi, N.; Cui, Y.; Wang, X.; You, Z.; Lin, L. Selective Sensing of Chemical Vapors Using Phase Spectra Detection on CVD Graphene Fet. In *2018 IEEE Micro Electro Mechanical Systems (MEMS)*; IEEE, 2018; pp 210–213.
- (26) Paul, R. K.; Badhulika, S.; Saucedo, N. M.; Mulchandani, A. Graphene Nanomesh as Highly Sensitive Chemiresistor Gas Sensor. *Analytical chemistry* **2012**, *84* (19), 8171–8178.
- (27) Novoselov, K. S.; Fal'ko, V. I.; Colombo, L.; Gellert, P. R.; Schwab, M. G.; Kim, K. A Roadmap for Graphene. *nature* **2012**, *490* (7419), 192–200.
- (28) Barnard, A. S.; Snook, I. K. Thermal Stability of Graphene Edge Structure and Graphene Nanoflakes. *The Journal of chemical physics* **2008**, *128* (9), 094707.
- (29) Du, X.; Skachko, I.; Barker, A.; Andrei, E. Y. Approaching Ballistic Transport in Suspended Graphene. *Nature nanotechnology* **2008**, *3* (8), 491–495.
- (30) Afanasov, I. M.; Morozov, V. A.; Kepman, A. V.; Ionov, S. G.; Seleznev, A. N.; Van Tendeloo, G.; Avdeev, V. V. Preparation, Electrical and Thermal Properties of New Exfoliated Graphite-Based Composites. *Carbon* **2009**, *47* (1), 263–270.
- (31) Ahmad, S. Carbon Nanostructures Fullerenes and Carbon Nanotubes. *IETE Technical Review* **1999**, *16* (3–4), 297–310.
- (32) Karthik, P. S.; Himaja, A. L.; Singh, S. P. Carbon-Allotropes: Synthesis Methods, Applications and Future Perspectives. *Carbon letters* **2014**, *15* (4), 219–237.
- (33) Murali, R.; Yang, Y.; Brenner, K.; Beck, T.; Meindl, J. D. Breakdown Current Density of Graphene Nanoribbons. *Applied Physics Letters* **2009**, *94* (24), 243114.
- (34) Calado, V. E.; Zhu, S.-E.; Goswami, S.; Xu, Q.; Watanabe, K.; Taniguchi, T.; Janssen, G. C.; Vandersypen, L. M. K. Ballistic Transport in Graphene Grown by Chemical Vapor Deposition. *Applied Physics Letters* **2014**, *104* (2), 023103.
- (35) Choi, W.; Lee, J. *Graphene: Synthesis and Applications*; CRC press, 2011.
- (36) Balandin, A. A.; Ghosh, S.; Bao, W.; Calizo, I.; Teweldebrhan, D.; Miao, F.; Lau, C. N. Superior Thermal Conductivity of Single-Layer Graphene. *Nano letters* **2008**, *8* (3), 902–907.
- (37) Gan, T.; Hu, S. Electrochemical Sensors Based on Graphene Materials. *Microchimica Acta* **2011**, *175*, 1–19.

- (38) Lakshmanan, R.; Maulik, N. Graphene-Based Drug Delivery Systems in Tissue Engineering and Nanomedicine. *Canadian journal of physiology and pharmacology* **2018**, *96* (9), 869–878.
- (39) Rhouma, M. B. Modeling and Simulation of Composite Plasmonic Structures Based on Graphene and Metals. PhD Thesis, Université Clermont Auvergne, 2021.
- (40) Sheehy, D. E.; Schmalian, J. Optical Transparency of Graphene as Determined by the Fine-Structure Constant. *Physical Review B* **2009**, *80* (19), 193411.
- (41) Kim, M.-S.; Kim, M.; Son, S.; Cho, S.-Y.; Lee, S.; Won, D.-K.; Ryu, J.; Bae, I.; Kim, H.-M.; Kim, K.-B. Sheet Resistance Analysis of Interface-Engineered Multilayer Graphene: Mobility versus Sheet Carrier Concentration. *ACS applied materials & interfaces* **2020**, *12* (27), 30932–30940.
- (42) Bolotin, K. I.; Sikes, K. J.; Jiang, Z.; Klima, M.; Fudenberg, G.; Hone, J.; Kim, P.; Stormer, H. L. Ultrahigh Electron Mobility in Suspended Graphene. *Solid state communications* **2008**, *146* (9–10), 351–355.
- (43) McIver, J. W.; Schulte, B.; Stein, F.-U.; Matsuyama, T.; Jotzu, G.; Meier, G.; Cavalleri, A. Light-Induced Anomalous Hall Effect in Graphene. *Nature physics* **2020**, *16* (1), 38–41.
- (44) Crosser, M. S.; Brown, M. A.; McEuen, P. L.; Minot, E. D. Determination of the Thermal Noise Limit of Graphene Biotransistors. *Nano Letters* **2015**, *15* (8), 5404–5407.
- (45) Jo, G.; Choe, M.; Lee, S.; Park, W.; Kahng, Y. H.; Lee, T. The Application of Graphene as Electrodes in Electrical and Optical Devices. *Nanotechnology* **2012**, *23* (11), 112001.
- (46) Das, T.; Sharma, B. K.; Katiyar, A. K.; Ahn, J.-H. Graphene-Based Flexible and Wearable Electronics. *Journal of Semiconductors* **2018**, *39* (1), 011007.
- (47) Neto, A. C.; Guinea, F.; Peres, N. M.; Novoselov, K. S.; Geim, A. K. The Electronic Properties of Graphene. *Reviews of modern physics* **2009**, *81* (1), 109.
- (48) Choi, J. Y.; Kang, W.; Kang, B.; Cha, W.; Son, S. K.; Yoon, Y.; Kim, H.; Kang, Y.; Ko, M. J.; Son, H. J. High Performance of Low Band Gap Polymer-Based Ambipolar Transistor Using Single-Layer Graphene Electrodes. *ACS Applied Materials & Interfaces* **2015**, *7* (10), 6002–6012.
- (49) Sakhaee-Pour, A. Elastic Properties of Single-Layered Graphene Sheet. *Solid State Communications* **2009**, *149* (1–2), 91–95.
- (50) Novoselov, K. S.; McCann, E.; Morozov, S. V.; Fal’ko, V. I.; Katsnelson, M. I.; Zeitler, U.; Jiang, D.; Schedin, F.; Geim, A. K. Unconventional Quantum Hall Effect and Berry’s Phase of 2π in Bilayer Graphene. *Nature physics* **2006**, *2* (3), 177–180.

- (51) Lang, B. A LEED Study of the Deposition of Carbon on Platinum Crystal Surfaces. *Surface Science* **1975**, *53* (1), 317–329.
- (52) Novoselov, K. S.; Geim, A. K.; Morozov, S. V.; Jiang, D.; Zhang, Y.; Dubonos, S. V.; Grigorieva, I. V.; Firsov, A. A. Electric Field Effect in Atomically Thin Carbon Films. *science* **2004**, *306* (5696), 666–669.
- (53) Wu, Z.-S.; Ren, W.; Gao, L.; Liu, B.; Jiang, C.; Cheng, H.-M. Synthesis of High-Quality Graphene with a Pre-Determined Number of Layers. *Carbon* **2009**, *47* (2), 493–499.
- (54) Somani, P. R.; Somani, S. P.; Umeno, M. Planer Nano-Graphenes from Camphor by CVD. *Chemical Physics Letters* **2006**, *430* (1–3), 56–59.
- (55) Saeed, M.; Alshammari, Y.; Majeed, S. A.; Al-Nasrallah, E. Chemical Vapour Deposition of Graphene—Synthesis, Characterisation, and Applications: A Review. *Molecules* **2020**, *25* (17), 3856.
- (56) Huang, M.; Wang, C.; Quan, L.; Nguyen, T. H.-Y.; Zhang, H.; Jiang, Y.; Byun, G.; Ruoff, R. S. CVD Growth of Porous Graphene Foam in Film Form. *Matter* **2020**, *3* (2), 487–497.
- (57) Drieschner, S.; Weber, M.; Wohlketter, J.; Vieten, J.; Makrygiannis, E.; Blaschke, B. M.; Morandi, V.; Colombo, L.; Bonaccorso, F.; Garrido, J. A. High Surface Area Graphene Foams by Chemical Vapor Deposition. *2D Materials* **2016**, *3* (4), 045013.
- (58) Chen, G.; Liu, Y.; Liu, F.; Zhang, X. Fabrication of Three-Dimensional Graphene Foam with High Electrical Conductivity and Large Adsorption Capability. *Applied Surface Science* **2014**, *311*, 808–815.
- (59) Zhang, W.; Sun, Y.; Liu, T.; Li, D.; Hou, C.; Gao, L.; Liu, Y. Preparation of Graphene Foam with High Performance by Modified Self-Assembly Method. *Applied Physics A* **2016**, *122*, 1–9.
- (60) Chen, Z.; Ren, W.; Gao, L.; Liu, B.; Pei, S.; Cheng, H.-M. Three-Dimensional Flexible and Conductive Interconnected Graphene Networks Grown by Chemical Vapour Deposition. *Nature materials* **2011**, *10* (6), 424–428.
- (61) Reddy, S. K.; Ferry, D. B.; Misra, A. Highly Compressible Behavior of Polymer Mediated Three-Dimensional Network of Graphene Foam. *RSC Advances* **2014**, *4* (91), 50074–50080.
- (62) Liu, Z.; Wang, B.; Wei, S.; Huang, W.; Wang, Y.; Liang, Y. Effect of Different Reducing Agents on the Microwave Absorption Properties of Graphene Foam. *Materials Letters* **2023**, *337*, 133950.
- (63) Barzegar, F.; Bello, A.; Fashedemi, O. O.; Dangbegnon, J. K.; Momodu, D. Y.; Taghizadeh, F.; Manyala, N. Synthesis of 3D Porous Carbon Based on Cheap Polymers

and Graphene Foam for High-Performance Electrochemical Capacitors. *Electrochimica Acta* **2015**, *180*, 442–450.

(64) Hu, G.; Xu, C.; Sun, Z.; Wang, S.; Cheng, H.-M.; Li, F.; Ren, W. 3D Graphene-Foam-Reduced-Graphene-Oxide Hybrid Nested Hierarchical Networks for High-Performance Li-S Batteries. *Advanced materials* **2016**, *28* (8), 1603–1609.

(65) Bardeen, J.; Brattain, W. H. The Transistor, a Semi-Conductor Triode. *Physical Review* **1948**, *74* (2), 230.

(66) Das, S.; Dubey, M.; Roelofs, A. High Gain, Low Noise, Fully Complementary Logic Inverter Based on Bi-Layer WSe₂ Field Effect Transistors. *Applied Physics Letters* **2014**, *105* (8), 083511.

(67) Nazir, G.; Rehman, A.; Park, S.-J. Energy-Efficient Tunneling Field-Effect Transistors for Low-Power Device Applications: Challenges and Opportunities. *ACS Applied Materials & Interfaces* **2020**, *12* (42), 47127–47163.

(68) Xi, F.; Han, Y.; Grenmyr, A.; Grützmacher, D.; Zhao, Q.-T. Four-Terminal Ferroelectric Schottky Barrier Field Effect Transistors as Artificial Synapses for Neuromorphic Applications. *IEEE Journal of the Electron Devices Society* **2022**, *10*, 569–574.

(69) Radeka, V. The Field-Effect Transistor-Its Characteristics and Applications. *IEEE Transactions on Nuclear Science* **1964**, *11* (3), 358–364.

(70) Liu, S.; Guo, X. Carbon Nanomaterials Field-Effect-Transistor-Based Biosensors. *NPG Asia Materials* **2012**, *4* (8), e23–e23.

(71) Svintsov, D.; Vyurkov, V.; Orlikovsky, A.; Ryzhii, V.; Otsuji, T. All-Graphene Field-Effect Transistor Based on Lateral Tunnelling. *Journal of Physics D: Applied Physics* **2014**, *47* (9), 094002.

(72) Wu, Y. Q.; Ye, P. D.; Capano, M. A.; Xuan, Y.; Sui, Y.; Qi, M.; Cooper, J. A.; Shen, T.; Pandey, D.; Prakash, G. Top-Gated Graphene Field-Effect-Transistors Formed by Decomposition of SiC. *Applied Physics Letters* **2008**, *92* (9), 092102.

(73) Meric, I.; Han, M. Y.; Young, A. F.; Ozyilmaz, B.; Kim, P.; Shepard, K. L. Current Saturation in Zero-Bandgap, Top-Gated Graphene Field-Effect Transistors. *Nature nanotechnology* **2008**, *3* (11), 654–659.

(74) He, R. X.; Lin, P.; Liu, Z. K.; Zhu, H. W.; Zhao, X. Z.; Chan, H. L.; Yan, F. Solution-Gated Graphene Field Effect Transistors Integrated in Microfluidic Systems and Used for Flow Velocity Detection. *Nano letters* **2012**, *12* (3), 1404–1409.

(75) Bergveld, P. Development of an Ion-Sensitive Solid-State Device for Neurophysiological Measurements. *IEEE Transactions on biomedical engineering* **1970**, No. 1, 70–71.

- (76) Reiner-Rozman, C.; Larisika, M.; Nowak, C.; Knoll, W. Graphene-Based Liquid-Gated Field Effect Transistor for Biosensing: Theory and Experiments. *Biosensors and Bioelectronics* **2015**, *70*, 21–27.
- (77) Reddy, D.; Register, L. F.; Carpenter, G. D.; Banerjee, S. K. Graphene Field-Effect Transistors. *Journal of Physics D: Applied Physics* **2011**, *44* (31), 313001.
- (78) Lu, C.-C.; Lin, Y.-C.; Yeh, C.-H.; Huang, J.-C.; Chiu, P.-W. High Mobility Flexible Graphene Field-Effect Transistors with Self-Healing Gate Dielectrics. *ACS nano* **2012**, *6* (5), 4469–4474.
- (79) Ohno, Y.; Maehashi, K.; Matsumoto, K. Chemical and Biosensing Applications Based on Graphene Field-Effect Transistors. In *Physics and Applications of Graphene-Experiments*; IntechOpen, 2011.
- (80) Fujimoto, T.; Awaga, K. Electric-Double-Layer Field-Effect Transistors with Ionic Liquids. *Physical Chemistry Chemical Physics* **2013**, *15* (23), 8983–9006.
- (81) Kontogeorgis, G. M.; Maribo-Mogensen, B.; Thomsen, K. The Debye-Hückel Theory and Its Importance in Modeling Electrolyte Solutions. *Fluid Phase Equilibria* **2018**, *462*, 130–152.
- (82) Ligor, M.; Ligor, T.; Bajtarevic, A.; Ager, C.; Pienz, M.; Klieber, M.; Denz, H.; Fiegl, M.; Hilbe, W.; Weiss, W. Determination of Volatile Organic Compounds in Exhaled Breath of Patients with Lung Cancer Using Solid Phase Microextraction and Gas Chromatography Mass Spectrometry. *Clinical chemistry and laboratory medicine* **2009**, *47* (5), 550–560.
- (83) Schedin, F.; Geim, A. K.; Morozov, S. V.; Hill, E. W.; Blake, P.; Katsnelson, M. I.; Novoselov, K. S. Detection of Individual Gas Molecules Adsorbed on Graphene. *Nature materials* **2007**, *6* (9), 652–655.
- (84) Ohno, Y.; Maehashi, K.; Matsumoto, K. Label-Free Biosensors Based on Aptamer-Modified Graphene Field-Effect Transistors. *Journal of the American Chemical Society* **2010**, *132* (51), 18012–18013.
- (85) Gautam, M.; Jayatissa, A. H. Graphene Based Field Effect Transistor for the Detection of Ammonia. *Journal of Applied Physics* **2012**, *112* (6), 064304.
- (86) Varghese, S. S.; Varghese, S. H.; Swaminathan, S.; Singh, K. K.; Mittal, V. Two-Dimensional Materials for Sensing: Graphene and Beyond. *Electronics* **2015**, *4* (3), 651–687.
- (87) Fu, W.; Feng, L.; Mayer, D.; Panaitov, G.; Kireev, D.; Offenhäusser, A.; Krause, H.-J. Electrolyte-Gated Graphene Ambipolar Frequency Multipliers for Biochemical Sensing. *Nano letters* **2016**, *16* (4), 2295–2300.
- (88) Kim, C.-H.; Yoo, S.-W.; Nam, D.-W.; Seo, S.; Lee, J.-H. Effect of Temperature and Humidity on $\{NO\}_2$ and $\{NH\}_3$ Gas

Sensitivity of Bottom-Gate Graphene FETs Prepared by ICP-CVD. *IEEE electron device letters* **2012**, *33* (7), 1084–1086.

(89) Hwang, I.-S.; Choi, J.-K.; Woo, H.-S.; Kim, S.-J.; Jung, S.-Y.; Seong, T.-Y.; Kim, I.-D.; Lee, J.-H. Facile Control of C₂H₅OH Sensing Characteristics by Decorating Discrete Ag Nanoclusters on SnO₂ Nanowire Networks. *ACS applied materials & interfaces* **2011**, *3* (8), 3140–3145.

(90) Mattioli, I. A.; Hassan, A.; Sanches, N. M.; Vieira, N. C.; Crespilho, F. N. Highly Sensitive Interfaces of Graphene Electrical-Electrochemical Vertical Devices for on Drop Atto-Molar DNA Detection. *Biosensors and Bioelectronics* **2021**, *175*, 112851.

(91) Campos, R.; Borme, J.; Guerreiro, J. R.; Machado Jr, G.; Cerqueira, M. F.; Petrovykh, D. Y.; Alpuim, P. Attomolar Label-Free Detection of DNA Hybridization with Electrolyte-Gated Graphene Field-Effect Transistors. *ACS sensors* **2019**, *4* (2), 286–293.

(92) Chee, L. H.; Kumar, P.; Kang, C. H.; Burhanudin, Z. A. DNA/AuNP-Graphene Back-Gated Field Effect Transistor as a Biosensor for Lead (II) Ion Detection. In *2017 IEEE regional symposium on micro and nanoelectronics (RSM)*; IEEE, 2017; pp 127–130.

(93) Lei, Y.-M.; Xiao, M.-M.; Li, Y.-T.; Xu, L.; Zhang, H.; Zhang, Z.-Y.; Zhang, G.-J. Detection of Heart Failure-Related Biomarker in Whole Blood with Graphene Field Effect Transistor Biosensor. *Biosensors and Bioelectronics* **2017**, *91*, 1–7.

(94) Norimatsu, W.; Kusunoki, M. Epitaxial Graphene on SiC {0001}: Advances and Perspectives. *Physical Chemistry Chemical Physics* **2014**, *16* (8), 3501–3511.

(95) Il'ves, V. G.; Zuev, M. G.; Sokovnin, S. Y. Properties of Silicon Dioxide Amorphous Nanopowder Produced by Pulsed Electron Beam Evaporation. *Journal of Nanotechnology* **2015**, *2015*.

(96) Frenot, A.; Chronakis, I. S. Polymer Nanofibers Assembled by Electrospinning. *Current opinion in colloid & interface science* **2003**, *8* (1), 64–75.

(97) Lau, C. H.; Cervini, R.; Clarke, S. R.; Markovic, M. G.; Matison, J. G.; Hawkins, S. C.; Huynh, C. P.; Simon, G. P. The Effect of Functionalization on Structure and Electrical Conductivity of Multi-Walled Carbon Nanotubes. *Journal of Nanoparticle Research* **2008**, *10*, 77–88.

(98) Turkevich, J.; Stevenson, P. C.; Hillier, J. A Study of the Nucleation and Growth Processes in the Synthesis of Colloidal Gold. *Discussions of the Faraday Society* **1951**, *11*, 55–75.

(99) Dresselhaus, M. S.; Jorio, A.; Hofmann, M.; Dresselhaus, G.; Saito, R. Perspectives on Carbon Nanotubes and Graphene Raman Spectroscopy. *Nano letters* **2010**, *10* (3), 751–758.

- (100) Dresselhaus, G.; Dresselhaus, M. S.; Saito, R. *Physical Properties of Carbon Nanotubes*; World scientific, 1998.
- (101) Ferrari, A. C.; Meyer, J. C.; Scardaci, V.; Casiraghi, C.; Lazzeri, M.; Mauri, F.; Piscanec, S.; Jiang, D.; Novoselov, K. S.; Roth, S. The Raman Fingerprint of Graphene. *arXiv preprint cond-mat/0606284* **2006**.
- (102) Di Bartolomeo, A. Graphene Schottky Diodes: An Experimental Review of the Rectifying Graphene/Semiconductor Heterojunction. *Physics Reports* **2016**, *606*, 1–58.
- (103) Yoon, D.; Son, Y.-W.; Cheong, H. Negative Thermal Expansion Coefficient of Graphene Measured by Raman Spectroscopy. *Nano letters* **2011**, *11* (8), 3227–3231.
- (104) Tsou, C.; Huang, Y.-S.; Li, H.-C.; Lai, T.-H. Determination of Thermal Expansion Coefficient of Thermal Oxide. *Sensors Mater* **2005**, *17* (8), 441–451.
- (105) Akins, J. A.; Ahrens, T. J. Dynamic Compression of SiO₂: A New Interpretation. *Geophysical Research Letters* **2002**, *29* (10), 31–1.
- (106) Li, Z.; Bradt, R. C. Thermal Expansion and Thermal Expansion Anisotropy of SiC Polytypes. *Journal of the American Ceramic Society* **1987**, *70* (7), 445–448.
- (107) Ekimov, E. A.; Gierlotka, S.; Gromnitskaya, E. L.; Kozubowski, J. A.; Palosz, B.; Lojkowski, W.; Naletov, A. M. Mechanical Properties and Microstructure of Diamond–SiC Nanocomposites. *Inorganic materials* **2002**, *38*, 1117–1122.
- (108) Hamilton, R. L.; Guo, L. S. French Pressure Cell Liposomes: Preparation, Properties, and Potential. In *Liposome Technology*; CRC Press, 2019; pp 37–49.
- (109) Mayer, L. D.; Bally, M. B.; Hope, M. J.; Cullis, P. R. Techniques for Encapsulating Bioactive Agents into Liposomes. *Chemistry and physics of lipids* **1986**, *40* (2–4), 333–345.
- (110) Song, H.; Geng, H.; Ruan, J.; Wang, K.; Bao, C.; Wang, J.; Peng, X.; Zhang, X.; Cui, D. Development of Polysorbate 80/Phospholipid Mixed Micellar Formation for Docetaxel and Assessment of Its in Vivo Distribution in Animal Models. *Nanoscale research letters* **2011**, *6*, 1–12.
- (111) Oldham, K. B. A Gouy–Chapman–Stern Model of the Double Layer at a (Metal)/(Ionic Liquid) Interface. *Journal of Electroanalytical Chemistry* **2008**, *613* (2), 131–138.
- (112) Blaschke, B. M.; Böhm, P.; Drieschner, S.; Nickel, B.; Garrido, J. A. Lipid Monolayer Formation and Lipid Exchange Monitored by a Graphene Field-Effect Transistor. *Langmuir* **2018**, *34* (14), 4224–4233.
- (113) Cho, N.-J.; Frank, C. W.; Kasemo, B.; Höök, F. Quartz Crystal Microbalance with Dissipation Monitoring of Supported Lipid Bilayers on Various Substrates. *Nature protocols* **2010**, *5* (6), 1096–1106.

- (114) Lichtenberg, D.; Ahyayauch, H.; Goñi, F. M. The Mechanism of Detergent Solubilization of Lipid Bilayers. *Biophysical journal* **2013**, *105* (2), 289–299.
- (115) Zhang, X.; Gan, Z.; Wang, Y.; Tang, X.; Li, G.; Liang, H. Effect of Chemical Cleaning on Nanofiltration Process in Treating Surface Water. *Journal of Water Process Engineering* **2022**, *50*, 103271.
- (116) Novikov, S.; Lebedeva, N.; Satrapinski, A.; Walden, J.; Davydov, V.; Lebedev, A. Graphene Based Sensor for Environmental Monitoring of NO₂. *Sensors and Actuators B: Chemical* **2016**, *236*, 1054–1060.
- (117) Singh, E.; Meyyappan, M.; Nalwa, H. S. Flexible Graphene-Based Wearable Gas and Chemical Sensors. *ACS applied materials & interfaces* **2017**, *9* (40), 34544–34586.
- (118) Dong, X.; Wang, P.; Fang, W.; Su, C.-Y.; Chen, Y.-H.; Li, L.-J.; Huang, W.; Chen, P. Growth of Large-Sized Graphene Thin-Films by Liquid Precursor-Based Chemical Vapor Deposition under Atmospheric Pressure. *Carbon* **2011**, *49* (11), 3672–3678.
- (119) Warburton, P. R.; Pagano, M. P.; Hoover, R.; Logman, M.; Crytzer, K.; Warburton, Y. J. Amperometric Gas Sensor Response Times. *Analytical chemistry* **1998**, *70* (5), 998–1006.
- (120) Choi, J. H.; Lee, J.; Byeon, M.; Hong, T. E.; Park, H.; Lee, C. Y. Graphene-Based Gas Sensors with High Sensitivity and Minimal Sensor-to-Sensor Variation. *ACS Applied Nano Materials* **2020**, *3* (3), 2257–2265.
- (121) Lv, C.; Hu, C.; Luo, J.; Liu, S.; Qiao, Y.; Zhang, Z.; Song, J.; Shi, Y.; Cai, J.; Watanabe, A. Recent Advances in Graphene-Based Humidity Sensors. *Nanomaterials* **2019**, *9* (3), 422.
- (122) Phasukom, K.; Prissanaroon-Ouajai, W.; Sirivat, A. A Highly Responsive Methanol Sensor Based on Graphene Oxide/Polyindole Composites. *RSC advances* **2020**, *10* (26), 15206–15220.
- (123) Leenaerts, O.; Partoens, B.; Peeters, F. M. Adsorption of H₂O, NH₃, CO, N₂O, and NO on Graphene: A First-Principles Study. *Physical Review B* **2008**, *77* (12), 125416.
- (124) Bader, R. F. W.; Henneker, W. H.; Cade, P. E. Molecular Charge Distributions and Chemical Binding. *The Journal of Chemical Physics* **1967**, *46* (9), 3341–3363.
- (125) Vanstraelen, S.; Jones, D. R.; Rocco, G. Breathprinting Analysis and Biomimetic Sensor Technology to Detect Lung Cancer. *The Journal of Thoracic and Cardiovascular Surgery* **2023**.
- (126) Gashimova, E. M.; Temerdashev, A. Z.; Porkhanov, V. A.; Polyakov, I. S.; Perunov, D. V. Comparative Analysis of Pre-and Post-Surgery Exhaled Breath Profiles

of Volatile Organic Compounds of Patients with Lung Cancer and Benign Tumors. *Journal of Analytical Chemistry* **2022**, 77 (12), 1547–1552.

(127) Shang, G.; Dinh, D.; Mercer, T.; Yan, S.; Wang, S.; Malaei, B.; Luo, J.; Lu, S.; Zhong, C.-J. Chemiresistive Sensor Array with Nanostructured Interfaces for Detection of Human Breaths with Simulated Lung Cancer Breath VOCs. *ACS sensors* **2023**, 8 (3), 1328–1338.

(128) Dragonieri, S.; Scioscia, G.; Quaranta, V. N.; Carratu, P.; Venuti, M. P.; Falcone, M.; Carpagnano, G. E.; Barbaro, M. P. F.; Resta, O.; Lacedonia, D. Exhaled Volatile Organic Compounds Analysis by E-Nose Can Detect Idiopathic Pulmonary Fibrosis. *Journal of Breath Research* **2020**, 14 (4), 047101.

(129) Ratiu, I. A.; Ligor, T.; Bocos-Bintintan, V.; Mayhew, C. A.; Buszewski, B. Volatile Organic Compounds in Exhaled Breath as Fingerprints of Lung Cancer, Asthma and COPD. *Journal of clinical medicine* **2020**, 10 (1), 32.

(130) Suzuki, N.; Nakaoka, H.; Nakayama, Y.; Tsumura, K.; Takaguchi, K.; Takaya, K.; Eguchi, A.; Hanazato, M.; Todaka, E.; Mori, C. Association between Sum of Volatile Organic Compounds and Occurrence of Building-Related Symptoms in Humans: A Study in Real Full-Scale Laboratory Houses. *Science of the Total Environment* **2021**, 750, 141635.

(131) Gibbs, J. E. Essential Oils, Asthma, Thunderstorms, and Plant Gases: A Prospective Study of Respiratory Response to Ambient Biogenic Volatile Organic Compounds (BVOCs). *Journal of Asthma and Allergy* **2019**, 169–182.

(132) Guo, X.; Li, J.; Wang, F.; Zhang, J.-H.; Zhang, J.; Shi, Y.; Pan, L. Application of Conductive Polymer Hydrogels in Flexible Electronics. *Journal of Polymer Science* **2022**, 60 (18), 2635–2662.

(133) Wang, X.-X.; Yu, G.-F.; Zhang, J.; Yu, M.; Ramakrishna, S.; Long, Y.-Z. Conductive Polymer Ultrafine Fibers via Electrospinning: Preparation, Physical Properties and Applications. *Progress in Materials Science* **2021**, 115, 100704.

(134) Wang, Y.; Liu, A.; Han, Y.; Li, T. Sensors Based on Conductive Polymers and Their Composites: A Review. *Polymer International* **2020**, 69 (1), 7–17.

(135) Jin, C.; Suenaga, K.; Iijima, S. Plumbing Carbon Nanotubes. *Nature Nanotechnology* **2008**, 3 (1), 17–21.

(136) Sun, L.; Wang, X.; Wang, Y.; Zhang, Q. Roles of Carbon Nanotubes in Novel Energy Storage Devices. *Carbon* **2017**, 122, 462–474.

(137) Díaz, E.; Ordóñez, S.; Vega, A. Adsorption of Volatile Organic Compounds onto Carbon Nanotubes, Carbon Nanofibers, and High-Surface-Area Graphites. *Journal of colloid and interface science* **2007**, 305 (1), 7–16.

- (138) Malcolm, A.; Wright, S.; Syms, R. R.; Dash, N.; Schwab, M.-A.; Finlay, A. Miniature Mass Spectrometer Systems Based on a Microengineered Quadrupole Filter. *Analytical Chemistry* **2010**, *82* (5), 1751–1758.
- (139) Sakhthivel, M.; Weppner, W. A Portable Limiting Current Solid-State Electrochemical Diffusion Hole Type Hydrogen Sensor Device for Biomass Fuel Reactors: Engineering Aspect. *International journal of hydrogen energy* **2008**, *33* (2), 905–911.
- (140) Hübert, T.; Boon-Brett, L.; Black, G.; Banach, U. Hydrogen Sensors—a Review. *Sensors and Actuators B: Chemical* **2011**, *157* (2), 329–352.
- (141) Gong, K.; Xu, X.; Liu, Y.; Huang, W.; Liu, Q.; Huang, X.; Wei, S. Induced Electrical Polarization and Conductivity Homogenization via Internal Architectural Regulation in PC/PVDF/MWCNTs/PEDOT:PSS Transparent Conductive Films. *Polymer* **2022**, *254*, 125088. <https://doi.org/10.1016/j.polymer.2022.125088>.
- (142) Ahmad, Z.; Azman, A. W.; Buys, Y. F.; Sarifuddin, N. Mechanisms for Doped PEDOT: PSS Electrical Conductivity Improvement. *Materials Advances* **2021**, *2* (22), 7118–7138.
- (143) Stöcker, T.; Köhler, A.; Moos, R. Why Does the Electrical Conductivity in PEDOT: PSS Decrease with PSS Content? A Study Combining Thermoelectric Measurements with Impedance Spectroscopy. *Journal of polymer science part B: polymer physics* **2012**, *50* (14), 976–983.
- (144) Vossmeier, T.; Joseph, Y.; Besnard, I.; Harnack, O.; Krasteva, N.; Guse, B.; Nothofer, H.-G.; Yasuda, A. Gold-Nanoparticle/Dithiol Films as Chemical Sensors and First Steps toward Their Integration on Chip. In *Physical Chemistry of Interfaces and Nanomaterials III*; SPIE, 2004; Vol. 5513, pp 202–212.
- (145) Choi, J.; Lee, J.; Choi, J.; Jung, D.; Shim, S. E. Electrospun PEDOT: PSS/PVP Nanofibers as the Chemiresistor in Chemical Vapour Sensing. *Synthetic Metals* **2010**, *160* (13–14), 1415–1421.
- (146) Gao, N.; Yu, J.; Tian, Q.; Shi, J.; Zhang, M.; Chen, S.; Zang, L. Application of PEDOT: PSS and Its Composites in Electrochemical and Electronic Chemosensors. *Chemosensors* **2021**, *9* (4), 79.
- (147) Freddi, S.; Drera, G.; Pagliara, S.; Goldoni, A.; Sangaletti, L. Enhanced Selectivity of Target Gas Molecules through a Minimal Array of Gas Sensors Based on Nanoparticle-Decorated SWCNTs. *Analyst* **2019**, *144* (13), 4100–4110.
- (148) Bachar, N.; Mintz, L.; Zilberman, Y.; Ionescu, R.; Feng, X.; Müllen, K.; Haick, H. Polycyclic Aromatic Hydrocarbon for the Detection of Nonpolar Analytes under Counteracting Humidity Conditions. *ACS Applied Materials & Interfaces* **2012**, *4* (9), 4960–4965.

(149) Bayn, A.; Feng, X.; Mullen, K.; Haick, H. Field Effect Transistors Based on Polycyclic Aromatic Hydrocarbons for the Detection and Classification of Volatile Organic Compounds. *ACS applied materials & interfaces* **2013**, 5 (8), 3431–3440.

VITA

EDUCATION

2023, Ph.D. in Photonics Science and Engineering, Graduate School of Engineering and Sciences, İzmir Institute of Technology, İzmir / Turkey

Thesis Title: Two Dimensional (2D) Material Based Field Effect Transistor for Biosensor Applications

Supervisor: Assoc. Prof. Dr. Ümit Hakan YILDIZ

2017, M.Sc. in Materials Science and Engineering, Graduate School of Engineering and Sciences, İzmir Institute of Technology, İzmir / Turkey

Thesis Title: Self-organized Network of Silicon Oxide on Epitaxial Graphene

Supervisor: Prof. Dr. Cem Çelebi

2014, B.Sc. in Physics, İzmir Institute of Technology, İzmir / Turkey

PUBLICATIONS

D.O. Inanc, Z.K Ng, M. Baskurt, B.Keles, G. Vardar, H. Sahin, S.H. Tsang, A. Palaniappan, U.H. Yıldız, E. Teo

A multi-layered Graphene Based Gas Sensor Platform for Discrimination of Volatile Organic Compounds via Differential Intercalation

Journal of Material Chemistry C 11 (14) 4703-4710 (2023)

D.O. İnanc, M.U. Mutlu, S. Karabacak, U.H. Yıldız

Advances and Future Perspective of Graphene Field Effect Transistors (GFETs) for Medical Diagnostics and Point-of-Care Tools

Emerging Technologies in Biophysical Sciences: A World Scientific Reference: Volume 3: Emerging Technologies for Diagnostics (2023)

M. Guzelgulgen, D.O. Inanc, U.H. Yıldız, A.Arslan-Yıldız

Glucuronoxylan-based Quince Seed Hydrogel: A promising scaffold for tissue engineering applications

International Journal of Biological Macromolecules 180, 729-738 (2021)

R. Bilginer, D-Ozkendir Inanc, U.H. Yıldız, A.Arslan-Yıldız
Biocomposite Scaffolds for 3D Cell Culture: Propolis Enriched Polyvinyl Alcohol
Nanofibers Favoring Cell Adhesion
Journal of Applied Polymer Science 138 (17), 50287, (2021)

D.O. Inanc, C. Celebi, U.H. Yıldız
Lipid bilayer on Wrinkled-interfaced Graphene Field Effect Transistor
Materials Letters 284, 128998, (2021)

H.E. Oguzturk, Y. Sozen, C. Akyol, D.O. Inanc, U.H. Yıldız, H.Sahin
Toward Single-Layer Janus Crystals: Off-balance Materials from Synthesis to
Nanotechnology Applications
Journal of Applied Physics 129 (160902) (2021)

S.B. Kalkan, H.Aydın, D. Ozkendir, C. Celebi
The Effect of Adsorbates on the Electrical Stability of Graphene Studied by
Transient Photocurrent Spectroscopy
Applied Physics Letters 112 (1) (2018)

E. Kus, D.Ozkendir, V. Fırat, C.Celebi
Epitaxial Graphene Contact Electrode for Silicon Carbide based Ultraviolet
Photodetector
Journal of Physics D: Applied Physics 48 (9), 095104 (2015)